

Laser manipulation of metastable neon atoms

Citation for published version (APA):

Hoogerland, M. D. (1993). *Laser manipulation of metastable neon atoms*. [Phd Thesis 1 (Research TU/e / Graduation TU/e), Applied Physics and Science Education]. Technische Universiteit Eindhoven.
<https://doi.org/10.6100/IR399838>

DOI:

[10.6100/IR399838](https://doi.org/10.6100/IR399838)

Document status and date:

Published: 01/01/1993

Document Version:

Publisher's PDF, also known as Version of Record (includes final page, issue and volume numbers)

Please check the document version of this publication:

- A submitted manuscript is the version of the article upon submission and before peer-review. There can be important differences between the submitted version and the official published version of record. People interested in the research are advised to contact the author for the final version of the publication, or visit the DOI to the publisher's website.
- The final author version and the galley proof are versions of the publication after peer review.
- The final published version features the final layout of the paper including the volume, issue and page numbers.

[Link to publication](#)

General rights

Copyright and moral rights for the publications made accessible in the public portal are retained by the authors and/or other copyright owners and it is a condition of accessing publications that users recognise and abide by the legal requirements associated with these rights.

- Users may download and print one copy of any publication from the public portal for the purpose of private study or research.
- You may not further distribute the material or use it for any profit-making activity or commercial gain
- You may freely distribute the URL identifying the publication in the public portal.

If the publication is distributed under the terms of Article 25fa of the Dutch Copyright Act, indicated by the "Taverne" license above, please follow below link for the End User Agreement:

www.tue.nl/taverne

Take down policy

If you believe that this document breaches copyright please contact us at:

openaccess@tue.nl

providing details and we will investigate your claim.

LASER MANIPULATION OF METASTABLE NEON ATOMS

PROEFSCHRIFT

TER VERKRIJGING VAN DE GRAAD VAN DOCTOR AAN
DE TECHNISCHE UNIVERSITEIT EINDHOVEN, OP GEZAG
VAN DE RECTOR MAGNIFICUS, PROF. DR. J.H. VAN LINT,
VOOR EEN COMMISSIE AANGEWEEZEN DOOR HET COLLEGE
VAN DEKANEN IN HET OPENBAAR TE VERDEDIGEN OP
DINSDAG 29 JUNI 1993 OM 16.00 UUR

DOOR

MAARTEN DIRK HOOGERLAND

GEBOREN TE BUSSUM



DIT PROEFSCHRIFT IS GOEDGEKEURD
DOOR DE PROMOTOREN
PROF.DR. H.C.W. BEIJERINCK
EN
PROF.DR. B.J. VERHAAR

COPROMOTOR:
DR. K.A.H. VAN LEEUWEN

The work described in this thesis was carried out at the Physics Department of the Eindhoven University of Technology and has been supported by the Foundation for Fundamental Research on Matter (FOM)

*Tau, dat gezegd kan worden,
is niet het eeuwig Tau.*

Contents

1	Introduction	3
1.1	Introduction to light forces	4
1.2	This thesis	7
	References	8
2	Photon statistics of resonance fluorescence: Ne* deflection experiments and Monte-Carlo simulations	9
2.1	Introduction	10
2.2	Experiment	12
2.2.1	Atomic beam apparatus	12
2.2.2	Laser equipment	14
2.2.3	Magnetic degeneracy	16
2.3	Monte-Carlo simulation	17
2.3.1	Theory	17
2.3.2	Numerical implementation	20
2.4	Data analysis and results	22
2.5	Conclusions	25
	References	25
3	Force, diffusion and channeling in sub-Doppler laser cooling	27
3.1	Introduction	28
3.2	Classical and semiclassical theory	29
3.2.1	Classical picture	30
3.2.2	Semiclassical treatment	31
3.3	Quantum Monte-Carlo treatment	33
3.3.1	Basic theory	33
3.3.2	Numerical implementation	35
3.4	Experiment	37
3.4.1	Atomic beam setup	37
3.4.2	Laser equipment	39
3.4.3	Data analysis	41
3.5	Results and discussion	43
3.5.1	The $\sigma^+\sigma^-$ polarization configuration	43
3.5.2	Channeling in a standing wave	47

3.5.3	The $\pi^x\pi^y$ polarization configuration	53
3.6	Conclusions	57
	References	57
4	A 1600-fold increase in beam intensity for neutral atoms using laser cooling forces	59
4.1	Introduction	60
4.2	Theory of operation	63
4.2.1	Collimating sections	63
4.2.2	Magneto-optical lens	68
4.2.3	Bright beam	71
4.3	Experimental design	73
4.3.1	Metastable atom source	73
4.3.2	Collimating stages	74
4.3.3	Magneto-optical lens	75
4.3.4	Laser equipment	77
4.3.5	Beam diagnostics	78
4.3.6	Beam setup	79
4.4	Results	80
4.4.1	First collimating stage	80
4.4.2	Magneto-optical lens	82
4.4.3	Bright beam characteristics	84
4.4.4	'Brightness' vs. signal gain	84
4.5	Final remarks and future prospects	85
	References	86
	Summary	89
	Samenvatting	91
	Dankwoord/Curriculum Vitae	93

Chapter 1

Introduction

1.1 Introduction to light forces

Resonant laser light can exert a large force on neutral atoms. This is illustrated in figure 1.1. When an initially not moving atom absorbs a laser photon (part (a) of the figure), it also absorbs the photon momentum $\hbar k$. Here, k is the wavevector of the photon with an absolute value $k = 2\pi/\lambda$. The excited atom now has a velocity $\hbar k/M$ in the direction of the laser (part (b) of the figure). After some time, the atom can spontaneously emit a photon in a random direction (part (c) of the figure), again getting a momentum recoil of the spontaneously emitted photon. The atom thus returns to

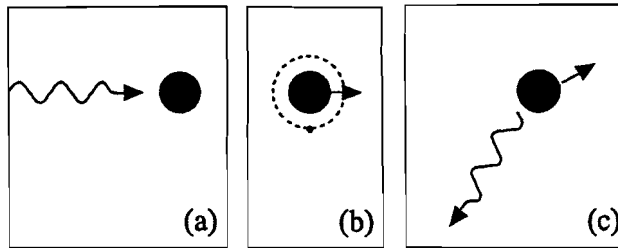


Figure 1.1: *When an atom absorbs a laser photon, as indicated in (a), it is excited and absorbs the photon momentum, as indicated in (b). When the photon is spontaneously emitted in a random direction, the atom returns to the ground state and gets another recoil. After many of these events the atom is on average accelerated in the direction of the laser.*

the ground state, from which it can be excited again. After many of these cycles, the recoils due to the spontaneous emissions will average to zero. Due to the recoils from the laser photons however, it will gain a momentum in the direction of the laser. If the laser light is resonant with a strong (electronic) transition in the atom, the atom can absorb many photons per unit of time. The maximum force exerted on the atoms is $F = \hbar k \Gamma/2$, with $\Gamma = 1/\tau$ the reciprocal of the natural radiative lifetime of an atom in the excited state. For neon, with a mass $M = 20$ a.m.u., the wavelength of the laser light resonant with a strong two-level transition is 640 nm, and the lifetime of the upper state is 20 ns. This results in a maximum acceleration of $F/M = 10^6$ ms⁻².

When an atom moves, it sees a laser beam Doppler shifted with an amount $\Delta_{\text{Doppler}} = -k \cdot v$ with v the velocity of the atom. As the natural linewidth of an optical transition is in the order of $\Gamma/2\pi = 8$ MHz, a velocity of 5 ms⁻¹ will shift the laser out of resonance. This is used to exert a velocity-dependent force on the atoms. Wineland and Dehmelt [1] as well as Hänsch and Schawlow [2] proposed a method to use this principle to cool neutral atoms. An atom is placed in a standing wave of slightly red-detuned ($\Delta_{\text{laser}} = -\Gamma/2$) laser light. It sees the counterpropagating laser beam blue-shifted by the Doppler effect and thus closer to resonance. This yields a dispersion-shaped acceleration vs. velocity profile as shown in figure 1.2. Near zero velocity, the atom

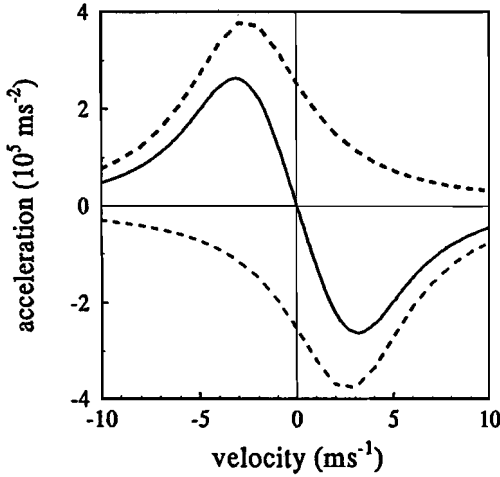


Figure 1.2: The acceleration of neon atoms due to the radiation pressure force in a standing laser wave as a function of the atomic velocity for optimal conditions $\Delta = -\Gamma/2$. The contributions to the total force of the two laser beams are represented by the dashed lines respectively. The total force is represented by the full line, showing a linear increase with the velocity for small velocity. The saturation parameter $s = I/I_0 = 1$ for both laser beams.

experiences a slowing force proportional to its velocity, as if it were moving in molasses. Thus the motion of the atoms is strongly damped with a friction coefficient α that is linear in the laser intensity. The width of the velocity distribution is strongly narrowed. If the velocity distribution is Gaussian, an equivalent temperature $\frac{1}{2}T = \frac{1}{2}m\langle v^2 \rangle / k_B$ can be assigned to the atomic ensemble. As the velocity distribution is narrowed, this temperature decreases. This is called laser cooling. The limit to this cooling process is imposed by the random recoils from the spontaneous emission photons, which heat the atomic ensemble. This can be described with a diffusion coefficient in velocity space D . By integrating the Fokker-Planck equation for this ensemble, an equilibrium Gaussian velocity distribution is obtained, and thus an ensemble with a ‘temperature’. For optimal conditions, the temperature is $k_B T_{\text{Doppler}} = D/\alpha = \hbar\Gamma/4$, independent of the laser intensity. For neon, this temperature $T_{\text{Doppler}} = 200\mu\text{K}$.

Although the first measurements confirmed this limit [3], in many experiments much lower temperatures were observed [4]. These lower temperatures were explained by the subsequent theoretical developments [5]. For an overview of the present work on laser cooling we refer to the special issue of JOSA B on laser cooling of atoms [6].

The electronic levels of an atom in a strong (resonant) light field are shifted by the AC Stark shift equal to $\hbar\Omega_s = \sqrt{\Omega^2 + \Delta^2}$, with Ω the Rabi frequency, proportional to the square root of the laser intensity, and Δ the laser detuning. Hence, a gradient in laser intensity and thus in AC Stark shift will exert a force on the atoms. Large gradients in laser intensity occur for instance between the nodes and the antinodes in a standing wave and in evanescent waves of total internal reflection of a laser beam in a prism. In a standing wave, there are large gradients in the light shift, and thus the atoms will, apart from the Doppler force, experience a force. If the atom has more than two levels, e.g., in case of magnetic degeneracy of the excited and ground states, these forces can be used to cool the atoms. The coupling of the magnetic sublevels to the

excited state by polarized laser light is determined by the Clebsch-Gordan coefficients. Hence a spatial gradient of the polarization of the light can also give rise to gradient forces. One example is the $\pi^x\pi^y$ polarization configuration, which is formed by two counterrunning laser waves with the same frequency and intensity, but with orthogonal linear polarizations. In this case, the polarization of the effective light field changes from σ^+ to π to σ^- in one half of a wavelength, as shown in the upper part of figure 1.3. In σ^+ polarized laser light, that induces $\Delta m = 1$ transitions the $m = +\frac{1}{2}$ magnetic

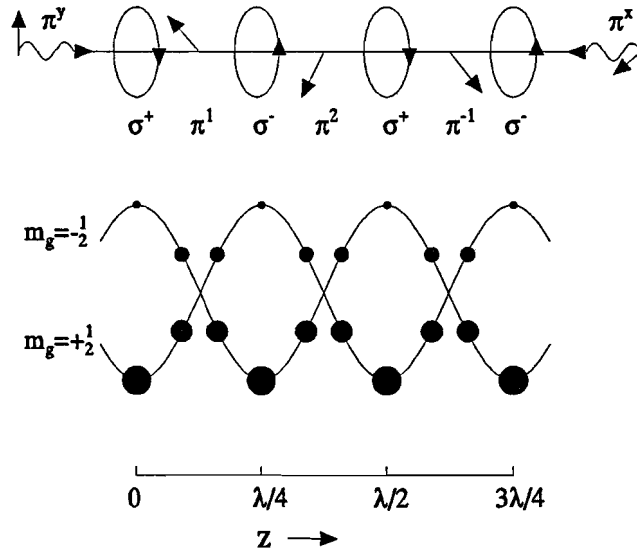


Figure 1.3: In a standing wave of orthogonal linear polarizations the local polarization of the resulting light field strongly depends on the position in the standing wave as shown in the upper part of the figure. The resulting light shift of the two ground levels for a $J = \frac{1}{2} \rightarrow J = \frac{3}{2}$ is shown in the lower part. The steady-state populations of these levels is indicated by the filled circles. The lowest sublevel is also the most populated one.

substate is the most light shifted: its coupling with the excited state is the largest. When the laser detuning is negative, this means that this substate is the lowest in energy. By absorption-spontaneous emission cycles, the atoms are optically pumped to this state. We will now consider an atom that is in this particular ground state. As the atom moves, it gets to a region with a different laser polarization, and the light shift decreases. The internal energy thus increases, which goes at the expense of kinetic energy. Thus the atom is decelerated. Now, there is a probability for the atom to be optically pumped to another magnetic substate, that is now lowest in energy. Hereby, the internal energy of the atom is decreased again, and the excess energy is carried away

by the spontaneous emission photon. This process can be repeated many times, causing the atom to decelerate. Although the absolute magnitude of the force induced by this cooling process is linear in the laser intensity, the friction coefficient is independent of the laser intensity. As the heating by spontaneous emission is linear with the laser intensity, the temperature can infinitely be decreased. The only limit to this cooling process shows up when the width of the velocity distribution is comparable to the recoil of one single photon [7]. This limit is called the recoil limit. This ‘Sisyphus’ effect is also present in the case of counterrunning σ^+ polarized laser beams in the presence of a magnetic field perpendicular to the laser beams [7, 8]. Another mechanism for cooling to the recoil limit is the case of counterrunning orthogonal circularly polarized laser beams [5]. All of these mechanisms yield temperatures close to the recoil limit, which is $T_r = 1.2\mu\text{K}$ for neon.

1.2 This thesis

This thesis is based on three papers, each addressing a different aspect of light forces on atoms.

In chapter 4, the design, tests and operation of an atomic beam brightener are discussed. We use Doppler cooling to intensify a beam of metastable ($\{3s\}^3P_2$) neon atoms by applying it in two dimensions. In order to increase the capture range of the cooling process, we use effectively curved wavefronts, keeping the angle between the laser beam and the atom trajectory at a fixed value. We increase the capture range to $\pm 60\text{ms}^{-1}$ for an atomic beam with an average axial velocity of 600ms^{-1} , achieving a rather large cross-section, parallel atomic beam. Then, the atomic beam is focussed to a small spot using a two-dimensional Magneto-Optical trap, which acts as a lens for neutral atoms. We recollimate the atomic beam using the Doppler cooling technique near the focus of this lens. This way we obtain a highly collimated intense atomic beam with a small cross-section. This apparatus has recently been tested and taken into operation. It unfolds a large range of scientific applications of intensified atomic beams, e.g., ultra high resolution atomic spectroscopy, detailed studies of atomic collision processes and improved atomic frequency standards.

We also investigate in detail the effects of running and standing laser fields on an ensemble of atoms with a well-defined initial velocity by atomic beam deflection. In chapter 2, we study the deflection of a well-collimated atomic beam of metastable neon atoms by a running laser wave. The velocity change of an atom in the direction of the laser beam is a measure for the number of scattered photons by the atom. An atomic beam, interacting with the laser for a finite amount of time, will thus undergo an average deflection. However, due to the random nature of spontaneous emission, the number of scattered photons fluctuates, and thus gives rise to a spread in deflection. By analyzing this spread in deflection, we observe that the fluorescence light has sub-Poissonian photon statistics. This can be interpreted as evidence for the explicit quantum nature

of light. Extensive results are presented, giving the deviation of photon statistics of the resonance fluorescence from Poissonian statistics as a function of laser detuning and laser intensity. The results are compared to the results of a numerical simulation, showing excellent agreement.

In chapter 3, the first force and diffusion measurements are presented on sub-Doppler cooling processes. We use the deflection of a well-collimated atomic beam of metastable neon atoms by a short interaction with a (quasi-) standing wave. The average deflection of the atomic beam now gives an average force on the atoms, while the spread in deflection is a measure for the diffusion. In some polarization configurations, we observe effects of channeling of the atoms in the spatially modulated potential induced by the difference in AC Stark shift in the nodes and the antinodes of the standing laser wave. These measurements form a much more stringent test for the existing theories on laser cooling to very low temperatures than the traditional measurements of the final temperature. They are compared to both semi-classical and fully quantum-mechanical calculations, finding excellent agreement.

References

- [1] D.J. Wineland and H. Dehmelt. *Bull. Am. Phys. Soc.* **20**, 637(1975).
- [2] T.W. Hänsch and A.L. Schawlow. *Opt. Comm.* **13**, 68(1975).
- [3] S. Chu, L. Hollberg, J. E. Bjorkholm, A. Cable, and A. Ashkin. *Phys. Rev. Lett.* **55**, 48(1985).
- [4] P. Lett, R. Watts, C. Westbrook, W. D. Phillips, P. Gould, and H. Metcalf. *Phys. Rev. Lett.* **61**, 169(1988).
- [5] J. Dalibard and C. Cohen-Tannoudji. *J. Opt. Soc. Am.* **B6**, 2023(1989).
- [6] See: special issue on Laser Cooling and Trapping of atoms in *J. Opt Soc.* **B6**, (1989).
- [7] M.D. Hoogerland, H.C.W. Beijerinck, K.A.H. van Leeuwen, P. van der Straten, and H.J. Metcalf. *Europhys. Lett.* **19**, 669(1992).
- [8] B. Sheehy, S-Q. Shang, P. van der Straten, and H.J. Metcalf. *Phys. Rev. Lett.* **64**, 858(1990).

Chapter 2

Photon statistics of resonance fluorescence: Ne* deflection experiments and Monte-Carlo simulations

M.D. Hoogerland, H.C.W. Beijerinck and K.A.H. van Leeuwen

*Eindhoven University of Technology,
P. O. Box 513 5600 MB Eindhoven, the Netherlands*

Abstract

The photon statistics of resonance fluorescence are studied by means of an atomic beam deflection experiment. The expected sub-Poissonian statistics are a manifestation of the quantummechanical nature of light. We present extensive results giving the deviation from Poissonian photon statistics as a function of the intensity and the detuning of the exciting laser field. We compare the data with results from a numerical simulation and give an explicitly real-valued expression for the integrated photon waiting time distribution. Due to a transient effect a large difference between the two level theory and our experimental data in case of σ excitation is observed. However, excellent agreement between the experimental data and the numerical simulation is demonstrated.

2.1 Introduction

The interaction of a two-level atom with an almost resonant running laser wave, and especially the characteristics of the spontaneously reemitted light (resonance fluorescence), has been thoroughly studied in the past years. The statistical properties of resonance fluorescence differ markedly from those of other light sources.

For instance, a monochromatic laser beam can generally be associated with a single mode coherent state. When such laser light is investigated with a photomultiplier, theory predicts a Poissonian distribution of photons detected in a given time interval (given some minimal assumptions as to the detector operation). This Poissonian distribution results from the lack of time correlation between the detected photons. Any loss of coherence will lead to a larger spread in the photon number distribution. In the limit of thermal light, the photons tend to appear in bunches, and the spread in the number of detected photons is large.

In the semiclassical treatment of the interaction between light and matter, the above results are reproduced if the 'coherent state' of the laser wave is replaced by a classical monochromatic light wave. The term 'detected photons' should then be replaced by, e.g., photoelectric counts.

In contrast to such 'classical' light, the resonance fluorescence from one atom will, as shown by Kimble *et al.* [1], tend to appear as photons which are rather equally spaced in time: an atom that has just emitted a photon will have to get re-excited first by the driving field. This phenomenon is called anti-bunching. This anti-bunching is obvious in the spontaneous photon waiting time distribution for resonant excitation, as shown by, e.g., Carmichael [2]. Associated is a spread in the number of detected photons in a given time interval that is smaller than the Poissonian value.

These statistical properties will be reflected in photoelectric count distributions. Mandel [3] has demonstrated that the semiclassical treatment cannot reproduce anti-bunching and sub-Poissonian photon number statistics of the photo-electric counts. These therefore represent true 'quantum features' of the radiation field.

In order to quantify the deviation from a Poissonian photon number distribution, characterized by a variance $\langle(\Delta N)^2\rangle$ equal to the average number of photons $\langle N\rangle$, Mandel introduced the normalized second factorial moment

$$Q = \frac{\langle(\Delta N)^2\rangle - \langle N\rangle}{\langle N\rangle}. \quad (2.1)$$

The parameter Q is negative for a sub-Poissonian and positive for a super-Poissonian distribution. Mandel derived a formula giving Q for resonant monochromatic incident radiation as a function of interaction time T and driving field intensity. In the limit of a long interaction time ($T \ll \tau$, with τ the natural lifetime of the upper level) a simple relation,

$$Q = \frac{-3s}{(1+s)^2} \quad (2.2)$$

is obtained, with the on-resonance saturation parameter $s = 2\Omega^2/\Gamma^2$ proportional to the driving field intensity (here Ω is the Rabi frequency and $\Gamma \equiv 1/\tau$ the linewidth of the excited state). The minimum value, $Q = -\frac{3}{4}$, is obtained at $s = 1$. This corresponds to a width of the photon number distribution equal to half the width of a

Poissonian distribution. At low intensities of the exciting field, the excitation rate of the atom is much lower than the spontaneous decay rate. Every absorption is almost immediately followed by a spontaneous emission, and the number distribution of the detected photons is determined by the statistics of the exciting laser field, and thus Q approaches zero. For the high intensity limit, re-excitation occurs very quickly, and the re-excitation delay that causes anti-bunching can be neglected.

Since then, the theory has been extended to include detuning of the driving field [4] and finite bandwidth effects [5, 6]. Analytical expressions for the complete photon number distribution $p(N, t)$ have been derived by Cook [7], Lenstra [8] and Kaminishi [9].

An explicit expression for Q as a function of detuning is given by Arnoldus[6], Singh[5] and Blatt [10]:

$$Q = \frac{\beta s(4\Delta^2/\Gamma^2 - 3)}{(1 + s + 4\Delta^2/\Gamma^2)^2} \quad (2.3)$$

with Δ the detuning and β the photon detection efficiency. For $\Delta = 0$ and $\beta = 1$ this leads to the simple expression (2.2). Equation 2.3 shows that for $\Delta > \sqrt{\frac{3}{4}}\Gamma$, super-Poissonian photon statistics appear, which means that anti-bunching does not necessarily lead to sub-Poissonian photon statistics. The fact that sub-Poissonian photon number statistics does not require anti-bunching was shown by Zou *et al.* [11].

Experimentally, less information is available. A major problem in the photon counting experiments is usually the low photon detection efficiency β , due to both the quantum efficiency of the photomultiplier and the limited solid angle of detection. As the photon detection efficiency however, appears directly in the expression for Q , sub-Poissonian features in such an experiment are strongly suppressed. Moreover, only one atom at a time should interact with the laser field, thus leading to extremely low count rates. Because of these low count rates and low overall detection efficiency the results of these experiments tend to have a relatively large uncertainty.

The first experimental result has been reported by Short and Mandel [12, 13]. They performed a photon-counting experiment using sodium as a two-level system with a dye laser to supply the driving field. The laser was on resonance and the intensity was at about half the saturation value ($s \approx 0.5$). They experimentally observed a negative value for Q_{exp} of $(-1.48 \pm 0.25) \cdot 10^{-3}$. With the estimated detector efficiency of $3.9 \cdot 10^{-3}$, this agrees well with the theoretical value at $\beta = 1$ of $Q = -0.59$. More extensive results using a photon-counting technique have been reported for a transition between two levels in a three-level system, prior to a quantum jump to the third level, in barium [14, 15]. In these experiments a relatively large detection efficiency was combined with a low background count rate, resulting in small errors. The parameter Q was measured as a function of the laser intensity for $0.2 < s < 6$. The results confirmed Mandel's two-level formula (2.2) with a relatively small uncertainty.

Direct measurements of the time correlation of spontaneous emission light from a single ion in a trap have been performed by Diedrich *et al.* [16]. In this type of experiment anti-bunching of the spontaneous emission light is demonstrated directly. However, the detection efficiency in these experiments constitutes a problem as well.

Instead of using a photomultiplier, Cook [17] suggested studying photon statistics using atomic motion as a detector for spontaneous emission. By analyzing the radiation-pressure induced deflection of an atomic beam, the photon number statistics

can be deduced using a simple relation between net momentum transfer and spontaneous emission. When an atom absorbs a photon it will also absorb the photon momentum $\hbar k_{\text{laser}}$. If an absorption is followed by a stimulated emission in a running light wave, there is no net effect on the final momentum. In case of a spontaneous emission, the photon will be emitted in a random direction, giving the atom a random recoil momentum $\hbar k_{\text{spont}}$. Thus, the average recoil momentum for spontaneous emission is zero and, on the average, the atom will gain a net momentum $\hbar k_{\text{laser}}$. Consequently, in such an experiment an atom ‘remembers’ each spontaneous emission, as it is ‘stored’ in its momentum. Hence the effective photon detection efficiency in such an experiment is equal to unity. In an atomic beam, the average deflection angle is a measure for the average number of spontaneous emissions and hence for the upper state population. The spread in the deflection angles is determined by the random direction of the spontaneous emissions, which contribution is easily calculated, and by the width of the photon number distribution. An extensive theoretical analysis of light induced deflection of an atomic beam, including both standing- and running light wave cases, has been performed by Tanguy *et al.* [18].

In 1989 experiments have been published by Oldaker *et al.* [19] and by Hoogerland *et al.* [20]. Oldaker used a supersonically cooled sodium beam, to obtain a narrow velocity distribution. When the atoms are prepumped to the correct hyperfine substate, sodium can be excited on a two-level transition. The position of the sodium beam was measured by a scanning hot wire detector. He used a full Gaussian laser beam, thus introducing a convolution over the laser intensity. The expected detuning dependence of Q was reproduced quite well.

We also reported such an experiment using metastable neon, which is easy to detect, has a pure two-level system with no bothersome hyperfine structure and can be easily produced in a supersonic expansion. We used an existing atomic beam apparatus, previously used for elastic scattering experiments [21], which already had the required beam collimation and detection equipment built in. We reported extensive results confirming both the detuning- and intensity dependence of Q .

In this paper we describe our experiment in detail. In section 2.3.1 we describe a Monte-Carlo simulation of our experiments, based on the pure state analysis of resonant light scattering by Mollow [22], in which all experimental details are included. The agreement with our experiments is excellent, as shown in section 2.4.

2.2 Experiment

2.2.1 Atomic beam apparatus

The atomic beam apparatus was previously used for atomic beam scattering experiments to determine differential elastic cross-sections [21]. A supersonic beam of neon atoms, partly excited in a DC-discharge to the metastable 3P_2 and 3P_0 states is created in a source described by Verheyen *et al* [23]. The discharge runs through the $\approx 100 \mu\text{m}$ radius nozzle. This type of metastable source creates a beam with an average axial velocity of $\approx 1000 \text{ ms}^{-1}$ and a velocity spread (fwhm) of $\approx 300 \text{ ms}^{-1}$. The metastable fraction of the atomic beam is $\approx 10^{-5}$, leading to a typical center-line beam intensity of

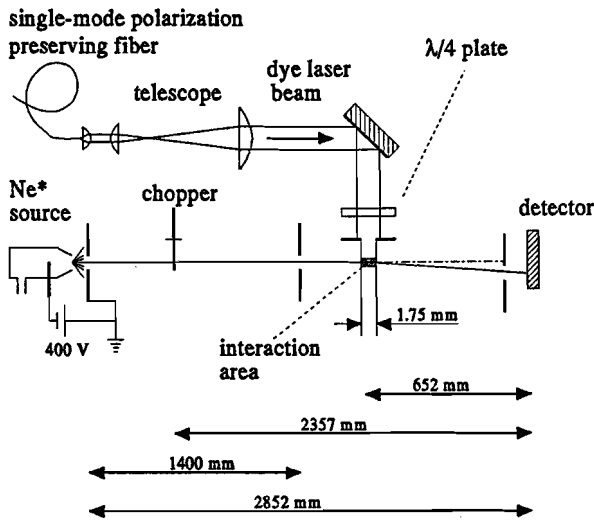


Figure 2.1: An overview of the experimental setup. The atomic beam is collimated using two slits, and intercepted by the laser beam. The resulting deflection of the atomic beam is measured using a scanning slit in front of a large-area metastable atom detector.

$\approx 1.5 \cdot 10^{13} \text{s}^{-1} \text{sr}^{-1}$. Typical operating conditions are a source inlet pressure of 30 Torr, a discharge voltage of 400 V and a discharge current of 10 mA. The flat plate anode of the discharge also acts as the first beam collimating slit.

The source vacuum chamber has a built-in differential pumping section to decrease the gas load for the rest of the setup. The second vacuum chamber also serves as a differential pumping section. This results in a very low gas load for the rest of the setup. The residual gas pressure after the second differential pumping section is $\approx 2 \cdot 10^{-8}$ Torr. This pressure is achieved by a five-stage differential pumping design using several oil diffusion pumps, a turbomolecular pump under the interaction region and a cryopump. When not in operation, the detector chamber is separated from the rest of the setup and is constantly kept at ultra-high vacuum ($< 10^{-9}$ Torr) by an ion-getter pump, resulting in a zero false-count rate in the experiments.

An overview of the experiment is shown in figure 2.1. The atomic beam is collimated to $< 10^{-4}$ rad using two slits: the first ($100 \times 500 \mu\text{m}$) located at 5 mm and the second ($50 \times 500 \mu\text{m}$) at 1.400 m downstream from the metastable source. All slits are carefully aligned to be parallel to within 5 mrad. The 1.75 mm long interaction region, defined by a collimating slit for the laser beam, is located at 2.200 m from the source. The interaction time ranges from 1.46 to 2.19 μs (corresponding to 75 and 113 lifetimes of the excited state respectively) for the 800 to 1200 ms^{-1} experimental range of velocities, so that the condition of a long interaction-time is fulfilled.

The beam profile after deflection is analyzed using a stepper-motor driven $50 \times 2000 \mu\text{m}$ movable slit in front of a large area Auger type surface ionization metastable atom detector. In such a detector, the metastable atom hits a stainless steel plate, which then emits an electron. The electron is accelerated by an electric field and de-

tected by an electron-multiplier. The total spread in delaytime of this detection system is less than 100 ns. The detection efficiency is estimated to be between 0.2 and 1 for metastable neon atoms. UV photons from the discharge, in which the metastables are formed, are detected as well. Ground state atoms and residual gas atoms are not detected.

The atomic beam is chopped to enable single burst time-of-flight velocity analysis of the axial velocity of the deflected atoms. The chopper is located at 2450 mm from the detector, giving a typical flight time from the chopper to the detector of 2.5 ms at an average beam velocity of 1000 ms^{-1} . The chopper has an open time of $\approx 130 \mu\text{s}$. The velocity distribution is analyzed using a multi-scaler, using 50 time channels of $100 \mu\text{s}$ width. This yields a velocity resolution (fwhm) of $\Delta v/v = 0.06$. The zero of the timescale is carefully calibrated by measuring the arrival time of the chopped UV-light from the discharge to the detector. The time-of-flight measurements greatly simplify the analysis of the deflected beam profiles, avoiding a convolution over both the interaction time and the longitudinal atomic momentum. The time-of-flight apparatus is described in detail in reference [24]. All measurements are fully automated using a Phydas/EPEP laboratory automation system, a local standard of the physics department. This system also continuously checks experimental parameters like laser power, laser frequency, chopper frequency and the inlet pressure of the metastable beam source. A time-of-flight measurement with these extremely well-collimated atomic beams has a typical average atom count rate of 2 kHz. In order to reduce statistical errors a total atom count of about 10^4 is required. This results in a measuring time of about 20 seconds per position of the detector slit, and thus a total measuring time of about 20 minutes per measurement of 50 positions. The detector positions are chosen equally spaced at $50 \mu\text{m}$ intervals.

2.2.2 Laser equipment

In figure 2.2 part of the level scheme of neon is displayed. Neon in the ground state has the electron configuration $\{(1s)^2(2s)^2(2p)^6\}$. When we excite one electron to a $3s$ orbital we obtain the four fine structure states of the $\{(1s)^2(2s)^2(2p)^5(3s)\}$ configuration. The states 3P_0 and 3P_2 (Russell-Saunders notation) are metastable and have a radiative lifetime of at least several seconds. The states $\{\alpha_1\}$ to $\{\alpha_{10}\}$ (Paschen numbering) form the $\{(1s)^2(2s)^2(2p)^5(3p)\}$ fine structure multiplet. All these states are short-lived, with a radiative lifetime $\tau \approx 20 \text{ ns}$. For our experiment we use the transition from the metastable 3P_2 to the $J = 3\{\alpha_9\}$ ($\tau = 19.4 \text{ ns}$) state, since this is a cycling transition and the system then constitutes a pure two-level system with only magnetic degeneracy. The natural linewidth of this transition is $1/(2\pi\tau) = 8.2 \text{ MHz}$. All other multiplet states can decay to the short-lived 3P_1 and 1P_1 states, and from there to the ground state. The wavelength of the laser light resonant with the two-level transition is easily produced by commercial dye lasers, operating on DCM dye [25].

In our experiment we use a small frame Coherent Innova 70 Argon Ion pump laser and a Spectra-Physics 380D ring dye laser. The laser is frequency stabilized by the Spectra-Physics locking electronics. The linewidth of the laser light is $\approx 250 \text{ kHz}$, which is negligible compared to the natural linewidth of the excited state of the atom. Long-

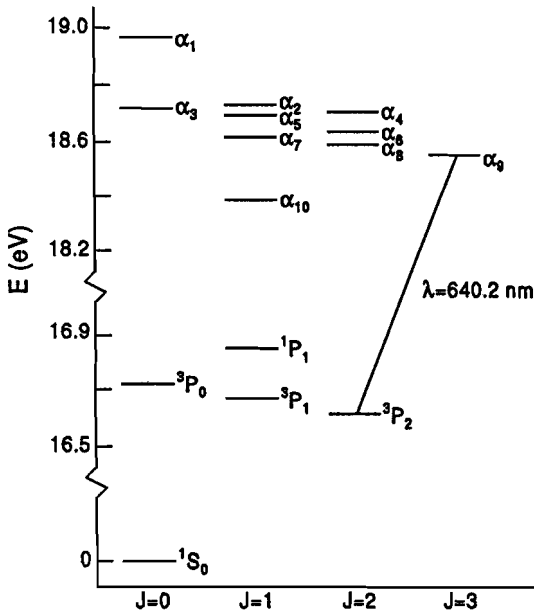


Figure 2.2: Partial level scheme of neon. The lifetime of the metastable 3P_0 and 3P_2 states is at least several seconds. We use the two-level transition from the 3P_2 state to the $\{\alpha_0\}$ state at 640.225 nm.

term drift is prevented by referring every five seconds to a small auxiliary beam machine. Here, part of the laser beam is crossed at right angles with a well-collimated atomic beam, and the laser frequency is adjusted to maximize the fluorescence light. During this short procedure the experiment is interrupted. The procedure is described in detail by Verheyen *et al.* [26].

The laser beam is transported to both the auxiliary beam machine and to the actual experiment via a single mode, polarization preserving fiber (York HB600). The polarization can be preserved to better than 1 : 100 over 30 meters of fiber when the optical axis of the fiber is properly aligned to the laser polarization, while the throughput can be as high as 70%. Using fibers has several advantages. One is that building vibrations do not disturb the position and direction of the laser beam in the experiment, as is the case when using mirrors to transport the laser beam. Another is that the alignment of the laser is decoupled from the alignment in the experiment. Coupling the laser beam into and out of these fibers is done with home-built fibercouplers using standard ($25\times$) microscope objectives.

After the fiber, the laser beam is expanded in a telescope using large-aperture lenses, avoiding aberrations and edge diffraction caused by these lenses. Before the experiment, the laser beam is carefully aligned and the waist length of the Gaussian laser beam is maximized. The Gaussian waist radius (at $1/e^2$ intensity) at the interaction center is measured by a movable slit and a photodiode, and is found to be 2.36 mm in the horizontal direction and 2.01 mm in the vertical direction. The slight ellipticity of the laser beam is caused by the polarization preserving fiber. The 1.75 mm slit defining the interaction center is placed close ($\approx 100 \mu\text{m}$) to the atomic beam, to limit diffraction effects. This way, a nearly flat top intensity profile with less than 8% rms intensity variation over the interaction region is ensured. The laser beam is aligned perpendicular

to the collimated atomic beam by tuning the laser to the ${}^3P_2 \rightarrow \{\alpha_8\}$ transition, where the upper state can decay to the ground state. In the case of non-perfect alignment, the Doppler effect will decrease the interaction strength and thus the pumping efficiency. If the angle is scanned using a stepper-motor driven and computer controlled procedure a clear minimum in atomic beam flux for perpendicular alignment is observed. The angle between laser and atomic beam is adjusted to the angle of maximum beam attenuation. This procedure ensures that the laser beam is perpendicular to the atomic beam to within 0.5 mrad. The optional quarter wave plate is placed directly before the interaction center to avoid perturbation of the circular polarization of the light by other optical components.

2.2.3 Magnetic degeneracy

Since the lower state used for the experiment is a $J = 2$ state, magnetic degeneracy has to be taken into account. We chose the experimental conditions such that the magnetic field is zero in the interaction region, so the magnetic sublevels are indeed degenerate. To achieve this, we placed the interaction region in a full set of circular Helmholtz coils with diameters of 680 mm, 780 mm and 890 mm for the lateral, vertical and axial coils respectively.

The earth magnetic field is zeroed by using the Hanle effect on the ‘pumping’ transition to the $\{\alpha_8\}$ state, which decays primarily by cascading to the ground state. Since this is a $J_e = J_g$ transition, the transition from $m_g = 0$ to $m_e = 0$ is forbidden. Consequently, when the laser is linearly polarized, inducing $\Delta m = 0$ transitions, the atoms in the $m_g = 0$ ground state will not be pumped. This can be measured as a decrease in the pumping efficiency. However, if there is a small magnetic field, the magnetic sublevels will be mixed by the Larmor precession, and all atoms will be pumped to the ground state. This means that the pumping efficiency will have a minimum at zero magnetic field orthogonal to the laser polarization. This proved to be a very sensitive test on the magnetic field. We obtain a clear maximum in the metastable atomic beam flux if both components of the magnetic field perpendicular to the laser polarization are small, such that the Larmor frequency ω_L induced by the residual magnetic field is much smaller than the reciprocal of the interaction time. The residual magnetic field is $B < 5$ mGauss.

Because of the strongly differing Clebsch-Gordan coefficients for σ excitation from the various magnetical substates, the deflection of an atom depends very strongly on the initial magnetic substate, as shown in table 2.1. That is, under σ^+ excitation, an atom in the $m_g = -2$ substate will undergo an excitation rate that is 15 times smaller than one in the $m_g = +2$ substate. Once excited and optically pumped to another substate, its excitation rate will increase during the interaction time. Finally, the atom will end up in the pure two-level system $m_g = 2 \rightarrow m_e = 3$. Using polarized atoms, optically pre-pumped to the $m_g = 2$ state, would yield the cleanest test for the photon statistics of a two-level atom. However, optical pumping would have to be done before the sub-recoil collimation of the atoms. In our setup, this is not feasible since stray magnetic fields would destroy the polarization before the atoms reach the interaction center.

Hence, the atoms are in a statistical mixture over the magnetic substates. This

		m_g				
		-2	-1	0	1	2
Δm	-1	1	$\frac{2}{3}$	$\frac{2}{5}$	$\frac{1}{5}$	$\frac{1}{15}$
	0	$\frac{1}{3}$	$\frac{8}{15}$	$\frac{9}{15}$	$\frac{8}{15}$	$\frac{1}{3}$
	1	$\frac{1}{15}$	$\frac{1}{5}$	$\frac{2}{5}$	$\frac{2}{3}$	1

Table 2.1: The squared Clebsch-Gordan coefficients for a $J = 2 \rightarrow J = 3$ transition.

causes a larger and more asymmetric spread in the number of scattered photons than given by the two-level theory. To incorporate these effects in the comparison of the experiments with theory, we performed a Monte-Carlo simulation of the experiment, as described in section 2.3.1.

2.3 Monte-Carlo simulation

2.3.1 Theory

The semiclassical Monte-Carlo simulation used to model our experiment is based on the pure-state analysis of resonant radiation scattering by Mollow [22]. Blatt *et al* [10] extended this treatment to include atomic motion, and made the connection to the Monte-Carlo treatment of light pressure. Recently, this treatment was extended to include more than one laser beam, including all laser-cooling effects [27, 28]. We briefly summarize Mollow's treatment and present an explicitly real-valued expression for the waiting time distribution for the next spontaneously emitted photon.

We consider an atom in a running plane laser wave. The Hamiltonian has the form:

$$\hat{H} = \frac{\hat{p}^2}{2M} + \hat{H}_{0A} + \hat{H}_{0F} + \hat{H}_1(t) \quad (2.4)$$

with \hat{p} the momentum operator and M the mass of the atom, $\hat{H}_{0A} = \omega_{eg}\hat{a}^\dagger\hat{a}$ the free Hamiltonian of the atom and $\hat{H}_{0F} = \sum_k \hat{b}_k^\dagger\hat{b}_k$ the radiation field Hamiltonian. The atomic creation operator is defined by $\hat{a}^\dagger = |e\rangle\langle g|$ with $|g\rangle$ and $|e\rangle$ the time-independent ground- and excited state wavefunctions. The field creation operator \hat{b}_k^\dagger is defined to create a photon in mode k of the radiation field. The interaction Hamiltonian in the rotating wave approximation is given by

$$\hat{H}_1(t) = -\mu_{eg}^* \cdot \hat{\mathbf{E}}^\dagger\hat{a} + \text{H.C.} \quad (2.5)$$

with μ_{eg} the atomic dipole matrix element. We split the radiation field $\hat{\mathbf{E}}$ into a laser field part $\hat{\mathbf{E}}_L$ and a spontaneous emission radiation field $\hat{\mathbf{E}}_R$. Mollow used a canonical transformation to show that a single mode coherent laser field can be treated classically, when the number of photons in all other modes of the field is zero for

$t \rightarrow -\infty$. Therefore, the laser field can be represented by a complex number $\mathcal{E}_c(\mathbf{r}, t)$. For a plane laser wave, we have $\mathcal{E}_c(x, t) = \mathcal{E}_0 e^{i(kx - \omega t)}$.

We assume that at time $t = 0$ all radiation modes, except the laser mode, are empty. We expand the combined wavefunction Ψ of the atom and the radiation field in the partial wavefunctions with n spontaneously emitted photons in mode k_1 through k_n , as given by:

$$\begin{aligned} \Psi(t) &= C_g^0(t)|g, \{0\}\rangle + C_e^0(t)|e, \{0\}\rangle \\ &+ \sum_k (C_g^{1k}(t)|g, b_k^\dagger\{0\}\rangle + C_e^{1k}(t)|e, \hat{b}_k^\dagger\{0\}\rangle) \\ &+ \dots \\ &+ \sum_{k_1 \dots k_n} [C_g^{n k_1 \dots k_n}(t)|g, \hat{b}_{k_1}^\dagger \dots \hat{b}_{k_n}^\dagger\{0\}\rangle + C_e^{n k_1 \dots k_n}(t)|e, \hat{b}_{k_1}^\dagger \dots \hat{b}_{k_n}^\dagger\{0\}\rangle] \end{aligned} \quad (2.6)$$

with $\{0\}$ the vacuum radiation field state. Mollow has shown that for the partial wavefunction $\Psi^0(t) = C_g^0(t)|g, \{0\}\rangle + C_e^0(t)|e, \{0\}\rangle$ the following (Schrödinger-like) equations for C_g^0 and C_e^0 hold:

$$\begin{aligned} \hbar \left[i \frac{d}{dt} - \omega_{eg} + i \frac{\Gamma}{2} \right] C_g^0(t) &= i(\boldsymbol{\mu} \cdot \boldsymbol{\mathcal{E}}_0) e^{-i\omega t} C_g^0(t) \\ i\hbar \frac{d}{dt} C_e^0(t) &= i(\boldsymbol{\mu} \cdot \boldsymbol{\mathcal{E}}_0) e^{i\omega t} C_e^0(t) \end{aligned} \quad (2.7)$$

with Γ the spontaneous decay rate, ω_{eg} the atomic transition frequency and ω the laser frequency. This system can be solved with the boundary conditions: $C_e^0(0) = 0$ and $C_g^0(0) = 1$. The exact solution given by Mollow is:

$$C_g^0(t) = \xi_+^2 e^{i(\delta - \bar{\Omega})t/2} + \xi_-^2 e^{i(\delta + \bar{\Omega})t/2} \quad (2.8)$$

$$C_e^0(t) = - \left[\frac{\Omega}{2\bar{\Omega}} e^{-i\omega t - i\theta} [e^{i(\delta - \bar{\Omega})t/2} - e^{i(\delta + \bar{\Omega})t/2}] \right] \quad (2.9)$$

with

$$\begin{aligned} \Omega e^{-i\theta} &= 2\boldsymbol{\mu} \cdot \boldsymbol{\mathcal{E}}_0 \\ \delta &= \Delta + \frac{i}{2}\Gamma \\ \bar{\Omega} &= \sqrt{\Omega^2 + \delta^2} \\ \xi_{\pm} &= \sqrt{\frac{1}{2}(1 \pm \delta/\bar{\Omega})} \end{aligned}$$

The phase θ of the Rabi frequency Ω is of no importance for the results of the calculation, as could be expected.

The decay of the total probability $|\Psi^0(t)|^2$ in the partial wavefunction $\Psi^0(t)$ can be equated the loss of probability that no photon has been spontaneously emitted yet. In a Monte-Carlo implementation we use the function $|\Psi^0(t)|^2 = |C_g^0(t)|^2 + |C_e^0(t)|^2$ to randomly determine the photon waiting time τ_{MC} by taking a random number $\Upsilon \in [0, 1)$ and solving the equation

$$1 - |\Psi^0(\tau_{MC})|^2 = \Upsilon \quad (2.10)$$

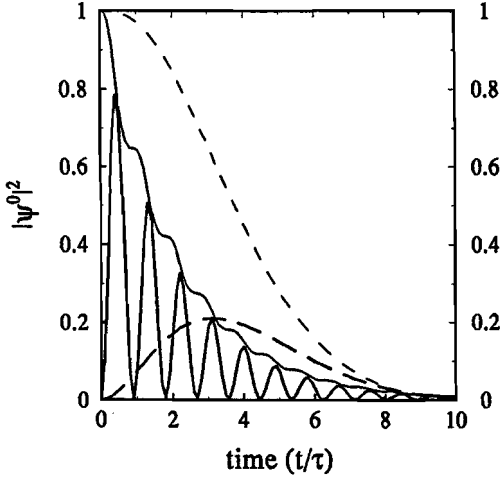


Figure 2.3: Zero-photon upper state population $|C_e^0(t)|^2$ (heavy lines) (equal to $w(t)/\Gamma$ with $w(t)$ the photon waiting time distribution) and the integrated distribution $|\Psi^0|^2$ (thin lines) for $s = 1$, $\Delta = 0$ (dashed lines) and for $s = 200$, $\Delta = \Gamma$ (full lines). In the latter set, the Rabi oscillations in the upper state population are clearly visible. In the former set, the expected quadratic increase of the upper state population near $t = 0$ is nicely visible.

For the simulation, we start out at $t = 0$ with an atom in the zero-photon ground state with $C_e^0 = 0$ and $C_g^0 = 1$ and pick a random number v . At $t = \tau_{MC}$, the atom spontaneously emits a photon. We assume no further interaction with the emitted photon. This allows us to restart the calculation in the zero-photon ground state, resetting the internal time of the atom to 0. To include light pressure in the simulation, we add the absorbed momentum in the direction of the laser $\hbar\mathbf{k}$ to the motion of the atom. At the same time a random recoil of the spontaneously emitted photon is added to the motion of the atom. The direction of the emitted photon is randomly determined in accordance with the correct angular distribution function.

We evaluate the function $|\Psi^0(t)|^2$ using computer-algebra to an explicitly real-valued expression, resulting in

$$|\Psi^0(t)|^2 = \frac{2\Omega^2}{4|\bar{\Omega}|^2} e^{-\Gamma t/2} \left[\frac{\Gamma}{\Gamma + \zeta^-} e^{-\zeta^- t/2} + \frac{\Gamma}{\Gamma - \zeta^-} e^{\zeta^- t/2} + \frac{2\Gamma}{\Gamma^2 + (\zeta^+)^2} (\zeta^+ \sin(\zeta^+ t/2) - \Gamma \cos(\zeta^+ t/2)) \right] \quad (2.11)$$

with the real-valued parameters

$$\zeta^\pm = \sqrt{2|\bar{\Omega}|^2 \pm 2(|\delta|^2 + \Omega^2)} \quad (2.12)$$

In figure 2.3 we plot $|\Psi^0(t)|^2$ and the upper state population $|C_e^0(t)|^2$ for two values of the laser detuning Δ and Rabi frequency Ω . The decay of $|\Psi^0(t)|^2$ is equal to the integral of the upper state population times the spontaneous decay rate:

$$1 - |\Psi^0(t)|^2 = \Gamma \int_0^t d\tau |C_e^0(\tau)|^2 \quad (2.13)$$

or in differential form

$$\Gamma |C_e^0(t)|^2 = -\frac{d}{dt} |\Psi^0(t)|^2 \quad (2.14)$$

2.3.2 Numerical implementation

We worked this out numerically in a one dimensional simulation and extended it to a multilevel atom. The procedure starts out assigning the atom a random, 'pure' magnetic sublevel and a momentum in the direction of the laser $p = 0$. For 'pure' σ or π laser polarizations, as in our experiment, the lower sublevel is coherently coupled with only one magnetic sublevel of the upper state. The Rabi frequency for this coupling is determined by the laser intensity and the Clebsch-Gordan coefficient for the transition. Hence we can calculate the waiting time to the next spontaneous emission by solving equation (2.10). This is accomplished by applying a bisection interpolation algorithm to a logarithmic transform of equation (2.11). At such an event, a photon recoil momentum in the direction of the laser is added to the momentum of the atom. We consider the spontaneous decay to end up in another 'pure' magnetic substate, which is randomly chosen with the correct branching ratio's (proportional to the squared Clebsch-Gordan coefficients). Decay to a coherent superposition of groundstates is not included. A random direction of the spontaneously emitted photon is chosen, with the correct angular dependence connected to either σ^+ , σ^- or π decay and the connected recoil is also added to the momentum of the atom. The calculation is now restarted with an atom in the ground state with a changed momentum p and magnetic sublevel m_g . The Doppler shift connected to the momentum of the atom is included in the simulation by including it in the effective detuning of the laser. The experimental interaction length is, for a given axial velocity, directly translated to the interaction time in the simulation. Also the initial momentum spread is put in explicitly. To reduce the statistical errors in the simulation, 100,000 atom trajectories are calculated for each simulation. The time needed for one simulation is about one hour on an IBM RS6000/320 workstation.

In figure 2.4 simulated deflected beam profiles are shown for σ and π excitation,

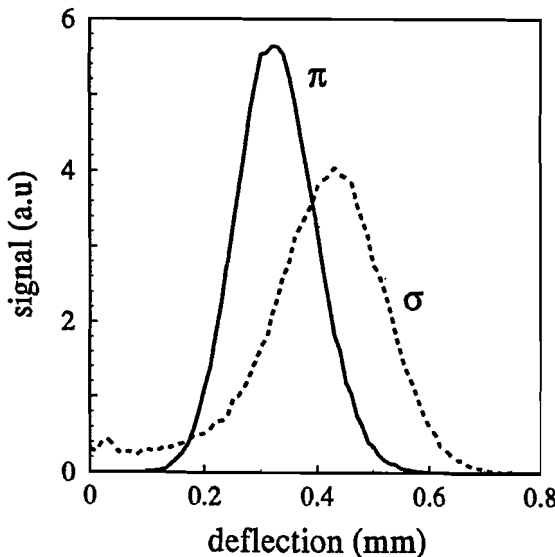


Figure 2.4: *Simulated deflected beam profile for σ^+ (dotted line) and π (full line) excitation. Note the undeflected tail in the σ^+ profile, caused by the slow evolution to the equilibrium distribution over the magnetic substates.*

both at $s = 1$. Here, as in the following, the saturation parameter s is specified with respect to the $m_g = 2 \rightarrow m_e = 3$ transition for σ^+ excitation. For σ excitation, the Clebsch-Gordan coefficients, (see table 2.1) vary over a factor 15 over the magnetic substates. From the slow evolution of the distribution over the substates from the initial statistical mixture to the purely polarized equilibrium distribution results a large spread in the number of excitations and thus a much larger observed value of $Q_{J=2 \rightarrow J=3}$. For linear excitation, the Clebsch-Gordan coefficients do not vary more than a factor of 2. In this case, the atoms are quickly optically pumped to an equilibrium distribution over the substates, resulting in an effective averaging of the excitation rate. In the figure, the large, hardly deflected tail for σ excitation is clearly visible, as well as the sub-Poissonian statistics for π excitation.

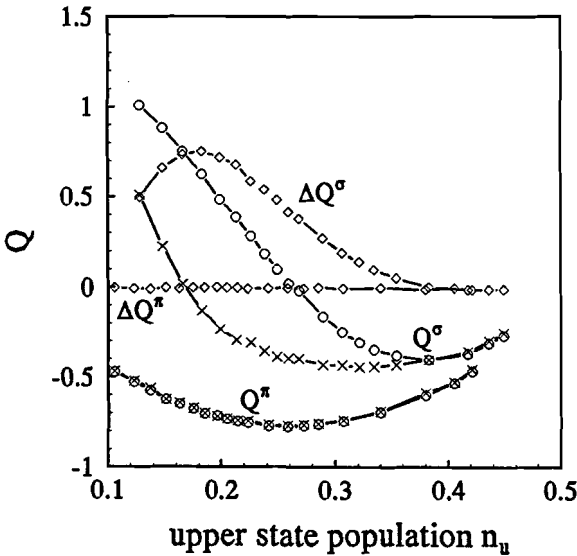


Figure 2.5: Q_{MC} extracted from the Monte-Carlo calculations, as determined from the Gaussian fit parameters (\times) and the directly calculated values (\circ) as a function of the laser intensity for σ and π excitation. The differences ΔQ^σ and ΔQ^π are indicated as well (\diamond). While for π excitation the correction is negligible, a large deviation is visible for σ excitation.

For the comparison of the Monte-Carlo simulation and the experiment, the simulated beam profile is subjected to the same analysis as the experimental data (see next section). Because of the non-Gaussian character of the deflected peak, especially with weak σ^+ excitation, the Gaussian fit does not give the exact value of $\langle \Delta N^2 \rangle$ and $\langle N \rangle$. This leads to a correction for the values determined from the Gaussian fit. In figure 2.5 the values of Q obtained directly from the spread in the number of scattered photons in the simulation are plotted as well as the values as determined from the Gaussian fit of the simulated deflected beam profile. For π excitation, the deviation never exceeds 0.05 in Q , but for σ excitation it can be as large as 0.75, as shown in the figure. This correction has been assumed to hold for the experimental data as well, enabling the 'real' experimental value of $\langle \Delta N^2 \rangle$ and hence $Q_{J=2 \rightarrow J=3}$ to be determined from the Gaussian fit results. It should be stressed, that the correction procedure does not affect the comparison of the calculated and experimental values as both data sets are affected simultaneously in the same fashion.

2.4 Data analysis and results

For an experimental deflected beam profile, at each detector position a time-of-flight spectrum is taken. The measured counts in one particular time-of-flight channel at different detector positions form a deflected beam profile for a mono-energetic atomic beam. Such a deflected beam profile for 1000 ms^{-1} atoms is shown in figure 2.6. The peak on the left is due to ^{21}Ne and ^{22}Ne atoms as well as ^{20}Ne atoms in the 3P_0 state, which all are not resonant with the laser. This peak serves as an excellent calibration of both the zero of the deflection scale and the instrumental beam width. The peak on the right is formed by the resonant 3P_2 atoms, which are deflected. The total profile is fitted with two Gaussians by a least-squares procedure, represented by the solid line. In the rest of the analysis, the width and the position of the deflected beam are determined from the fitted profile.

In figure 2.6 a simulated profile assuming Poissonian photon statistics (represented by the dashed line) is also displayed. The measured (and fitted) profile is obviously much narrower than this simulated profile, indicating a smaller spread in number of spontaneous emissions and thus a sub-Poissonian photon distribution. Q_{exp} can be extracted from the spread in momentum of the deflected beam using equation (2) from reference [7]:

$$\langle(\Delta p)^2\rangle = \langle(\Delta p_0)^2\rangle + (\hbar k)^2 [\langle(\Delta N)^2\rangle + \alpha \langle N\rangle], \quad (2.15)$$

which splits the momentum variance into contributions from the variance $\langle(\Delta p_0)^2\rangle$ before deflection, from the variance $\langle(\Delta N)^2\rangle$ of the photon number distribution and the variance $\alpha\langle N\rangle$ resulting from the angular distribution of the spontaneous-emission induced recoils. The factor α in the last contribution equals $\frac{2}{5}$ for a pure two-level system. In our case, α depends on the actual substate distribution. For the equilibrium distributions for circular and linear polarization, α equals $\frac{2}{5}$ and $\frac{16}{45}$, respectively. In view of the long interaction time in our experiments, the equilibrium values have been

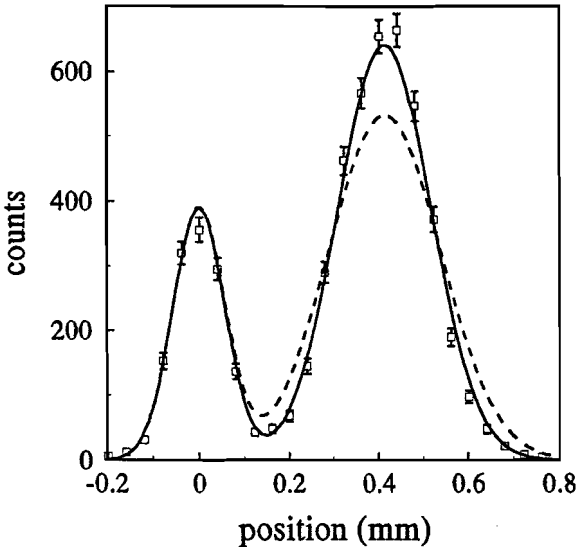


Figure 2.6: An experimental deflected beam profile. The undeflected peak on the left is formed by atoms in the 3P_0 state and other isotopes of neon. The deflected and broadened peak on the right. The solid line represents a fit to two Gaussian profiles. The dashed line indicates the expected deflected beam profile for Poissonian photon statistics.

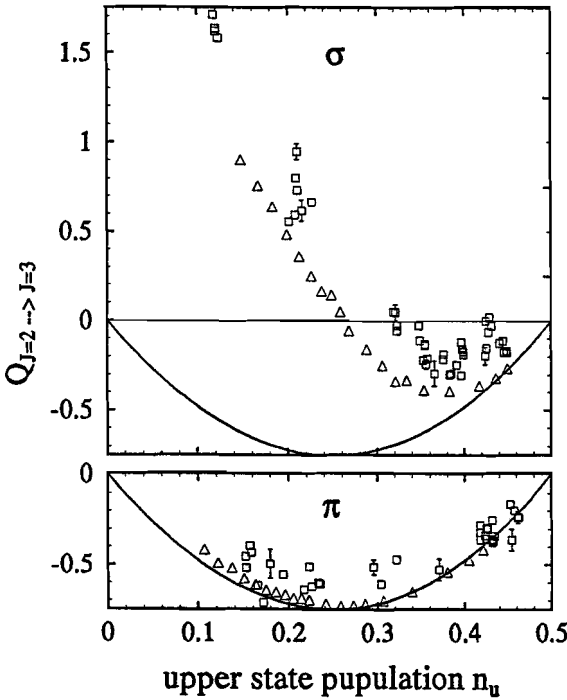


Figure 2.7: The value of $Q_{J=2 \rightarrow J=3}$ as a function of the upper state population for π excitation and for σ excitation for zero laser detuning. The experimental data and the results of the Monte-Carlo simulation are represented by squares and triangles respectively. The analytical two-level formula is indicated by the full line.

used.

The average deflection is proportional to the average upper state population $n_u \equiv \langle N \rangle \tau / T$. For a two-level system the upper state population is connected to the laser intensity by $n_u = s / (2(s + 1))$. Rewriting Mandel's formula as a function of n_u , we arrive at the simple quadratic expression

$$Q = 12n_u \left(n_u - \frac{1}{2} \right), \quad (2.16)$$

which allows us to plot the experimental results in a meaningful way without an explicit calibration of the laser power. In our analysis the broadening of the deflected peak is corrected for the instrumental beam width, variations in the laser power and the residual velocity spread. This analysis gives $Q_{\text{exp}} = -0.58 \pm 0.05$ for the profile in figure 2.6.

In the figure 2.7 the results for $Q_{J=2 \rightarrow J=3}$ from the experiments, from the Monte-Carlo simulation and the analytical formula are displayed for a wide range of laser intensities (from 20 to $800 \mu\text{W}/\text{mm}^2$). For one experimental data point, all time-of-flight channels in one measurement have been treated separately and the resulting Q -values are averaged afterwards. The dramatic deviation of our measured Q and the analytical formula for σ^+ excitation is also caused by the large transient effect due to the differing Clebsch-Gordan coefficients for σ excitation, as discussed in section 2.2.3. The Monte-Carlo results however, coincide nicely with our measured results. For π excitation, the differences between the simulation, the experimental results and the analytical formula are small. However, the experimental points seem to be systematically somewhat too

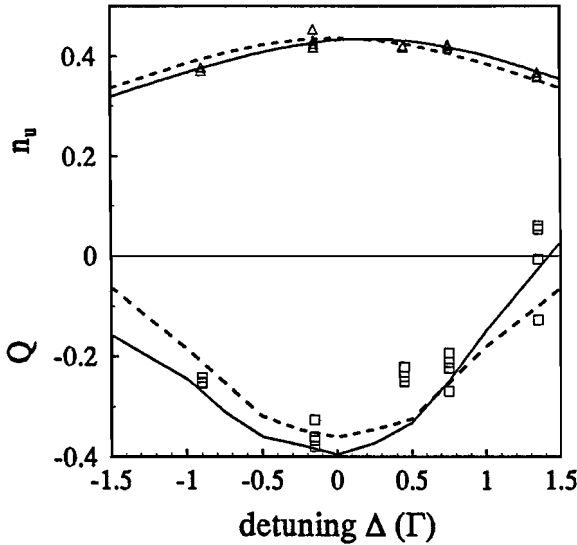


Figure 2.8: The upper state population (upper part) and the value of $Q_{J=2 \rightarrow J=3}$ (lower part) as a function of the laser detuning at a saturation parameter $s = 10$ ($I = 400 \mu\text{Wmm}^{-2}$ for π excitation). The results of the simulation are represented by the full lines, the analytical formula is represented by the dashed line.

high. Since our comparison between theory and experiment does not have any free parameters, we cannot explain this phenomenon.

The dependence of n_u and $Q_{J=2 \rightarrow J=3}$ on the laser detuning Δ for linearly polarized light is shown in figure 2.8, as well as the analytical expression (2.3) for Q as a function of the detuning. These results have been taken at one value of the laser intensity ($\approx 400 \mu\text{W}/\text{mm}^2$). The n_u curve has been used to calibrate the detuning scale, which is not known absolutely. Again, simulation and experiment are in excellent agreement, demonstrating the rapid increase in Q with increasing detuning. As can be derived from equation (2.2), at large detuning super-Poissonian photon statistics ($Q > 0$) can occur. The parameter Q goes through zero at $\Delta = \pm\sqrt{\frac{3}{4}}\Gamma$, regardless of the laser intensity.

The asymmetry apparent in the curves is a consequence of the Doppler shift changing the effective laser detuning while the atomic beam is being deflected. At an upper state population $n_u = 0.4$, an atom scatters on the average ≈ 35 photons during the $1.75 \mu\text{s}$ interaction time. With a velocity change per photon $\hbar k/M = 3.1 \text{ cms}^{-1}$ the resulting velocity in the direction of the laser is $\approx 1.0 \text{ ms}^{-1}$, which introduces a Doppler shift of $\approx 1.6 \text{ MHz}$. While constituting a small effect at zero detuning, the effect is more pronounced at larger initial detuning where the excitation rate varies appreciably with the detuning. With ‘blue’ detuning, the Doppler shift connected to the deflection moves the atom closer to resonance, which increases n_u . Hence an atom that already emitted a photon will be more likely to emit another. This causes the atoms to have a larger momentum spread, and consequently will the measured value of Q_{exp} will be higher. The reverse is true for ‘red’ detuning: an atom that has not yet emitted a photon is closer to resonance than one that already did. This is one of the simplest forms of laser cooling of an atomic beam. Of course the analytical curve does not include this effect. In the measurements by Oldaker *et al.* this effect is also visible, but it remains unnoticed.

2.5 Conclusions

We have performed accurate measurements on the photon number statistics of spontaneous emission photons from atoms in a quasi-resonant laser field using the method suggested by Cook [17]. This method uses the direct relation between spontaneous emission and momentum transfer to an atom in a running light wave. The spread in the number of emitted photons directly translates into a spread in atomic beam deflection. We used the neon ${}^3P_2 \rightarrow {}^3D_3$ closed level system as a two level system. The predominantly sub-Poissonian character of the photon number distribution, resulting in a smaller spread in the deflection of an atomic beam, has been confirmed by our measurements.

Mandel's Q -parameter, which gives the deviation from Poissonian photon statistics, has been measured for a wide range of driving field intensities and for a number of values of the laser detuning. The experimental dependency on these parameters is shown to be in good agreement with our calculations based on a Monte-Carlo approach of spontaneous emission. However, the measured results for Q seem to be systematically somewhat too high. Whether this is a result of underestimating an experimental broadening effect or something more fundamental, is not yet understood.

In the simulation experimental details, such as the effects of magnetic degeneracy of the system, finite interaction length and the Doppler shift resulting from the induced deflection, are included. For linear laser polarization the results from the Monte-Carlo simulation differ very little from the simple analytical formulae given by Cook and Mandel (equation (2.2)). For circular polarization the differences are large due to the slow evolution to an equilibrium situation, but the agreement between simulation and experiment is still very good.

These measurements show, without the uncertainty introduced by small detection efficiencies, sub-Poissonian photon number statistics of spontaneous emission light from an atom in a strong (quasi-)resonant light field. This can be interpreted as a confirmation of the quantum-mechanical nature of light.

Acknowledgments

This work is financially supported by the Dutch Foundation for Fundamental Research on Matter (FOM)

References

- [1] H.J. Kimble and L. Mandel. Phys. Rev. **A13**, 2123(1976).
- [2] H.J. Carmichael, S. Singh, R. Vyas, and P.R. Rice. Phys. Rev. **A39**, 1200(1989).
- [3] L. Mandel. Opt. Lett. **4**, 205(1979).
- [4] R.J. Cook. Phys. Rev. **A22**, 1078(1980).
- [5] S. Singh. Opt. Comm. **44**, 254(1983).

- [6] H.F. Arnoldus and G. Nienhuis. *Optica Acta* **30**, 1573(1983).
- [7] R.J. Cook. *Phys. Rev.* **A23**, 1243(1981).
- [8] D. Lenstra. *Phys. Rev.* **A26**, 3369(1982).
- [9] K. Kaminishi. *J. Phys. Soc. Jap.* **53**, 1006(1984).
- [10] R. Blatt, W. Ertmer, P. Zoller, and J.L. Hall. *Phys. Rev.* **A34**, 3022(1986).
- [11] X.T. Zou and L. Mandel. *Phys. Rev.* **A41**, 475(1990).
- [12] R. Short and L. Mandel. *Phys. Rev. Lett.* **51**, 384(1983).
- [13] R. Short and L. Mandel. in *Coherence and Quantum Optics V.*, Proceedings of the Fifth Rochester Conference (Plenum, New York, 1984), p. 671.
- [14] T.W. Hodapp, G.W. Greenlees, M.A. Finn, and D.A. Lewis. *Phys. Rev.* **A41**, 2698(1990).
- [15] M.A. Finn, G.W. Greenlees, T.W. Hodapp, and D.A. Lewis. *Phys. Rev. A* **40**, 1704(1989).
- [16] F. Diedrich and H. Walther. *Phys. Rev. Lett.* **58**, 203(1987).
- [17] R.J. Cook. *Opt. Comm.* **35**, 347(1980).
- [18] C. Tanguy, S. Reynaud, and C. Cohen-Tannoudji. *J. Phys.* **B 17**, 4623(1984).
- [19] B.G. Oldaker, P.J. Martin, Ph. L. Gould, M. Xiao, and D.E. Pritchard. *Phys. Rev. Lett.* **65**, 1555(1990).
- [20] M.D. Hoogerland, M.N.H. Wijnands, H.J. Senhorst, H.C.W. Beijerinck, and K.A.H. van Leeuwen. *Phys. Rev. Lett.* **65**, 1559(1990).
- [21] E.R.T. Kerstel, C.P.J.W. van Kruysdijk, J.C. Vlugter, and H.C.W. Beijerinck. *Chem. Phys.* **121**, 211(1988).
- [22] B.R. Mollow. *Phys. Rev.* **A12**, 1919(1975).
- [23] M.J. Verheyen, H.C.W. Beijerinck, J.P.J. Driessen, and N. F. Verster. *J. Phys.* **B10**, 15(1984).
- [24] H.C.W. Beijerinck. PhD thesis, Eindhoven University of Technology, 1975.
- [25] 4-dicyanomethylene-2-methyl-6(*p*-dimethyl-amino styryl)-4H-pyran.
- [26] M.J. Verheyen, H.C.W. Beijerinck, and N.F. Verster. *J. Phys.* **E15** 1198(1982).
- [27] R. Dum, P. Zoller, and H. Ritsch. *Phys. Rev.* **A45**, 4879(1992).
- [28] J. Dalibard, Y. Castin, and K. Mølmer. *Phys. Rev. Lett.* **68**, 580(1992).

Chapter 3

Force, diffusion and channeling in sub-Doppler laser cooling

M.D. Hoogerland, H.F.P. de Bie, H.C.W. Beijerinck
and K.A.H. van Leeuwen

*Eindhoven University of Technology,
P. O. Box 513 5600 MB Eindhoven, the Netherlands*

P. van der Straten

*Fysisch Laboratorium, Rijksuniversiteit Utrecht,
P.O. Box 80000, 3508TA Utrecht, The Netherlands.*

E.J.D. Vredenburg and H.J. Metcalf
State University of New York at Stony Brook, NY 11794.

Abstract

We present the first direct measurements of sub-Doppler cooling forces as well as the diffusion coefficients in these processes as a function of the initial velocity v_{\perp} . The deflection of an extremely well collimated atomic beam by a well-defined laser field is measured to determine the average force. The initial velocity of the atoms in the direction of the laser beams is varied in the range $-1 \leq v_{\perp}(\text{ms}^{-1}) \leq 1$ by changing the angle between atomic- and laser beams. The diffusion coefficient is determined from the broadening of the atomic beam profile. The experimental results are compared to Quantum Monte-Carlo simulations and semiclassical calculations. We observe excellent agreement. In the $\sigma^+\sigma^-$ cooling configuration, we observe transient effects due to the slow evolution of the distribution over the magnetic sublevels to an equilibrium. We also demonstrate channeling of atoms in weak standing waves and demonstrate the validity of the well-known Sisyphus picture for the $\pi^x\pi^y$ cooling scheme.

3.1 Introduction

The concept of cooling atoms with laser light to low temperatures was first proposed by Hänsch and Schawlow [1] and by Wineland and Dehmelt [2]. When a moving atom is placed in a pair of counterpropagating, red-detuned laser beams, it sees the counterpropagating laser beam blue-shifted and thus closer to resonance than the co-propagating. Thus more photons are scattered from the former beam, and an effective force is exerted on the atom. Near zero velocity, the force on the atom is directed against and proportional to the atomic velocity. Consequently, the atom feels a friction force and the atomic velocity distribution is narrowed. At the same time, the atomic velocity distribution is broadened by the random recoils of the spontaneously emitted photons. Thus, the minimum width of the Gaussian velocity distribution is equal to the Doppler limit, corresponding to temperatures in the milliKelvin range.

Apart from these 'dissipative' forces, atoms can also experience purely conservative forces. In a strong light field, the atomic levels are shifted by the AC Stark shift or light shift. Consequently, a gradient in light shift can also pose a considerable force on atoms. Combinations with dissipative effects have proven to yield extremely strong cooling forces [3]. Using only this gradient or dipole force, optical elements for atoms have been designed: mirrors, lenses and beamsplitters [4, 5].

The field of laser cooling has recently experienced an increasing activity in both theory and experiment. A large number of practical applications in other fields have been put forward [6, 7], and cooling to temperatures far below the 'Doppler limit' has been demonstrated [8, 9, 10]. The theoretical understanding of laser cooling processes has grown rapidly over the last few years and these very low temperatures were explained [11, 12, 13]. For a multilevel atom in some particular laser configurations the ratio of the diffusion constant to the friction coefficient, that determines the final temperature, can be much smaller than is the case in Doppler cooling. Semiclassically, the sub-Doppler cooling force $F(v)$ can be calculated in one dimension in steady state by solving the optical Bloch equations for a slowly moving atom in a classical laser field. Also the diffusion constant $D(v)$ can be calculated as the time autocorrelation function of the force. For more rigorous calculations the atomic motion has to be quantized, as recently discussed by Dum *et al.* [14, 15].

Experimentally however, there is less information available. The only experimental information so far is the final temperature resulting from the cooling process, which only reflects the ratio of the damping coefficient $(dF/dv)_{v=0}$ to the diffusion coefficient $D(0)$ at zero velocity [9, 8]. Other experiments have only studied the non-dissipative interaction in strong laser fields [16, 17].

In this paper, we present a large set of measurements investigating the dynamics of the cooling process. We study the deflection of a well-collimated atomic beam intersecting a (quasi-)standing laser field at a well defined angle, in the order of 1 mrad. This can be seen as a one dimensional experiment: the velocity in the direction of the laser field, that is less than 1 ms^{-1} , is influenced by the interaction with the laser light. The longitudinal velocity of the atomic beam, which is in the order of 1200 ms^{-1} , is hardly influenced by the interaction with the laser light. The Gaussian laser beam profile in this direction can be treated as a variation of the laser intensity in time. The initial velocity in the direction of the laser beam can be varied by displacing the second

collimating slit. The width (rms spread) of the velocity distribution in this direction is much smaller than a single photon recoil. It should be stressed that the atomic motion can thus be treated as one-dimensional in the direction of the laser beam. The velocity distribution is modified by the interaction with the laser field: it will be shifted due to an average force on the atoms and broadened, for instance by spontaneous emission heating.

If the force on the atoms exerted by the laser field does not strongly depend on the position of the atoms in the (quasi-)standing wave, as in the $\sigma^+\sigma^-$ configuration, the average velocity change Δv of the atoms can directly be translated to an average (cooling) force by representing the Gaussian laser beam profile with an equivalent square profile (see section 3.4.3).

The broadening of the atomic beam can then be translated to a diffusion coefficient. In configurations with a spatially modulated light shift, as in a pure standing wave (with either σ or π polarization) or the $\pi^x\pi^y$ cooling configuration, the force exerted on an atom strongly depends on the position of the atom in the standing wave. In this case the deflected beam profile cannot directly be translated to an average force and diffusion coefficient. However, our measurements clearly indicate channeling of the atoms in the spatially modulated light shift potentials.

This way we have measured deflected beam profiles for four polarization configurations as a function of the initial velocity at several values of the laser detuning Δ and laser intensity I . Thus we have a much more stringent check of the theory than measurements of the final temperature after a long interaction time, which only reflects the ratio of the diffusion coefficient and the damping at zero velocity. We compare our measured results with existing theories on laser cooling, and find in most cases excellent agreement. Moreover, we observe transient effects and channeling in potential wells during the cooling process. This way we come to new insights in the dynamics of the cooling process.

3.2 Classical and semiclassical theory

We compare our measured deflected beam profiles with several theoretical models. First we consider a simple physical picture of the interaction of the atoms with the laser light and implement this in a semiclassical rate-equation based Monte-Carlo simulation of the experiment. Channeling of atoms in a pure standing wave as well as the $\pi^x\pi^y$ cooling configuration are shown to be well understood using this simple model. Second, we use the semiclassical operator treatment of sub-Doppler cooling forces as given by Nienhuis *et al.* [13]. The steady-state drag forces as well as transient effects can be calculated for an arbitrary (one-dimensional) light field using this model. These calculations show fair agreement with the experimental data for all experimental laser configurations. Finally, we consider a fully quantummechanical Monte-Carlo simulation, as recently introduced by Dum *et al.* [14]. These calculations also show excellent agreement with the experimental data for all laser configurations.

3.2.1 Classical picture

A two-level atom in a laser field experiences a population-averaged ‘light shift’ or AC Stark shift equal to

$$\hbar\Omega_s = \frac{\hbar\Delta}{2} \log\left(1 + \frac{\Omega^2}{2\Delta^2}\right) \quad (3.1)$$

Here, $\Delta = \omega - \omega_0$ denotes the detuning of the laser field and Ω the Rabi frequency. In a pure standing wave of either linear or circular polarization, this means that the atom experiences a spatially modulated potential with maximum absolute values at the antinodes of the standing wave. If the kinetic energy of the atoms is smaller than the light shift in the antinodes, this means that the atoms will be channeled in the standing wave pattern. The classical particle trajectories in such a periodic potential can easily be calculated, and the resulting deflected beam profiles show a strikingly good agreement with the experimental data. In a numerical simulation of our experiment, we introduced magnetic substates, optical pumping between these substates and momentum diffusion by spontaneous emission in a Monte-Carlo like manner. We start out with an atom in a particular magnetic substate, and calculate the classical particle trajectory in the potential pattern. At a rate Γn_e , with Γ the natural linewidth of the transition and n_e the excited state population, photons are spontaneously emitted. Spontaneous decay may go to another magnetic substate, chosen with the correct probabilities given by the Clebsch-Gordan coefficients.

For the $\pi^x\pi^y$ cooling configuration, the well known physical Sisyphus picture is applicable [11]. In this configuration, the polarization of the resulting light field is spatially modulated. A moving atom thus experiences a constantly changing polarization of the light field. In a $J \rightarrow J+1$ transition, optical pumping in the light field will drive the atom to the most light shifted magnetic sublevel of the ground state. In case of red detuning, this is the sublevel that is lowest in energy. As the atom moves, it gets to a region with a different light polarization. The formerly most shifted sublevel has moved up in energy. This energy is taken from the kinetic energy, so the atom slows down. Then optical pumping will probably take the atom to the lowest sublevel again, from where it starts climbing the potential hill again. Optimal damping of the motion is achieved if the atom moves a quarter of a wavelength in one optical pumping time. Also in this configuration, atoms in a particular magnetic substate will be channeled in the spatially modulated potential. This is enhanced by the optical pumping to the deepest channel, that causes the cooling effect. For positive detuning, optical pumping will drive the atom to the magnetic sublevel that is highest in energy. Consequently, channeling will be suppressed for positive detuning and enhanced for negative detuning in this polarization configuration. This mechanism can easily be included in the classical rate-equation based Monte-Carlo simulation of the experiment.

For the $\sigma^+\sigma^-$ cooling configuration, it is impossible to perform such a simple simulation. Coherences between the ground states cause the cooling effect. These cannot be included in this treatment that only deals with the population of levels. The resulting polarization in the standing light field is linear everywhere, but with a spatially rotating polarization vector. If the atom moves through the light field, we can transform to a new coordinate system rotating with the laser polarization at a rate $k v$. As we do so, we introduce a topological magnetic field that mixes the magnetic sublevels. The resulting orientation of the atom is such that it ends up in a sublevel that has more

interaction with the counterpropagating laser beam. Thus a strong cooling effect is achieved.

For light atoms like sodium and neon, the Sisyphus cooling mechanism does not work so well to achieve low temperatures. The reason is that when the interaction strength is reduced to reduce the final temperature, the capture range of the force is also reduced. For very low excitation rates, the capture range becomes smaller than one photon recoil. Therefore, the $\sigma^+\sigma^-$ configuration that has a larger capture range works rather well to achieve low temperatures for these light atoms.

3.2.2 Semiclassical treatment

In the semiclassical model we consider an ensemble of point-like particles that is subject to a position and velocity dependent diffusion $D(v)$ and force $F(v)$. The evolution of the velocity distribution $W(v)$ is then governed by the Fokker-Planck equation. The average force and the diffusion coefficient are calculated using the operator description of sub-Doppler laser cooling by Nienhuis *et al.* [13]. We give a brief summary of this treatment, and apply it to simulate our experiment. For the calculations of steady-state drag forces with this method we refer to the article by Nienhuis.

The force and diffusion coefficients are calculated from

$$\mathbf{F}(\mathbf{v}) = \langle \hat{\mathbf{f}}(t) \rangle \quad (3.2)$$

$$2 \vec{\mathbf{D}}(\mathbf{v}) = \int d\tau \langle \hat{\mathbf{f}}(t) \hat{\mathbf{f}}(t + \tau) \rangle - \langle \hat{\mathbf{f}}(t) \rangle \langle \hat{\mathbf{f}}(t + \tau) \rangle + \text{C.C.} \quad (3.3)$$

with $\hat{\mathbf{f}}$ the Heisenberg force operator with expectation value $\langle \mathbf{f} \rangle = \text{Tr}(\sigma \hat{\mathbf{f}})$. Here, the density matrix σ describes the internal states of the ensemble of atoms.

The radiation field is described by the classical electric field

$$\mathbf{E}(\mathbf{r}, t) = \mathbf{E}_+(\mathbf{r})e^{-i\omega t} + \mathbf{E}_-(\mathbf{r})e^{i\omega t} \quad (3.4)$$

with ω the laser frequency. The field drives the transition between a lower level g and an upper level e , which both may be degenerate. In the rotating wave approximation, the atom-field coupling is governed by the Rabi operators $\hat{\mathcal{R}} = \boldsymbol{\mu}_{eg} \cdot \mathbf{E}_+ \hat{a} / \hbar$ and $\hat{\mathcal{R}}^\dagger = \boldsymbol{\mu}_{ge} \cdot \mathbf{E}_- \hat{a}^\dagger / \hbar$ with $\boldsymbol{\mu}_{eg} = \boldsymbol{\mu}_{ge}^*$ the atomic dipole matrix and \hat{a} and \hat{a}^\dagger the atomic lowering and raising operators respectively.

In the low-velocity limit ($v \ll \Gamma/k$), we assume the decay of the optical coherences to their stationary values to be rapid compared to the rate of change of the field that the atoms feel. Hence we assume $\dot{\sigma}_{eg} = \dot{\sigma}_{ge} = 0$, which allows us to eliminate the optical coherences and reduce the evolution equations for the density matrix to the form:

$$\begin{aligned} \frac{d\sigma_{ee}}{dt} &= -(\Gamma + i\hat{\mathcal{L}})\sigma_{ee} - \hat{\mathcal{R}}\left(\frac{\Gamma}{2} + i\Delta + i\hat{\mathcal{L}}\right)^{-1}(\hat{\mathcal{R}}^\dagger\sigma_{ee} - \sigma_{gg}\hat{\mathcal{R}}^\dagger) \\ &\quad + \left[\left(\frac{\Gamma}{2} - i\Delta + i\hat{\mathcal{L}}\right)^{-1}(\hat{\mathcal{R}}\sigma_{gg} - \sigma_{ee}\hat{\mathcal{R}})\right]\hat{\mathcal{R}}^\dagger \\ \frac{d\sigma_{gg}}{dt} &= \Gamma \sum_{\beta} \hat{Q}_{\beta}^\dagger \sigma_{ee} \hat{Q}_{\beta} - i\hat{\mathcal{L}}\sigma_{gg} - \hat{\mathcal{R}}^\dagger\left(\frac{\Gamma}{2} - i\Delta + i\hat{\mathcal{L}}\right)^{-1}(\hat{\mathcal{R}}\sigma_{gg} - \sigma_{ee}\hat{\mathcal{R}}) \\ &\quad + \left[\left(\frac{\Gamma}{2} + i\Delta + i\hat{\mathcal{L}}\right)^{-1}(\hat{\mathcal{R}}^\dagger\sigma_{ee} - \sigma_{gg}\hat{\mathcal{R}}^\dagger)\right]\hat{\mathcal{R}} \end{aligned} \quad (3.5)$$

Herein, we introduced the Liouville operator $\hat{\mathcal{L}}$ that, in our case, denotes the commutator with the Zeeman Hamiltonian. The dimensionless dipole operators \hat{Q}_β account for the anisotropy of spontaneous decay and are defined by their matrix elements as Clebsch-Gordan coefficients. In the low-intensity limit, we assume that the excited state submatrix σ_{ee} adiabatically follows the lower state submatrix σ_{gg} . This is justified if the Rabi frequency Ω , determined by the strength of the interaction operator $\hat{\mathcal{R}}$, is small compared to the natural linewidth Γ . We find

$$\sigma_{ee} = \frac{1}{\Gamma + i\hat{\mathcal{L}}} \left[\hat{\mathcal{R}} \frac{1}{\Gamma/2 + i\Delta + i\hat{\mathcal{L}}} \sigma_{gg} \hat{\mathcal{R}}^\dagger + \frac{1}{\Gamma/2 - i\Delta + i\hat{\mathcal{L}}} \hat{\mathcal{R}} \sigma_{gg} \hat{\mathcal{R}}^\dagger \right] \quad (3.6)$$

When this is substituted in equation 3.5, we find a closed evolution equation for the lower state submatrix σ_{gg} .

The force operator $\hat{\mathbf{f}}$ is determined by the commutator of the momentum operator with the Hamiltonian and is given by

$$\hat{\mathbf{f}} = \hbar[\nabla\hat{\mathcal{R}} + \nabla\hat{\mathcal{R}}^\dagger] \quad (3.7)$$

We evaluate this for a one-dimensional laser field, with a time dependent amplitude. The force and diffusion coefficient working on an ensemble of atoms are now calculated as follows: We start out with the ensemble of atoms located at position \mathbf{r} and all polarized with a magnetic moment m in the direction of the laser beam. We follow the evolution of the density matrix, while at each time calculating the new position, momentum and force. This results in ‘classical particle trajectories’ for the center of mass of the atomic ensemble. The diffusion coefficient is calculated afterwards as the time autocorrelation of the force along the trajectory, as given in equation 3.3. This process is repeated for a number of different starting positions in the standing wave, for a number of initial velocities and for all particular magnetic sublevels. Note

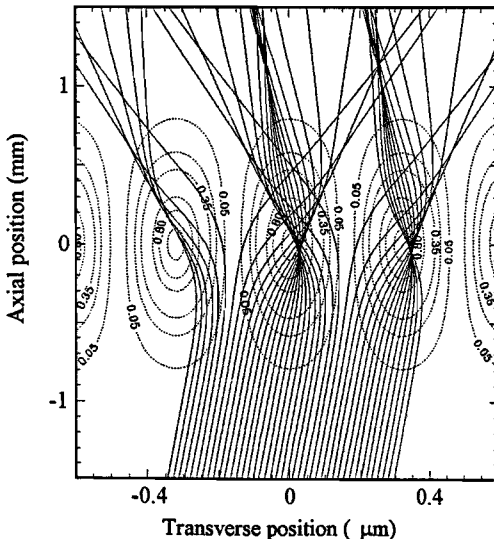


Figure 3.1: ‘Classical atom trajectories’ as calculated by the semiclassical treatment in a standing wave of linearly polarized light. Note that the exit velocity mostly depends on the incoming position in the standing wave.

that starting out with a density matrix containing an isotropic distribution over the magnetic substates gives a different result than starting the calculation with only a single magnetic substate and averaging this afterwards. The latter procedure more accurately reproduces the actual final momentum distribution of the atomic ensemble, as the former procedure can only lead to a Gaussian distribution.

In figure 3.1 ‘classical particle trajectories’ as calculated using the semiclassical model for atoms with an initial velocity of 0.1 ms^{-1} for a 20 initial positions in a linearly polarized standing laser wave are shown. The light intensity as a function of the position is displayed as a contour plot in dashed lines. The particle trajectories are averaged over the different magnetic substates. Note that for different initial positions in the standing wave, we get dramatically different exit velocities. This is observed in the experiment as a strong broadening of the atomic beam. Note also that in this particular case there is a focal point almost in the middle of the standing wave: the dipole potentials induced by the laser field effectively act as a graded index lens for atoms with pitch 0.5. Consequently, a large fraction of the atoms has an final velocity $v_e = -v_i$.

3.3 Quantum Monte-Carlo treatment

3.3.1 Basic theory

The quantum Monte-Carlo treatment (QMC) is based on Mollow’s treatment of resonant light scattering. This treatment has been extended to a Monte-Carlo simulation for a running laser wave by Blatt *et al.* [18] and to arbitrary light field configurations by Dum *et al.* [14]. We briefly summarize this treatment.

For an atom in a light field, the total Hamiltonian \hat{H} is given by

$$\hat{H} = \frac{\hat{p}^2}{2M} + \hat{H}_{0A} + \hat{H}_{0F} + \hat{H}_I(t) \quad (3.8)$$

with \hat{p} is the momentum of the atom and M the mass. The operator $\hat{H}_{0A} = \omega_{eg} \hat{a}^\dagger \hat{a}$ is the Hamiltonian of the free atom, with $\hat{a} = |g\rangle\langle e|$ and $\hat{a}^\dagger = |e\rangle\langle g|$ the atomic lowering and raising operators respectively. The kets $|e\rangle$ and $|g\rangle$ are the time-independent excited and ground states of the atom. The operator \hat{H}_{0F} denotes the Hamiltonian of the free radiation field, and the interaction part \hat{H}_I is given by

$$\hat{H}_I(t) = -\boldsymbol{\mu}_{eg}^* \cdot \hat{\mathbf{E}}^\dagger \hat{a} + \text{H.C.} \quad (3.9)$$

Here, $\boldsymbol{\mu}_{eg}$ is the atomic dipole matrix and $\hat{\mathbf{E}}$ the electric field operator. Mollow used a canonical transformation to show that a single-mode coherent laser field can be treated classically, when the number of photons in all other modes of the field is zero for $t \rightarrow -\infty$. Therefore, the laser field can be represented by a complex vector $\mathcal{E}_c(\mathbf{r}, t)$. For instance, for a plane wave, we have $\mathcal{E}_c(z, t) = \mathcal{E}_0 e^{i(kz - \omega t)}$.

We assume that at time $t = 0$, all radiation modes except the laser mode are empty. We split the wavefunction $\Psi(\mathbf{r}, t)$ in partial wavefunctions $\Psi^n(\mathbf{r}, t)$ with n spontaneously emitted photons in modes k_1 through k_n as:

$$\Psi(\mathbf{r}, t) = \Psi^0(\mathbf{r}, t) + \sum_{n=1}^{\infty} \Psi^n(\mathbf{r}, t) \quad (3.10)$$

$$= C_g^0(\mathbf{r}, t)|g, \{0\} + C_e^0(\mathbf{r}, t)|e, \{0\} \quad (3.11)$$

$$+ \sum_k (C_g^{1k}(\mathbf{r}, t)|g, \hat{b}_k^\dagger\{0\} + C_e^{1k}(\mathbf{r}, t)|e, \hat{b}_k^\dagger\{0\}))$$

+ ...

$$+ \sum_{k_1 \dots k_n} (C_g^{nk_1 \dots k_n}(\mathbf{r}, t)|g, \hat{b}_{k_1}^\dagger \dots \hat{b}_{k_n}^\dagger\{0\} + C_e^{nk_1 \dots k_n}(\mathbf{r}, t)|e, \hat{b}_{k_1}^\dagger \dots \hat{b}_{k_n}^\dagger\{0\}))$$

For the partial wavefunction $\Psi^0(\mathbf{r}, t)$ a set of Schrödinger-like equations can be derived. The modulus $|\Psi^0(t)|^2 = |C_g^0(t)|^2 + |C_e^0(t)|^2$ is equal to the probability that no spontaneous emission has occurred until time t . The loss of probability $1 - |\Psi^0(t)|^2$ of the zero photon wavefunction is equal to the integral of the photon waiting-time distribution $W(t)$ as given by

$$1 - |\Psi^0(t)|^2 = \int_0^t W(t') dt' = \Gamma \int_0^t |C_e^0(t')|^2 dt' \quad (3.12)$$

In a Monte-Carlo implementation this integral of the photon waiting time distribution can be used to randomly determine the time at which the spontaneous emission takes place by taking a random number $\Upsilon \in [0..1]$ and solving the equation

$$1 - |\Psi^0(t)|^2 = \Upsilon \quad (3.13)$$

At this moment in the simulation, we assume no further interaction with the spontaneously emitted photon, and start over in the zero-photon ground state with $C_g(0) = 1$.

In case of a two-level atom in a running laser wave the complete time evolution of the coefficients C_g^0 and C_e^0 is given by Mollow [19]; it has been applied to a Monte-Carlo simulation of cooling processes and photon statistics by Blatt [18] and by us [20, 21], and generalized by Dum *et al.* [14] and Dalibard [15] *et al.* to an arbitrary light field and (magnetic) atomic substructure.

To include magnetic substructure, the wavefunction Ψ^0 can be expanded in time-independent states $|\alpha, m_\alpha\rangle$ with coefficients C_α and $\alpha = e$ or g . The superscript zero, denoting the fact that C_α only denotes that part of the wavefunction with no spontaneous emission yet, has been omitted. We furthermore introduce the operator \hat{p} with eigenfunctions $|p\rangle$ for atomic momentum in the direction of the laser. The motion perpendicular to the laser beam is treated classically. The product wavefunction is now represented by $|\alpha, m_\alpha, p\rangle$. If there is no spontaneous emission, the atomic momentum is quantized as $|p_0 + j\hbar k\rangle$ with p_0 the initial momentum and j an integer number. We now have a family \mathcal{F}_{p_0} of states that are internally coupled only by stimulated processes. The states of this family are denoted by $|\alpha, m_\alpha, j\rangle$ and have coefficients $C_{\alpha m_\alpha}^j$. The momentum eigenvalues are $p_0 + 2j\hbar k$ with j even for the ground states and j odd for the excited states, respectively. An atom can leave the family of states by spontaneous emission to another family $\mathcal{F}_{p_0'}$.

The equations of motion for the coefficients $C_{\alpha m_\alpha}^j(t)$ for a family with initial momentum $p_0 = \hbar k_0$ are in a one-dimensional laser configuration in z direction given

by

$$i\hbar \frac{d}{dt} C_{g m_g}^j(t) = \left[\frac{\hbar^2}{2M} (jk + k_0)^2 + \mu_B g_{j_g} B^z m_g \right] C_{g m_g}^j(t) \quad (3.14)$$

$$\begin{aligned} &+ \frac{\mu_B g_{j_g}}{2} (B^x - iB^y) \sqrt{(j_g - m_g)(j_g + m_g + 1)} C_{g(m_g+1)}^j(t) \\ &+ \frac{\mu_B g_{j_g}}{2} (B^x + iB^y) \sqrt{(j_g + m_g)(j_g - m_g + 1)} C_{g(m_g-1)}^j(t) \\ &+ \frac{\hbar \Omega_{eg}^*}{2} (j_g \ m_g \ 1 \ 1 | j_e \ (m_g - 1)) \left[\epsilon_1^{+*} C_{e(m_g-1)}^{j+1}(t) + \epsilon_1^{-*} C_{e(m_g-1)}^{j-1}(t) \right] \\ &+ \frac{\hbar \Omega_{eg}^*}{2} (j_g \ m_g \ 1-1 | j_e \ (m_g + 1)) \left[\epsilon_{-1}^{+*} C_{e(m_g+1)}^{j+1}(t) + \epsilon_{-1}^{-*} C_{e(m_g+1)}^{j-1}(t) \right] \end{aligned}$$

$$i\hbar \frac{d}{dt} C_{e m_e}^j(t) = \left[\frac{\hbar^2}{2M} (jk + k_0)^2 - \hbar(\Delta + i\Gamma/2) + \mu_B g_{j_e} B^z m_e \right] C_{e m_e}^j(t) \quad (3.15)$$

$$\begin{aligned} &+ \frac{\mu_B g_{j_e}}{2} (B^x - iB^y) \sqrt{(j_e - m_e)(j_e + m_e + 1)} C_{e(m_e+1)}^j(t) \\ &+ \frac{\mu_B g_{j_e}}{2} (B^x + iB^y) \sqrt{(j_e + m_e)(j_e - m_e + 1)} C_{e(m_e-1)}^j(t) \\ &+ \frac{\hbar \Omega_{eg}}{2} (j_g \ (m_e + 1) \ 1 \ 1 | j_e \ m_e) \left[\epsilon_1^+ C_{g(m_e+1)}^{j-1}(t) + \epsilon_1^- C_{g(m_e+1)}^{j+1}(t) \right] \\ &+ \frac{\hbar \Omega_{eg}}{2} (j_g \ (m_e - 1) \ 1-1 | j_e \ m_e) \left[\epsilon_{-1}^+ C_{g(m_e-1)}^{j-1}(t) + \epsilon_{-1}^- C_{g(m_e-1)}^{j+1}(t) \right] \end{aligned}$$

Here, the Rabi frequency is given by $\Omega_{eg} = \Gamma(I/(2I_0))^{\frac{1}{2}}$ with I_0 the saturation intensity for the $m_g = 2 \rightarrow m_e = 3$ transition. $B^{(x,y,z)}$ denote the cartesian components of the magnetic field. The relative strengths of the orthogonal circular polarization components $+1$ and -1 of the individual laser beams in the $+$ and $-$ directions are denoted by $\epsilon_{\pm 1}^{\pm}$.

3.3.2 Numerical implementation

For a simulation of our experiment, we chose a basis set of 30–40 momentum states to study the momentum evolution of the atomic wave. Since our experiment is done with metastable neon, we evaluate a $J = 2 \rightarrow J = 3$ transition. With $12=5+7$ magnetic substates taken into account, we thus integrate 360 coupled differential equations using the well-known NAG routine D02BHF. The interaction time is divided in small time intervals, in which we assume a constant laser power. We start out with an atomic plane wave with momentum p_0 , a random angular momentum m_g in the direction of the laser and in the ground state. This means that all coefficients $C = 0$, except for $C_{g m_g}^0 = 1$. We integrate the equations of motion for the coefficients C until time τ_{MC} , at which equation 3.13 is fulfilled, with $|\Psi^0(t)|^2 = \sum_j \sum_\alpha \sum_{m_\alpha} |C_{\alpha m_\alpha}^j|^2$. At this moment, we assume a photon to be spontaneously emitted. We assume no further interaction with the spontaneously emitted photon. We add a random recoil to the initial momentum k_0 and collapse the wavefunction to the ground state as follows:

$$C_{g m_g}^j(0) \leftarrow \frac{\sum_{m_e} (j_g \ m_g \ 1 \ (m_e - m_g) | j_e \ m_e) C_{e m_e}^j(\tau_{MC})}{|\Psi^0(\tau_{MC})|^2} \quad (3.16)$$

$$C_{e m}^j(0) \leftarrow 0 \quad (3.17)$$

Then, the integration is restarted with these values. The resulting momentum distribution over many shots is binned. For 1000 shots, the computing time is about two hours on an IBM RS6000/320 workstation.

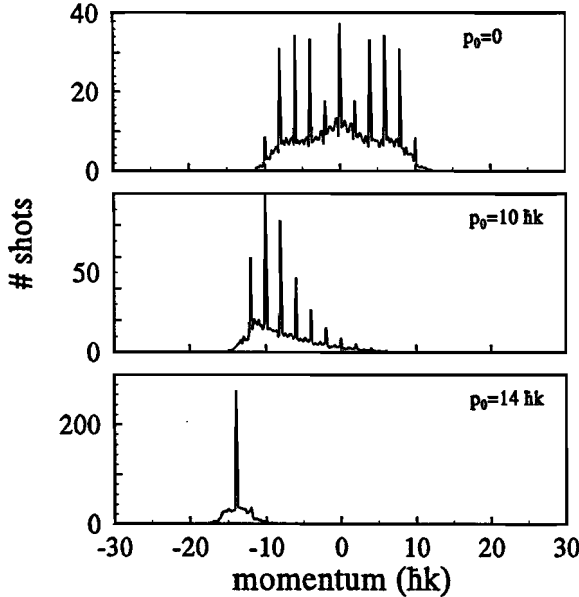


Figure 3.2: Final momentum distributions from the QMC calculations for three different initial momenta. The laser configuration is $\pi^x\pi^y$, the detuning $\Delta = -3.8\Gamma$ and $s = I/I_0 = 6.2$ for all initial momenta.

As a result, we obtain the momentum distribution of the deflected beam profile. In figure 3.2 this distribution is shown for three different values of the initial momentum p_0 , in the $\pi^x\pi^y$ laser configuration with a detuning $\Delta = -3.8\Gamma$ and an on-resonance saturation parameter at the center of the laser beam profile $s = I/I_0 = 6.2$. In this situation, channeling of the atoms in the periodic potential induced by the light field should play an important role. For $p \approx 12\hbar k$ the kinetic energy of the atoms is equal to the maximum light shift. The sharp peaks in the figures represent the fraction of the atoms that has not spontaneously emitted a photon during the interaction. We observe that for initial momentum $p_0 = 0$, the atomic momentum distribution is redistributed over many momentum states by absorption-stimulated emission cycles. For $p_0 = 10\hbar k$, with a kinetic energy slightly smaller than the maximum light shift, the atoms are clearly pushed to $p = 0$ by this process. For $p_0 = 14\hbar k$, the kinetic energy of the atoms is larger than the light shift and the stimulated redistribution process does not seem to occur. Only a single sharp peak at $p = p_0$ remains.

In figure 3.3 the resulting momentum distributions at lower intensity ($s \approx 4$) and smaller detuning ($\Delta = -2\Gamma$) are shown for the $\sigma^+\sigma^-$, $\pi^x\pi^y$, $\pi^x\pi^x$ and $\sigma^+\sigma^+$ laser configurations for $p_0 = 0$. In the latter two profiles, a strong redistribution is observed, as visible in the strong broadening of the distribution. For the former two profiles, a more Gaussian distribution is obtained, indicating that most atoms have spontaneously emitted a photon.

For the comparison of simulated momentum distributions with the experimental data in section 3.5, the simulated profiles are then convoluted with the experimental resolution. Of course all sharp peaks will then disappear.

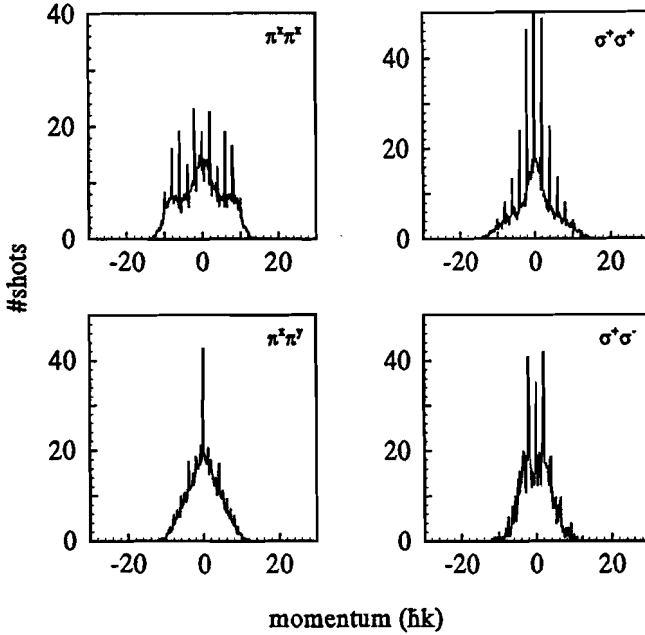


Figure 3.3: Final momentum distributions from the QMC calculations for four different polarization configurations for initial momentum $p_0 = 0$. The detuning $\Delta = -2\Gamma$ for all graphs. The saturation parameter $s = 4.1$ for the $\pi^x\pi^y$ and $\pi^x\pi^x$ configurations and $s = 3.6$ for the $\sigma^+\sigma^-$ and $\sigma^+\sigma^+$ configurations.

3.4 Experiment

3.4.1 Atomic beam setup

We use a supersonic beam of neon atoms, partly excited in a DC-discharge to the metastable 3P_2 and 3P_0 states. The discharge runs through the $\approx 100 \mu\text{m}$ nozzle. This type of metastable source creates a beam with an average velocity of $\approx 1200\text{ms}^{-1}$ and a velocity spread (FWHM) of $\approx 300\text{ms}^{-1}$. The fraction of metastable atoms in the atomic beam is $\approx 10^{-5}$, leading to a typical center-line beam intensity of $\approx 1.5 \cdot 10^{13}\text{s}^{-1}\text{sr}^{-1}$. Typical operating conditions are a source inlet pressure of 30 Torr, a discharge voltage of about 400 V and a discharge current of 10 mA. The flat plate anode of the discharge also acts as a skimmer and as the first beam collimating slit.

The vacuum setup has been used in several other experiments on light forces on atoms [10, 20, 21]. A number of differential pumping stages decreases the gas load on the setup, resulting in a residual gas pressure after the second differential pumping section of $\approx 2 \cdot 10^{-8}$ Torr. This pressure is achieved by using both oil diffusion pumps and a 20 K cryopump.

The atomic beam is collimated to $< 10^{-4}$ rad using two $50 \times 500 \mu\text{m}$ slits located 5 mm and 1948 mm downstream from the metastable atom source (figure 3.4). The

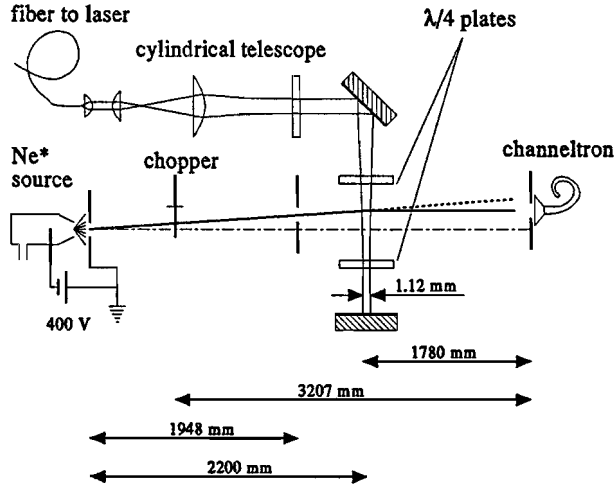


Figure 3.4: An overview of the experimental setup. The atomic beam is collimated using two $50 \times 500 \mu\text{m}$ slits. It is intercepted by a (quasi) standing laser field with a Gaussian waist radius of 0.56 mm on the backreflecting mirror. The deflected beam profile is analyzed using a channeltron electron multiplier with a $50 \times 2000 \mu\text{m}$ entrance slit. The atomic beam is chopped to enable time-of-flight analysis of the atomic beam.

latter slit can be moved by a stepper-motor to define the initial velocity of the atomic beam in the direction of the laser. By moving this slit over 2 mm , the initial velocity v_{\perp} can be changed in the range $-1 \leq v_{\perp} (\text{ms}^{-1}) \leq +1$ with high selectivity. In figure 3.5 the spread in v_{\perp} of the atomic beam is plotted as a function of v_{\perp} . At $v_{\perp} = 0$, the spread is only due to the limited collimation of the beam. At larger v_{\perp} , the longitudinal velocity spread is the most important factor. However, in this range the force on the atoms does not strongly depend on the velocity. The Doppler cooling force is very small over the whole velocity range. All slits are carefully aligned to be parallel. The interaction region is located 2200 mm downstream from the source.

The beam profile after deflection is analyzed using a stepper-motor driven movable channeltron electron multiplier with a $50 \times 2000 \mu\text{m}$ entrance slit located 1780 mm downstream from the interaction region (figure 3.4). When a metastable atom hits the channeltron, an electron is emitted that is amplified in the channeltron. The delaytime spread of this detection system is less than 100 ns . The detection efficiency is estimated to be in the range between 0.2 and 1 for metastable neon atoms. Also UV-light from the discharge beam source detected. Ground state atoms and residual gas atoms are not detected.

The atomic beam is chopped mechanically to enable time-of-flight velocity analysis of the deflected atoms. The chopper is located 3207 mm upstream from the detector, giving a typical time-of-flight from the chopper to the detector of 2.7 ms at an average beam velocity of 1200 ms^{-1} . The chopper has an open time of $\approx 130 \mu\text{s}$. The velocity distribution is analyzed using a multi-scaler in 50 time channels of each $100 \mu\text{s}$ long. This yields a (FWHM) velocity resolution of $\Delta v/v = 0.06$. The zero of the timescale is

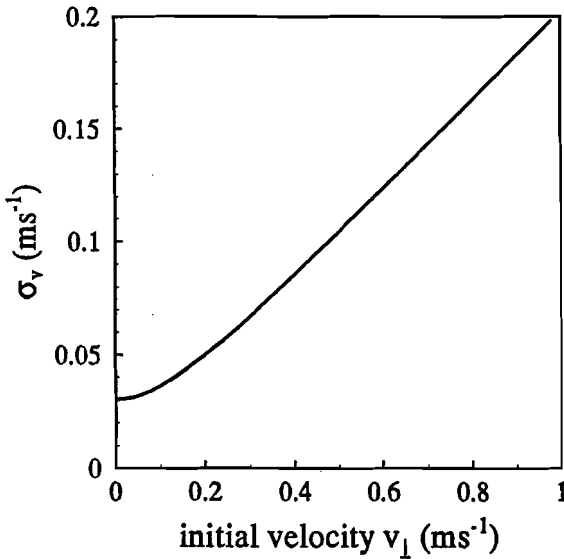


Figure 3.5: The initial transverse velocity spread as a function of the initial velocity. At $v_{\perp} = 0$, the spread is only due to the limited collimation of the beam. For large v_{\perp} , it is determined by the longitudinal velocity spread.

carefully calibrated by analyzing the position of the UV-light from the discharge in the time-of-flight spectrum. The time-of-flight measurements greatly simplify the analysis of the deflected beam profiles, avoiding a convolution over both the interaction time and the longitudinal atomic momentum.

All measurements were fully automated using the Phydas/EPEP laboratory automation system, a local standard of the physics department. This system also continuously checks experimental parameters like laser power, laser frequency, chopper frequency and source inlet pressure. A time-of-flight measurement with these extremely well-collimated atomic beams has a typical average atom count rate of 1 kHz. In order to reduce statistical errors a total atom count of about 10^4 is required both for 'laser on' and 'laser off' signals. This resulted in a measuring time of about 20 seconds per position of the detector slit, and thus a total measuring time of about 20 minutes per initial velocity.

3.4.2 Laser equipment

In figure 3.6 part of the level scheme of neon is shown. Neon in the ground state has the electron configuration $\{(1s)^2(2s)^2(2p)^6\}$. When we excite a $(2p)$ core electron to a $(3s)$ orbital we obtain the four fine structure states of the $\{(1s)^2(2s)^2(2p)^5(3s)\}$ configuration. The states 3P_0 and 3P_2 (Russell-Saunders notation) are metastable and have a radiative lifetime of at least several seconds [22]. The states $\{\alpha_1\}$ to $\{\alpha_{10}\}$ (Paschen numbering) form the $\{(1s)^2(2s)^2(2p)^5(3p)\}$ fine structure multiplet. All these states are short-lived, with a radiative lifetime $\tau \approx 20$ ns. For our experiment we used the transition from the metastable 3P_2 to the $\{\alpha_9\}$ ($\tau = 19.4$ ns) state, since this constitutes a pure closed-level system with only magnetic degeneracy. The natural linewidth of this transition is $\Gamma/2\pi = 8.2$ MHz. The wavelength of the laser light resonant with the two-level transition (640.225 nm) is easily produced by commercial

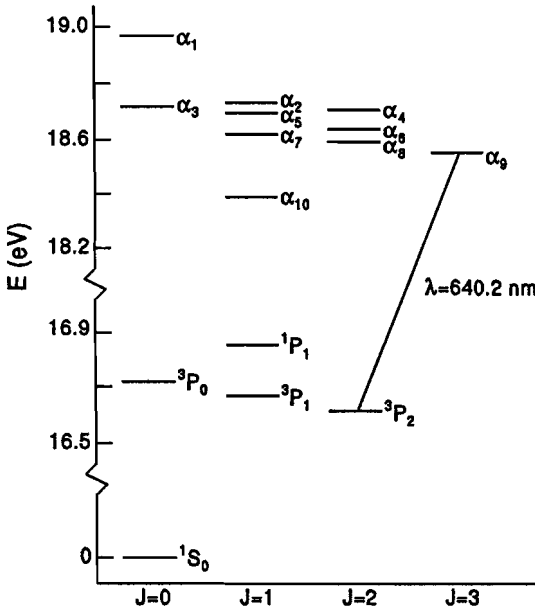


Figure 3.6: Part of the level scheme of neon. The lifetime of the metastable $3P_0$ and $3P_2$ states has been calculated to be 430 s and 24.4 s respectively [22]. For the cooling process we use the closed-level transition from the $\{3s\}3P_2$ state to the $\{3p\}3D_3 = \{\alpha_9\}$ state at 640.225 nm.

dye lasers, operating on DCM dye [23].

In our experiment we use a small frame Coherent Innova 70 Argon Ion pump laser and an actively stabilized Spectra-Physics 380D ring dye laser. The linewidth of the laser is ~ 250 kHz, which is small compared to the natural linewidth of the excited state of the atom. Long-term drift is prevented by locking the laser frequency to a Zeeman-modulated and -shifted saturated absorption gas discharge cell.

Transportation of the laser beam to both the saturated absorption setup and to the actual experiment is done by a single mode, polarization preserving fiber (York HB600). The polarization can be preserved to better than 1 : 100 over 30 meters of fiber when the optical axis of the fiber is properly aligned to the laser polarization, while the throughput can be as high as 70%. Using fibers has several advantages: one is that the building vibrations do not disturb the position and direction of the laser beam in the experiment. Another is that the alignment of the laser is decoupled from the alignment in the experiment. Coupling the laser beam into and out of these fibers is done with home-built, high stability fiber couplers using standard (25X) microscope objectives.

At the experiment, large-aperture cylindrical and AR-coated lenses are used in the telescope, minimizing aberrations and cut-off diffraction due to their finite size. The laser beam has a Gaussian waist on the backreflecting mirror with a radius of 0.56 mm ($1/e^2$ intensity drop) in the atomic beam direction, and 2.5 mm in the other dimension. Correct focussing of the laser beam is checked by autocollimation techniques. The wavefront curvature in the interaction region is less than 25 μ rad over the interaction region. Thus the additional variation of the angle between the laser field the atomic beam and hence variation of the atomic velocity in the direction of the laser due to wavefront curvature is negligible. The 0.5 mm high atomic beam is homogeneously

illuminated to within 2%. By using an AR-coated vacuum window and quarter wave plate ($R < 0.005$) and a high-reflection backreflecting mirror ($R > 0.995$) the intensity imbalance between the laser beams is kept smaller than 2%.

The laser beam is aligned perpendicular to the collimated atomic beam by tuning the laser resonant to the pumping transition to the $\{\alpha_8\}$ state, that can cascade to the ground state. The pumping efficiency at low laser power is then optimized by measuring the metastable signal loss. In the case of non-perfect alignment, the Doppler effect will decrease the interaction strength and thus the pumping efficiency. This ensures the laser beam to be perpendicular to the atomic beam to within 1 mrad. The optional quarter wave plates are placed just before and just after the interaction center, thus avoiding polarizing effects of other optical components.

The laser beam profile in the interaction region is measured carefully using a photodiode with a 0.1 mm diameter aperture. The profile is fitted to a Gaussian profile, that is used as input for the theoretical calculations. As a check for the laser intensity and detuning, we used the deflection of the atomic beam by one laser beam, and compare this to the results of a Monte-Carlo simulation of atomic beam deflection. This simulation is based on the simulation described in reference [21], but modified to include the variation of the light intensity when the atom traverses the Gaussian laser beam profile. The modification required replacing the analytical integrated photon waiting-time distribution with a direct numerical integration of the differential equations for the expansion coefficients of the wavefunction.

The magnetic field in the interaction region is controlled by a full set of Helmholtz coils. The magnetic field was zeroed by using the Hanle effect on the pumping transition to the $\{\alpha_8\}$ state. Since this is a $J_e = J_g$ transition, the transition from $m_g = 0$ to $m_e = 0$ is forbidden. Consequently, when the laser is linearly polarized, inducing $\Delta m = 0$ transitions, the atoms in the $m_g = 0$ ground state will not be depleted. This results in a decrease in the pumping efficiency. However, if there is a small magnetic field, the magnetic sublevels will be mixed up by Larmor precession, and eventually the atoms initially in the $m = 0$ sublevel will also be depleted. This means that the pumping efficiency and thus the loss of signal will have a minimum when the magnetic field components perpendicular to the laser polarization are zero. This proved to be a very sensitive test on the magnetic field with a residual magnetic field $B < 5$ mGauss. The Larmor frequency is thus much smaller than the reciprocal of the interaction time.

3.4.3 Data analysis

To measure a deflected beam profile, a time-of-flight spectrum is taken at each detector position. The measured counts in one particular time-of-flight channel at different detector positions form a beam profile for a mono-energetic atomic beam. Such a profile for 1200 ms^{-1} atoms in the $\pi^x\pi^y$ polarization configuration is shown in figure 3.7. The signal with ‘laser on’ is denoted by circles, the signal with ‘laser off’ by squares. The undeflected peak in the ‘laser on’ profile is due to ^{20}Ne atoms in the 3P_0 metastable state and ^{22}Ne atoms in both metastable states, which are not deflected. Together, these represent 25.0% of the total signal, which is consistent with the natural abundance of the neon isotopes and the statistical ratio of 5:1 between the 3P_2 and 3P_0 metastable state populations. This ratio has proven to be very stable. The deflected beam profile

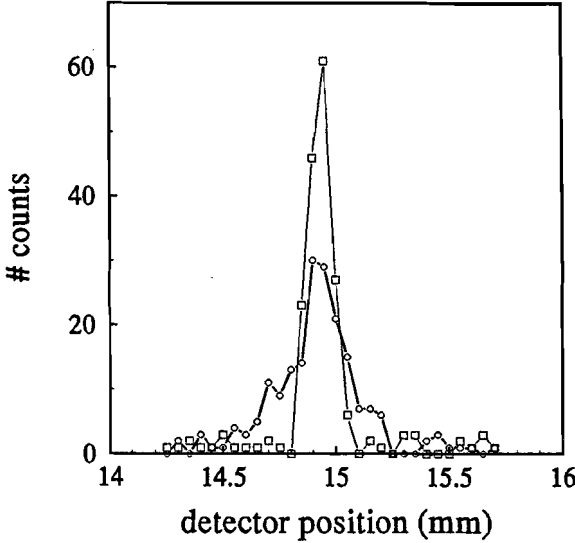


Figure 3.7: A typical deflected beam profile in for the $\pi^x\pi^y$ polarization configuration. In squares, the initial beam profile is shown, and in circles the deflected beam profile, both for the 1200 ms^{-1} time-of-flight channel. The initial velocity in the direction of the laser is 0.1 ms^{-1} in this figure. The laser detuning in this figure is -2Γ , and the saturation parameter $s = 4.0$.

is obtained by subtracting 25.0% of the ‘laser off’ signal from the ‘laser on’ signal. The initial velocity is $v_{\perp} = 0.10 \text{ ms}^{-1}$ in this figure. We can observe both a broadening and a deflection of the atomic beam. Using the time-of-flight analysis this can unambiguously be related to a velocity change Δv and the spread σ_v therein.

In order to reduce the statistical errors due to the low count rate, all time-of-flight channels are processed simultaneously in the following manner. To account for the different interaction times, the velocity transfer profiles for the different time-of-flight channels are transformed to acceleration profiles by dividing by the effective interaction time:

$$a_{\perp} = \frac{\Delta v_{\perp}(v_{\text{ax}})}{\tau_{\text{eff}}(v_{\text{ax}})} = \frac{\Delta v_{\perp}(v_{\text{ax}})v_{\text{ax}}}{l_{\text{eff}}} \quad (3.18)$$

The effective interaction time $\tau_{\text{eff}}(v_{\text{ax}})$ is defined as the time an atom with axial velocity v_{ax} needs to traverse a laser beam with an ‘equivalent square profile’. This is defined as the square profile with the same integrated area and variance as the Gaussian laser beam profile, i.e., a profile with width $l_{\text{eff}} = \sigma\sqrt{12}$ and height $I_{\text{eff}} = (\pi/6)^{\frac{1}{2}}I_0$ for a Gaussian with variance σ^2 and maximum height I_0 . The thus obtained array of acceleration profiles is fitted simultaneously to the sum of two Gaussians for the shape and to the supersonic velocity distribution for the normalization of each time-of-flight channel using a least-squares procedure. The two-Gaussian fit function was found to yield a satisfactory fit to the experimental data in all cases and hence yields reliable values for the deflection and the broadening of the atomic beam. This way, the statistical errors are greatly reduced while only introducing a spread in v_{\perp} discussed in section 3.4.1.

In figure 3.8 fitted ‘acceleration’ profiles for four different polarization configurations are displayed for an initial velocity $v_{\perp} = 0$. In the $\sigma^+\sigma^-$ polarization configuration, an almost Gaussian broadening of the atomic beam due to momentum diffusion is observed. For the $\pi^x\pi^x$ and the $\sigma^+\sigma^+$ configuration, effects of channeling in the standing

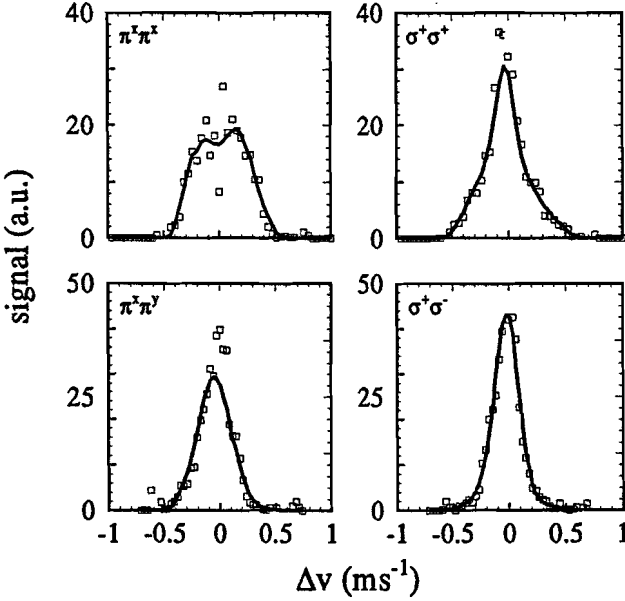


Figure 3.8: Deflected beam profiles averaged over the time-of-flight spectrum for the $\pi^x\pi^x$ (upper left) $\sigma^+\sigma^+$ (lower left), $\pi^x\pi^y$ (upper right) and $\sigma^+\sigma^-$ polarization configurations. Here, the horizontal axis is velocity change. The two-Gaussian fit curve is represented by the full line.

wave are clearly visible through the broad base of the deflection curve. For the $\pi^x\pi^y$ configuration this is less clear. The effects of channeling will be discussed in detail in section 3.5.2.

3.5 Results and discussion

3.5.1 The $\sigma^+\sigma^-$ polarization configuration

In this polarization configuration the force on the atom does not depend on the initial position of the atom in the quasi-standing wave. Therefore fit parameters can directly be related to an average force and a diffusion coefficient. In figure 3.9 the force in the $\sigma^+\sigma^-$ polarization configuration laser detunings of equal magnitude but reversed sign are plotted as a function of the initial velocity. Also the results from the quantum Monte-Carlo (QMC) simulations, indicated by the full lines, and the semiclassical (SC) calculations, indicated by the dotted lines, as discussed in section 3.3.1 and 3.2.2 respectively are shown. The force is scaled to the maximum radiation pressure force $\hbar k\Gamma/2 = 2.710^{-20}$ N. Clearly visible is the dispersion-like shape of the force. The force is obviously larger than the Doppler force, indicated by the dashed line, but much smaller than the steady-state drag force, as indicated by the dash-dotted line. This

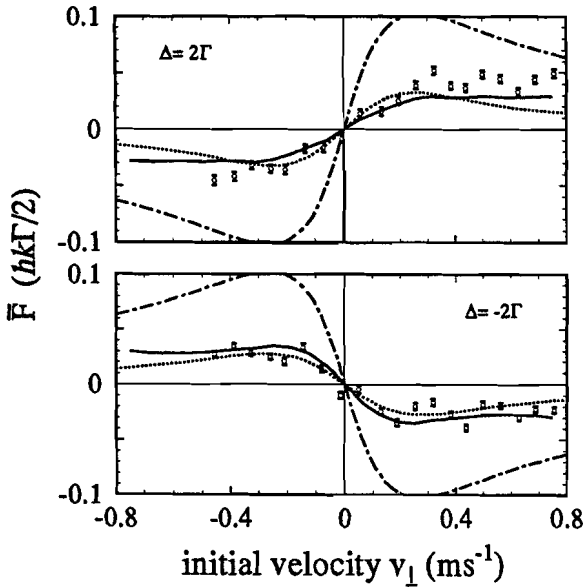


Figure 3.9: The force as a function of the initial velocity v_{\perp} for the $\sigma^+\sigma^-$ configuration. The laser detuning is $\Delta = 2\Gamma$ for the upper graph and $\Delta = -2\Gamma$ for the lower graph. The saturation parameter for both curves is $s = 3.6$. The dash-dotted line indicates the steady-state drag force for these parameters. The results of the QMC and SC calculations are represented by the full and dotted lines respectively.

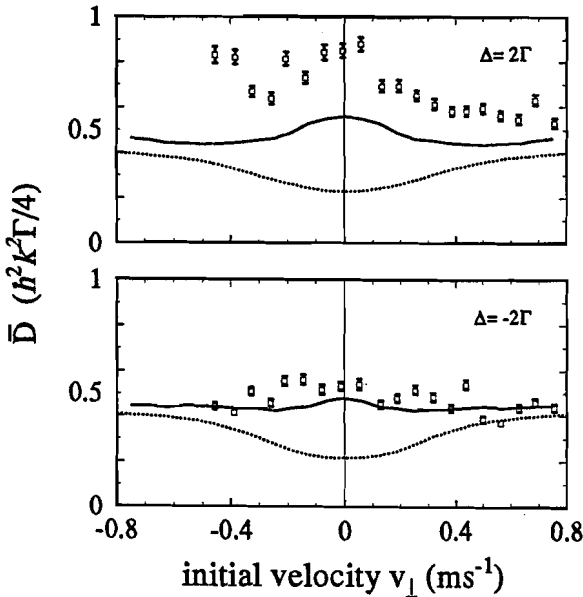


Figure 3.10: The diffusion constant as a function of the initial velocity v_{\perp} for the $\sigma^+\sigma^-$ configuration. The laser detuning is $\Delta = 2\Gamma$ for the upper graph and $\Delta = -2\Gamma$ for the lower graph. The saturation parameter for both curves is $s = 3.6$.

is caused by a transient effect: following the argument in section 3.2.1 the Larmor frequency induced by the topological magnetic field is smaller than the reciprocal of the interaction time. Notwithstanding, this represents the first direct measurement of a sub-Doppler cooling force on neutral atoms. We observe that the force reverses as expected when the sign of the detuning is changed. The small difference between the SC and the QMC model is mainly caused by the fact that the SC calculations do not include the Doppler force.

In figure 3.10 the diffusion coefficients are plotted as a function of the initial velocity for these measurements. The diffusion coefficient is scaled by $\hbar^2 k^2 \Gamma / 4 = 1.410^{-47} \text{kg}^2 \text{m}^{-2} \text{s}^{-3}$. Again, both theoretical calculations are displayed as well, showing good agreement. Note the differences between the results of the SC and QMC calculations near $v_{\perp} = 0$. The decrease in diffusion coefficient predicted by the SC model does not show up in either the experiments or the QMC calculations. We therefore consider this an artefact of the semiclassical calculation. It originates from considering the whole ensemble of atoms to follow a single ‘averaged trajectory’. The diffusion is calculated as the time autocorrelation of the force along this trajectory. When the force strongly depends on the velocity, this procedure is incorrect. The base level of the diffusion at large v_{\perp} is well reproduced. The differences between the experimental and theoretical curves in the positive detuning curves are probably caused by the systematic error in the experimental determination of the laser detuning as discussed in section 3.4. The agreement can be largely improved by adjusting the detuning in the theoretical calculations. However, for clarity the experimentally determined values are used as input for the calculations. In contrast to the SC calculations, the QMC calculations predict a small increase in the diffusion coefficient around $v_{\perp} = 0$. This increase is too small to be visible in the experiment. So far, we have found no physical interpretation of this effect.

In figure 3.11 the force as a function of the initial velocity is shown for three different laser intensities at the same laser detuning, as well as the results from both the QMC simulations and the SC calculations. The agreement of both models with the experiment is excellent. Again the differences between the models are caused by the omission of the Doppler force in the SC model. Note that the calculations are carried out without any free parameters. The calculated curves show that the maximum sub-Doppler cooling force increases quadratically with the laser intensity. This can be understood by the following argument: the steady state cooling force increases linearly and the transient effect is reduced with increasing laser intensity.

For the diffusion coefficient, as displayed in figure 3.12 again a large difference between the SC model and both the experimental data and the QMC curves is observed due to the effect discussed earlier. The agreement of the QMC calculations with the measurements is excellent, whereas the large decrease in the diffusion coefficient near $v_{\perp} = 0$ in the SC calculations for high laser intensity is not reproduced by either the QMC calculations or the experimental data.

The oscillation visible in all plots of the experimental force as a function of the initial velocity is not reproduced by either theoretical model. In the experiment, however, it is reproducible and has a period of approximately 0.2ms^{-1} . So far, these oscillations have not been explained and might be either an experimental artefact or an unknown physical effect.

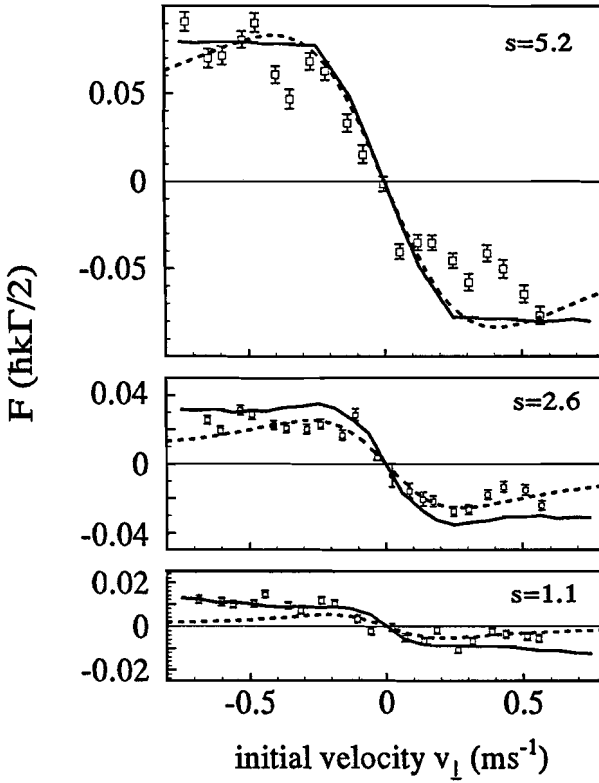


Figure 3.11: The force as a function of initial velocity v_{\perp} for three laser intensities in the $\sigma^+\sigma^-$ configuration. Also the SC (dotted line) and QMC (full line) calculations are shown. In all curves the detuning $\Delta = -1.6\Gamma$.

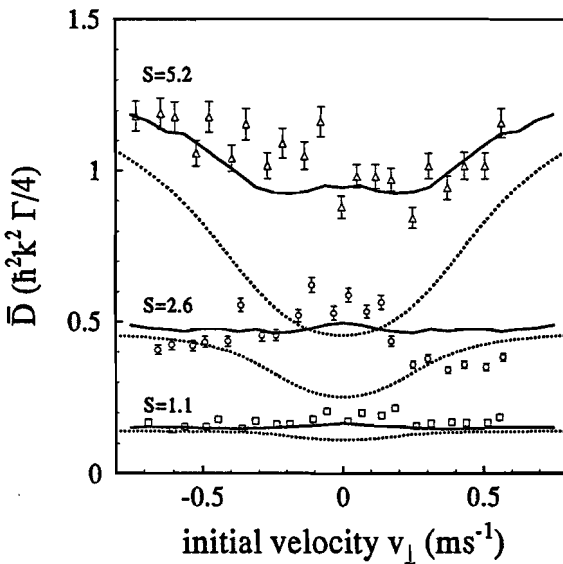


Figure 3.12: The diffusion constant as a function of initial velocity v_{\perp} for three laser intensities in the $\sigma^+\sigma^-$ configuration. Also the SC (dotted line) and QMC (full line) calculations are shown. In all curves the detuning $\Delta = -1.6\Gamma$.

3.5.2 Channeling in a standing wave

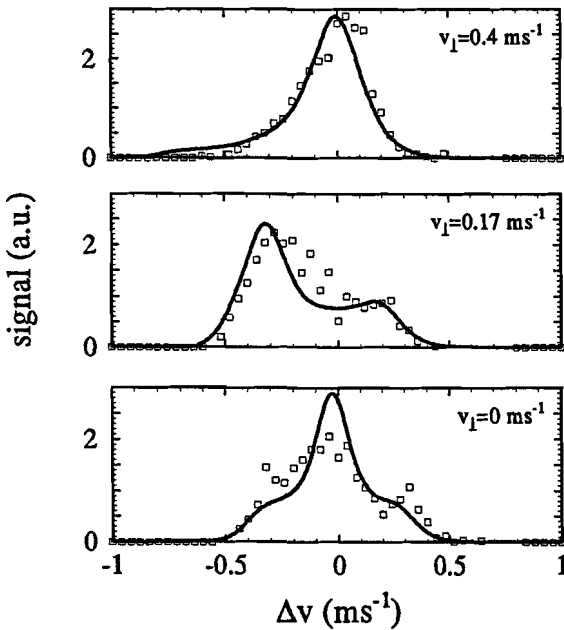


Figure 3.13: Deflected beam profiles for the initial velocity $v_{\perp} > v_c$ (upper part), $v_{\perp} < v_c$ (middle part) and for $v_{\perp} = 0$ (lower part) in the $\pi^x\pi^x$ polarization configuration. The laser detuning $\Delta = -2.0\Gamma$ and the saturation parameter $s = 4.1$ for all graphs, resulting in $v_c = 0.21 \text{ ms}^{-1}$. The full line represents the results of the QMC calculations.

In a purely standing wave of either linear or circularly polarized light the atoms can be deflected by the periodic potential formed by the differing light shift in the nodes and the antinodes of the field. In this configuration, there should be no real cooling force present due to the lack of polarization gradients. In figure 3.13 a deflected beam profile in a pure standing wave of linearly polarized light is shown for an initial velocity $v_{\perp} = 0 \text{ ms}^{-1}$, 0.17 ms^{-1} and 0.40 ms^{-1} . At $v_{\perp} = 0.17 \text{ ms}^{-1}$, a structure with two maxima can clearly be observed. The results from the QMC calculations are plotted as well. We now introduce the capture velocity v_c , which is defined as the velocity for which kinetic energy of the atoms is equal to the height of such a potential hill. For the situation of figure 3.13 $v_c = 0.21 \text{ ms}^{-1}$. If $v_{\perp} > v_c$, as for $v_{\perp} = 0.40 \text{ ms}^{-1}$, the atomic beam will only be deflected by the Doppler force and is just broadened by spontaneous emission.

This threshold behavior is clearly visible in figure 3.14. Here, in the lower part the average final velocity is shown as a function of the initial velocity. In the upper part, the spread in final velocity σ_v is plotted. When the initial velocity is below v_c ($v_c \approx 0.4 \text{ ms}^{-1}$), we observe that the atomic beam is strongly broadened and that the average final velocity is almost zero. An actual slight reversal of the initial velocity can be observed, indicating that atoms perform less than a full oscillation in the potential well on their transit through the laser beam. The full line indicates the results from the QMC simulations, indicating good agreement with the experiment.

In figure 3.15 the average velocity change Δv as a function of v_{\perp} for equal magnitude but reversed laser detunings Δ at the same laser intensity are shown. We clearly see that the velocity change does not depend on the detuning. Just the small offsets in the

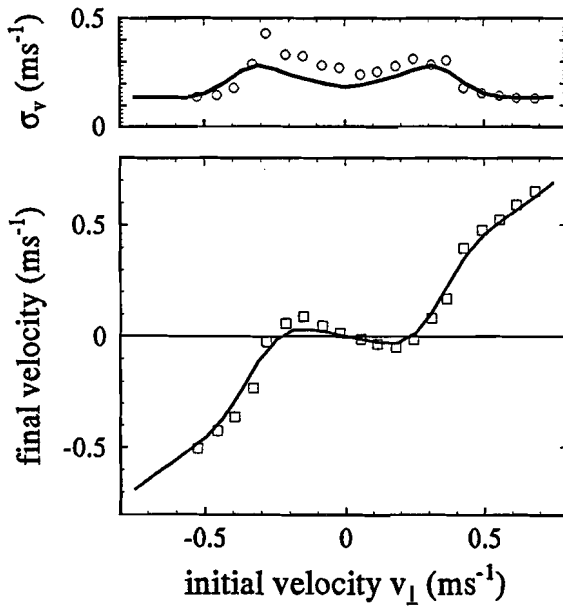


Figure 3.14: The final velocity (lower part) and the spread in final velocity (upper part) as a function of the initial velocity in a linearly polarized standing wave. The detuning $\Delta = -0.8\Gamma$ and the saturation parameter $s = 4.1$. The results from the QMC (full line) and RE simulations (dotted line) for these parameters show excellent agreement.

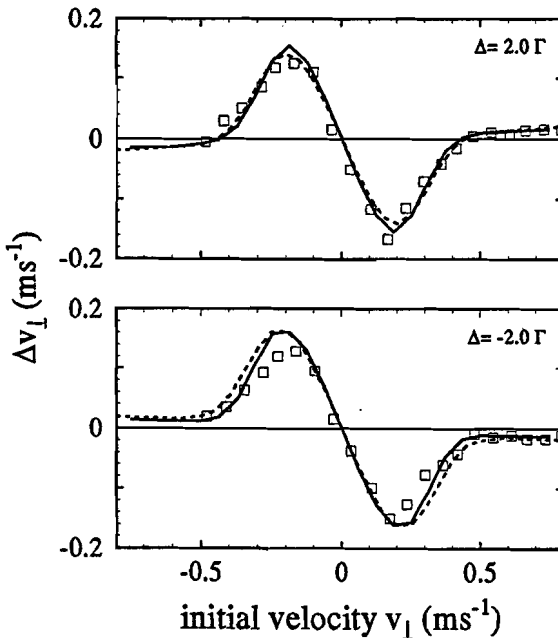


Figure 3.15: The average velocity change Δv as a function of initial velocity v_{\perp} in a linearly polarized standing wave for equal but reversed detunings. The detuning $\Delta = \pm 2\Gamma$ and the saturation parameter $s = 4.2$ for both profiles. The results from the QMC and RE calculations are represented by the full and dotted lines respectively.

tails of the profiles indicate residual effects of Doppler cooling. The agreement with the QMC simulations, indicated by the full lines, is excellent. The agreement with the results from the simple rate-equation based model (RE) as indicated by the dashed lines is excellent as well. Consequently the physical channeling picture is correct to a high degree.

It should be stressed that although the average velocity is reduced to zero in this configuration, it is *not* a cooling process. The final velocity of the atoms just depends more strongly on the position at which they enter the standing wave than on the initial velocity. This can be experimentally observed as a strongly enhanced broadening of the atomic beam, as shown in figure 3.16. In this figure we plot σ_v as a function of

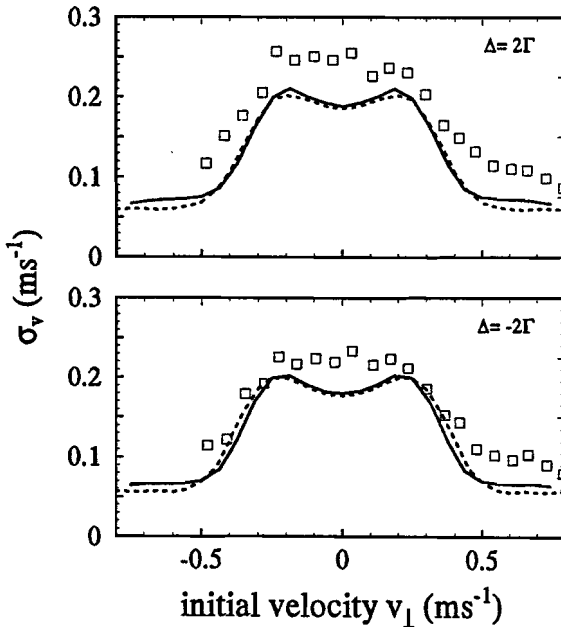


Figure 3.16: The spread in final velocity σ_v as a function of initial velocity v_{\perp} in a linearly polarized standing wave for equal but reversed detunings. The detuning $\Delta = \pm 2\Gamma$ and the saturation parameter $s = 4.2$ for both profiles. The results from the QMC and RE calculations are represented by the full and dotted lines respectively.

v_{\perp} for the measurements in figure 3.15. The strong broadening for small v_{\perp} does not depend on the laser detuning, as would be the case for a cooling process. With an even better resolution of the final velocity, diffraction effects could possibly be observed in the deflected beam profiles.

For a pure standing wave of circular polarization the same physical picture holds. In figure 3.17 the deflected beam profiles are shown for an initial kinetic energy either larger or smaller than the light shift, and for zero initial velocity. Also the results from the QMC simulations (full line) are shown. The agreement is not as good as in the case of linear polarization, but still quite satisfactory. At zero initial velocity, we observe a rather sharp peak at $\Delta v = 0$ and a broader underlying structure. For $v_{\perp} < v_c$ the underlying structure has shifted and has a long tail under the undeflected peak. For $v_{\perp} > v_c$, we only observe one peak, that is only slightly broadened by spontaneous emission. In this situation, the experimental velocity transfer profile is broader than the theoretically calculated profile. The small peak at $\Delta v = 0$ in the first two situations caused by the atoms that are initially in the $m = -2$ sublevel. Due to

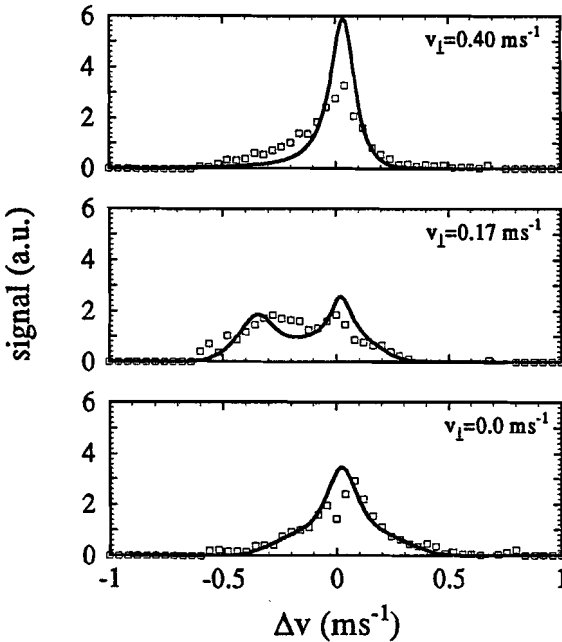


Figure 3.17: Deflected beam profiles for the initial velocity $v_{\perp} > v_c$ (upper part), $v_{\perp} < v_c$ (middle part) and for $v = 0$ (lower part) in the $\sigma^+\sigma^+$ polarization configuration. The laser detuning $\Delta = -2.0\Gamma$ and the saturation parameter $s = 3.6$ for all graphs. The full line represents the results of the QMC calculations.

the small Clebsch-Gordan coefficient, these atoms have an appreciable probability of not being excited at all by the laser beams. Hence these atoms will hardly be deflected.

In figure 3.18 the average velocity change Δv as a function of initial velocity v_{\perp} is shown for reversed but equal magnitude laser detunings. Again in this situation there is no sub-Doppler cooling force. The Doppler cooling force is very small and is visible in the small offset in the tails of the profiles. In figure 3.19 the broadening of the beam σ_v is shown as a function of initial velocity v_{\perp} . The agreement with the results of the QMC simulation, indicated by the full lines, is quite good for both the deflection and the broadening of the beam. The differences are probably due to an error in the experimental values of the laser detuning as discussed in section 3.4.2.

If a magnetic field is applied perpendicular to the propagation direction of the laser light, the well-known magnetically induced laser cooling (MILC) force [24, 10] should be visible. The effects of this force are, however, largely obscured by the deflection caused by channeling. For a higher magnetic field, velocity selective magnetic resonance laser cooling (VSMRLC) [25, 10] should be visible. In figure 3.20 the velocity change and broadening in pure standing wave of σ polarized light in a magnetic field perpendicular to the laser field $B = 0.753$ Gauss is shown. Near zero initial velocity the channeling effect is dominant, but at higher initial velocity some extra features are observed. The resonant velocity for VSMRLC is 0.50 ms^{-1} . The QMC simulation again excellently reproduces the results from the experiments.

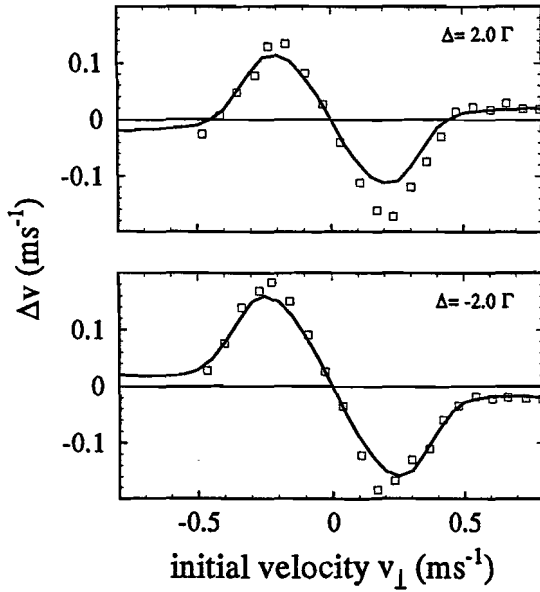


Figure 3.18: The average velocity change Δv as a function of initial velocity v_{\perp} for a circularly polarized standing wave for equal but reversed detunings. The detuning $\Delta = \pm 2\Gamma$ and the saturation parameter $s = 3.5$ for both profiles. The results from the QMC calculations are indicated by the full lines.

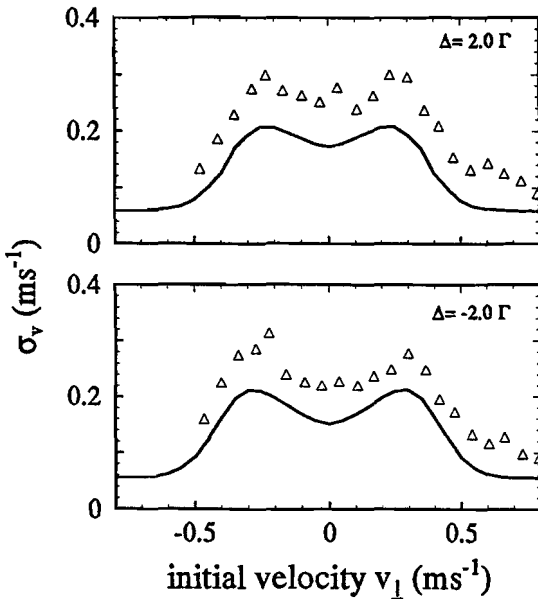


Figure 3.19: The spread in final velocity σ^v as a function of initial velocity v_{\perp} for a circularly polarized standing wave for equal but reversed detunings. The detuning $\Delta = \pm 2\Gamma$ and the saturation parameter $s = 3.5$ for both profiles. The results from the QMC calculations are indicated by the full lines.

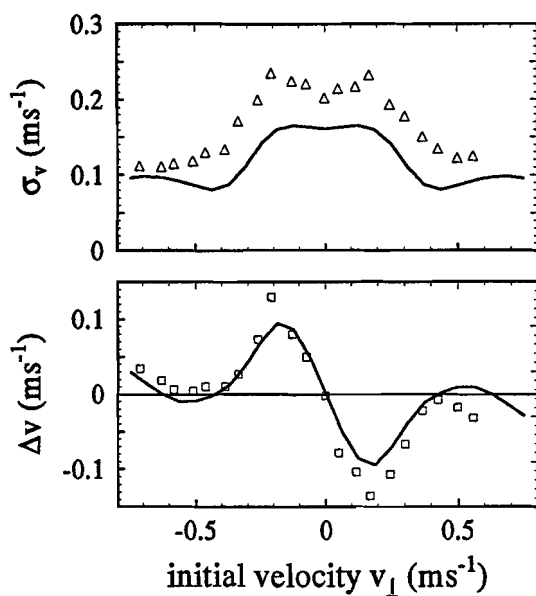


Figure 3.20: *The average velocity change Δv (lower part) and the final velocity spread σ_v (upper part) for a circularly polarized standing wave with a magnetic field perpendicular to the direction of the laser beam. The detuning $\Delta = -1.6\Gamma$, the saturation parameter $s = 2.6$ and the magnetic field $B = 0.753$ Gauss for these curves. The results from the QMC simulations are represented by the full line, showing good agreement.*

3.5.3 The $\pi^x\pi^y$ polarization configuration

In the $\pi^x\pi^y$ configuration (usually called lin \perp lin) the atoms can, depending on their initial magnetic substate, be channeled in the potential wells formed by the polarization gradient. Again we expect a largely different behavior for atoms entering the laser field at different positions or in a different magnetical substate. Consequently, the broadening of the atomic beam is also expected to be non-Gaussian. In this case, there is a large difference between positive and negative detuning due to the actual cooling process. The atoms are always optically pumped to the most light-shifted substate. For positive detuning this means that the atoms are always pumped to the highest potential hill, which is not a stable situation. For negative detuning, the reverse is true and the atoms will accumulate in potential valleys.

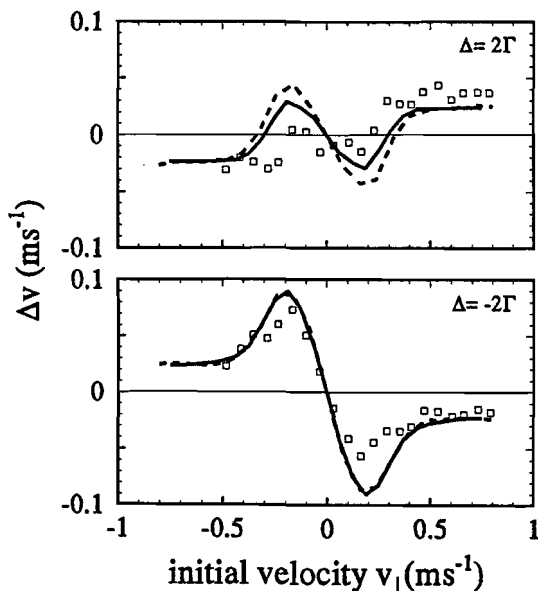


Figure 3.21: The average velocity change Δv as a function of initial velocity v_{\perp} in the $\pi^x\pi^y$ polarization configuration for equal but reversed detunings. The detuning $\Delta = \pm 2\Gamma$ and the saturation parameter $s = 4.0$ for both profiles. The results from the QMC and RE calculations are represented by the full and dotted lines respectively.

In figure 3.21 the average velocity change Δv of the atomic beam in this configuration for positive and negative detuning are shown. Notice that the average effects of cooling and channeling almost cancel for positive detuning, whereas for negative detuning the effects add up. In both figures, also the results from the QMC (full line) and RE (dashed line) calculations are displayed. The excellent agreement between the QMC and RE simulations indicate that the physical picture associated with the $\pi^x\pi^y$ cooling mechanism is correct to a high degree. In figure 3.22 the spread in final velocity σ_v is displayed for these situations. In these curves the large difference between positive (upper part) and negative (lower part) detuning is clearly visible. In the latter case the channeling effect is enhanced by the optical pumping to the magnetic substate that is lowest in energy. This enhanced channeling effect causes a stronger broadening for v_{\perp} smaller than the threshold. In the former case, the channeling is decreased by the optical pumping. Note the excellent agreement of the experimental data with the results from both the QMC simulation (full line) and RE simulation (dashed line).

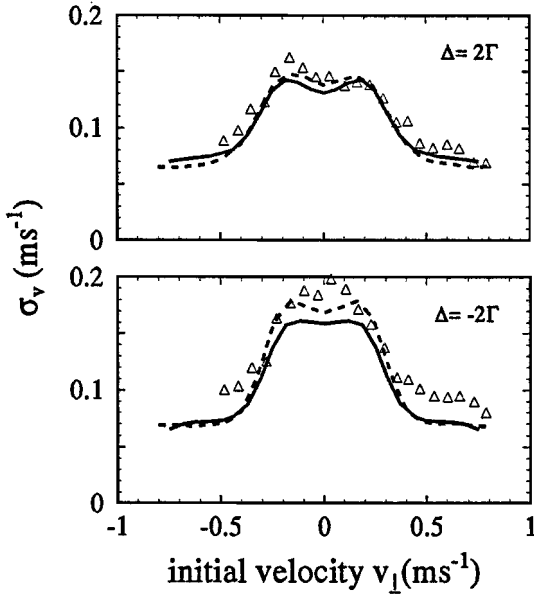


Figure 3.22: The final velocity spread σ_v as a function of initial velocity v_{\perp} in the $\pi^x\pi^y$ polarization configuration for equal but reversed detunings. The detuning $\Delta = \pm 2\Gamma$ and the saturation parameter $s = 4.0$ for both profiles. The results from the QMC and RE calculations are represented by the full and dotted lines respectively.

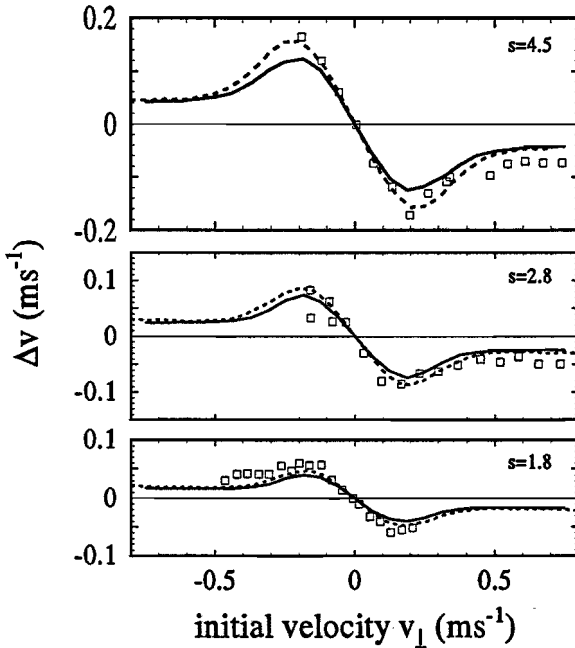


Figure 3.23: The average velocity change Δv as a function of initial velocity in the $\pi^x\pi^y$ polarization configuration for three different values of the laser intensities $s = I/I_0$. The detuning $\Delta = -1.6\Gamma$ for all profiles. The results from the QMC and RE simulations are represented by the full and dashed lines respectively.

In figure 3.23 the velocity change Δv is given for three different intensities at the same laser detuning. We can observe that both the maximum velocity change due to the channeling mechanism and the capture velocity v_c of this mechanism increases with increasing intensity as expected. The results from the QMC and RE simulations are shown, indicated by the full and dashed lines respectively. The agreement of the experimental data and both simulations is good. The final velocity spread σ_v for these situations is shown in figure 3.24. Herein the increase in capture range can be observed

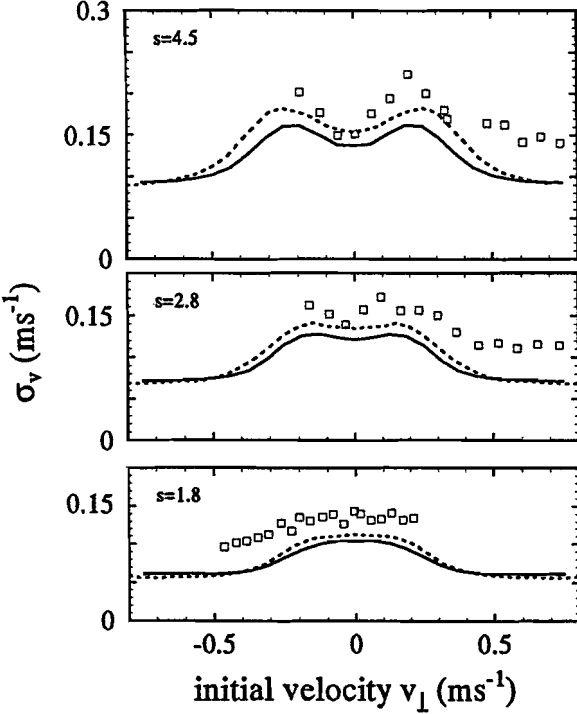


Figure 3.24: The velocity spread σ_v as a function of initial velocity in the $\pi^x\pi^y$ polarization configuration for three different values of the laser intensities $s = I/I_0$. The detuning $\Delta = -1.6\Gamma$ for all profiles. The results from the QMC and RE simulations are represented by the full and dashed lines respectively.

as well: for initial velocities larger than the capture range the beam is only broadened by spontaneous emission, while for smaller initial velocity the final velocity depends on the initial position of the atom in the spatially modulated potential. Note that for $s = 4.5$, the spread in deflection near $v_{\perp} = 0$ is smaller than for larger v_{\perp} .

In figure 3.25 the velocity change Δv is shown for two different detunings at the same laser intensity, as well as the result from both the QMC and RE simulations. The channeling effect decreases with increasing detuning as expected. In the final velocity spread, as displayed in figure 3.26, we observe a large difference between these situations. For large detuning (upper part), the broadening due to channeling is dominant and causes the broadening to be large. For smaller detuning (lower part) the optical pumping rate is much larger and the Sysiphus mechanism is relatively important. This is visible as a large decrease in broadening for small v_{\perp} . The agreement of both simulations with the experimental data is good for both situations.

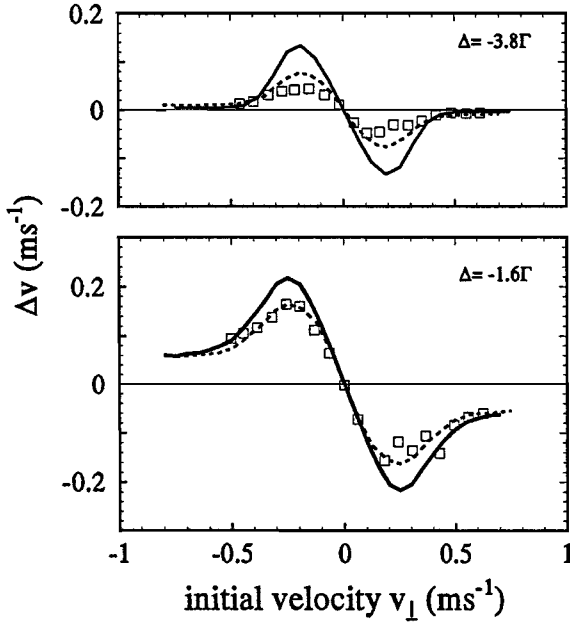


Figure 3.25: The average velocity change Δv as a function of initial velocity $\pi^x \pi^y$ in the polarization configuration for two different values of the laser detuning Δ . The saturation parameter $s = I/I_0 = 6.1$ for both profiles. The results from the QMC and RE simulations are represented by the full and dashed lines respectively.

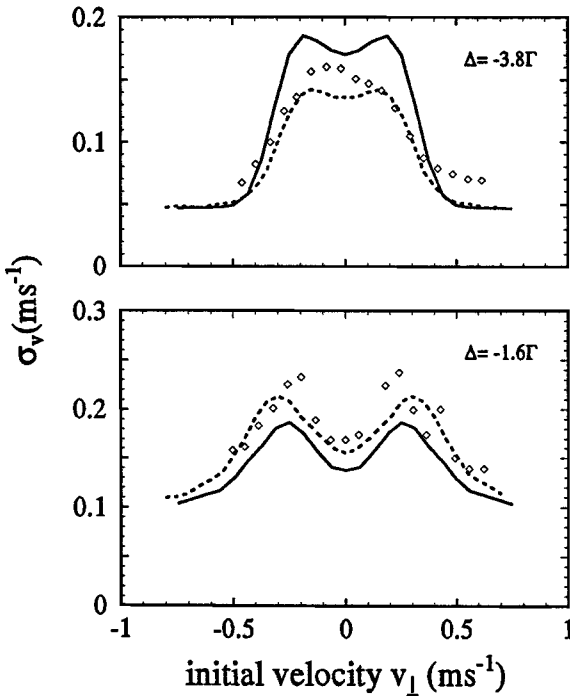


Figure 3.26: The velocity spread σ_v as a function of initial velocity $\pi^x \pi^y$ in the polarization configuration for two different values of the laser detuning Δ . The saturation parameter $s = I/I_0 = 6.1$ for both profiles. The results from the QMC and RE simulations are represented by the full and dashed lines respectively.

3.6 Conclusions

We have presented the first direct measurements of the velocity dependence of $\sigma^+\sigma^-$ sub-Doppler laser cooling forces and diffusion constants for neon atoms. We compared the experimental results to a simulation based on a quantum Monte-Carlo approach as well as a semiclassical density matrix calculation. We demonstrate excellent quantitative agreement with the experimental data without any free parameters.

The effects of channeling in the periodic potential induced by a standing laser wave of either circular or linear polarization have been demonstrated. These results show excellent agreement with simulations based on a simple rate-equation approach, as well as with the more rigorous quantum-Monte-Carlo calculations.

Experimental results obtained for the $\pi^x\pi^y$ cooling configuration are perfectly reproduced by the rate-equation-based calculations as well. This demonstrates that the simple physical 'Sisyphus' picture for the cooling mechanism is valid to a high degree.

The dynamics of the cooling process for both $\sigma^+\sigma^-$ and $\pi^x\pi^y$ configurations have been studied in great detail as a function of laser detuning and intensity. The experimental and theoretical data provide a good insight in the dynamics of the cooling process.

For future extensions, we intend to investigate the transition to the steady state by varying the interaction time and keeping the laser intensity constant during the interaction. As we go from a single oscillation in a potential well to a large number, quantization of the atomic motion will become visible. In fact, we will be able to excite selectively one particular vibrational state in the potential well. For other transitions, we can selectively excite a 'dark' state. Other extensions include sub-Doppler cooling forces and dark states in two-dimensional laser fields, which have not at all been investigated.

Acknowledgements

This work is financially supported by the Dutch Foundation for Fundamental Research on Matter (FOM) (Hoogerland), the Royal Dutch Academy of Sciences (KNAW) (Van der Straten), the National Science Foundation (NSF) (Vredenburg, Metcalf) and the Office for Naval Research (ONR) (Vredenburg, Metcalf).

References

- [1] T.W. Hänsch and A.L. Schawlow. *Opt. Comm.* **13**, 68(1975).
- [2] D.J. Wineland and H. Dehmelt. *Bull. Am. Phys. Soc.* **20**, 637(1975).
- [3] A. Aspect, J. Dalibard, A. Heidmann, C. Salomon, and C. Cohen-Tannoudji. *Phys. Rev. Lett.* **41**, 1361(1987).
- [4] P.E. Moskowitz, P.L. Gould, and D.E. Pritchard. *J. Opt. Soc. Am.* **B2**, 1784(1985).
- [5] J. Mlynek. private communication.

- [6] M.D. Hoogerland, H.J.L. Megens, M.P. Schuwer, J.P.J. Driessen, H.C.W. Beijerinck, and K.A.H. van Leeuwen. this thesis, chapter 4.
- [7] P.S. Julienne and F.H. Mies. *J. Opt. Soc. Am.* **B6**, 2257(1989).
- [8] C. Salomon, J. Dalibard, W. D. Phillips, A. Clarion, and S. Guellati. *Europhys. Lett.* **12** 683(1990).
- [9] P.D. Lett, W.D. Phillips, S.L. Rolston, R. N. Watts C.E. Tanner, and C.I. Westbrook. *J. Opt. Soc. Am.* **B6**, 2084(1989).
- [10] M.D. Hoogerland, H.C.W. Beijerinck, K.A.H. van Leeuwen, P. van der Straten, and H.J. Metcalf. *Europhys. Lett.* **19**, 669(1992).
- [11] J. Dalibard and C. Cohen-Tannoudji. *J. Opt. Soc. Am.* **B6**, 2023(1989).
- [12] P.J. Ungar, D.S. Weiss, E.Riis, and S. Chu. *J. Opt. Soc. Am.* **B6**, 2058(1989).
- [13] G. Nienhuis, P. van der Straten, and S-Q. Shang. *Phys. Rev.* **A44**, 462(1991).
- [14] R. Dum, P. Zoller, and H. Ritsch. *Phys. Rev.* **A45**, 4879(1992).
- [15] J. Dalibard, Y. Castin, and K. Mølmer. *Phys. Rev. Lett.* **68**, 580(1992).
- [16] C. Salomon, J. Dalibard, A. Aspect, H. Metcalf, and C. Cohen-Tannoudji. *Phys. Rev. Lett.* **59**, 1659(1987).
- [17] P. Verkerk, B. Lounis, C. Salomon, C. Cohen-Tannoudji, J.-Y. Courtois, and G. Grynberg. *Phys. Rev. Lett.* **68**, 3861(1992).
- [18] R. Blatt, W. Ertmer, P. Zoller, and J.L. Hall. *Phys. Rev.* **A34**, 3022(1986).
- [19] B.R. Mollow. *Phys. Rev.* **A12**, 1919(1975).
- [20] M.D. Hoogerland, M.N.H. Wijnands, H.J. Senhorst, H.C.W. Beijerinck, and K.A.H. van Leeuwen. *Phys. Rev. Lett.* **65**, 1559(1990).
- [21] M.D. Hoogerland, H.C.W. Beijerinck, and K.A.H. van Leeuwen. this thesis, chapter 2.
- [22] N.E. Small-Warren and L.Y. Chin. *Phys. Rev.* **A11**, 1777(1975).
- [23] 4-dicyanomethylene-2-methyl-6(*p*-dimethyl-amino-styryl)-4H-pyran.
- [24] B. Sheehy, S-Q. Shang, P. van der Straten, and H.J. Metcalf. *Phys. Rev. Lett.* **64**, 858(1990).
- [25] S-Q. Shang, B. Sheehy, P. van der Straten, and H.J. Metcalf. *Phys. Rev. Lett.* **65**, 317(1990).

Chapter 4

A 1600-fold increase in beam intensity for neutral atoms using laser cooling forces

M.D. Hoogerland, M.P. Schuwer, H.J.L. Megens,
J.P.J. Driessen, H.C.W. Beijerinck and K.A.H. van Leeuwen

*Eindhoven University of Technology,
P. O. Box 513 5600 MB Eindhoven, the Netherlands.*

Abstract

The design of an 'atomic beam intensifier' for neutral atoms using a combination of laser cooling techniques is presented. A beam of $\text{Ne}^* \text{}^3\text{P}_2$ atoms, initially diverging at 0.1 rad half-angle, is first collimated by a variation of the Doppler cooling-technique using effectively curved wavefronts. It is then focussed by a magneto-optical lens and recollimated near the focus by Doppler cooling. This results in a beam with a diameter of 4 mm and a divergence of 0.002 rad, containing the full flux of the original beam. This constitutes an increase in centerline beam intensity with a factor 1600. The intensified atomic beam opens up a whole new range of possible applications.

4.1 Introduction

The concept that neutral atoms can be cooled to very low temperatures using (almost) resonant laser radiation pressure was first proposed by Wineland and Dehmelt [1] and Hänsch and Schawlow [2] in 1975. With the first experimental results in 1985 [3], laser cooling has experienced a rapidly increasing interest over the last decade. Many applications of laser cooling in various other fields are being proposed. One area is ultra-high resolution spectroscopy, where cold atoms can be used for atomic frequency standards [4] and for atomic interferometers[5]. Other possibilities for application lie, e.g., in the study of extremely cold collisions. Laser manipulation allows not only 'real' cooling in three dimensions, but also one- and two-dimensional cooling as well as non-cooling effects like deflection and focussing of atomic beams. Thus, 'optical' elements for neutral atomic beams have been developed [5]. Unlike in traditional optics, due to the dissipative nature of laser cooling the phase space volume of an atomic beam can be reduced. Thus, the control offered of the motion of free atoms is virtually complete, opening the way to even more applications.

In collision physics, very intense and well-collimated atomic beams are required to accurately study, e.g., atomic collision processes with small cross-sections or collisions between excited state atoms. For instance, to study binary collisions of metastable rare gas atoms, e.g., the process $\text{Ne}^* + \text{Ne}^* \rightarrow \text{Ne} + \text{Ne}^+ + e^-$, the beam flux as offered by conventional atomic beams is fully insufficient. In this work a scheme is implemented, where two-dimensional laser cooling and focussing of an atomic beam is used to produce a very intense, well-collimated atomic beam.

Radiation pressure arises when a two-level atom is placed in a resonant laser field. The atom absorbs a photon from the laser beam, and thereby the photon momentum in the direction of the laser beam, and re-emits the photon spontaneously in a random direction. Over many of these events, the latter contribution averages out to zero, whereas the former adds up to a force: the radiation force $F = \hbar k \Gamma n_e$. The force is proportional to the spontaneous emission rate Γn_u , with n_e the excited state population and Γ the decay rate of the upper level, and to the photon momentum $\hbar k$, with $|k| = 2\pi/\lambda$ the wavenumber of the photon. The upper state population is for resonant excitation given by $n_u = s/(2(s+1))$, with the on-resonance saturation parameter $s = I/I_0$, which is proportional to the laser intensity. The reference intensity I_0 is a characteristic of the atomic transition. The maximum force $F = \hbar k \Gamma / 2$ yields an acceleration of the order of 10^5 ms^{-2} for a light atom like neon with a strong transition. For non-resonant excitation, the Lorentz-profile of the transition has to be taken into account. The expression for the radiation pressure force on an atom from a single laser beam then takes the form:

$$F = \frac{\hbar k \Gamma}{2} \frac{s}{(1 + s + (2\Delta/\Gamma)^2)} \quad (4.1)$$

with Δ the detuning. For a moving atom, the effective detuning is not only determined by the laser frequency, but also includes a contribution $\Delta_D = -\mathbf{k} \cdot \mathbf{v}$ due to the Doppler effect. The Doppler effect thus makes the force strongly dependent on the atomic velocity in the direction of the laser.

The velocity-dependence of the radiation pressure force forms the basis for the 'standard' laser cooling effect known as 'Doppler cooling' or 'optical molasses' [6].

Atoms are placed in a standing wave of slightly red-detuned laser light. An atom moving slowly in the direction of the laser beams will see the counterpropagating beam slightly blue-shifted by the Doppler effect, and consequently closer to resonance. The atom will absorb more photons from the counterpropagating laser beam than from the copropagating and experiences a stronger radiation pressure force from the counterpropagating beam. The resulting force as a function of the atomic velocity for a typical example of a cooling transition and for the optimal laser detuning $\Delta = -\Gamma/2$ is shown in figure 4.1. For small velocities ($v < 5 \text{ ms}^{-1}$), the decelerating force is proportional to the velocity, and thus constitutes a pure friction force. The atomic motion is damped and the atoms are cooled. If three orthogonal pairs of laser beams are used, a so-called trap configuration, three-dimensional cooling results [7]. In two dimensions, an atomic beam can be collimated this way.

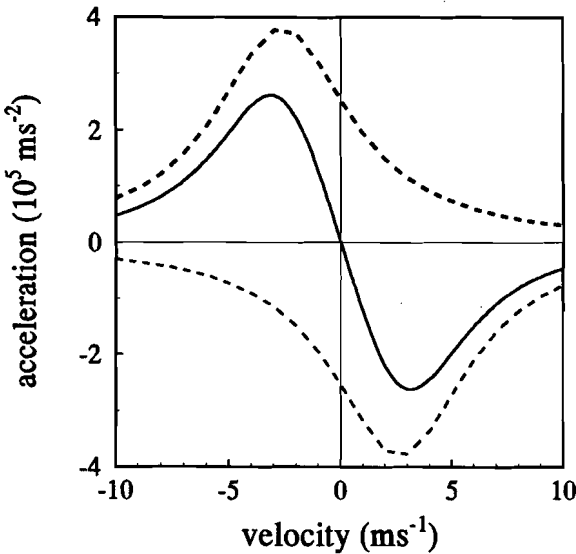


Figure 4.1: The acceleration of neon atoms due to the radiation pressure force in a standing laser wave as a function of the atomic velocity for optimal conditions $\Delta = -\Gamma/2$. The contributions to the total force of the two laser beams are represented by the dashed lines respectively. The total force is represented by the full line, showing a linear increase with the velocity for small velocity. The saturation parameter $s = I/I_0 = 1$ for both laser beams.

In a magnetic field, the atomic energy levels are shifted by an amount $\Delta E = \hbar \mu_B B m g_j$, with B the magnetic field, g_j the Landé factor, μ_B the Bohr magneton and m the magnetic quantum number for the quantization axis of the field. Thus $\mu_B m$ is the magnetic moment of the atom in the direction of the magnetic field. Therefore an additional detuning $\Delta_{\text{mag}} = \mu_B B (g_j m_e - g_j m_g) / \hbar$ can be introduced. Using an inhomogeneous magnetic field, the resulting force on an atom can also be made position dependent. This results in the possibility of making, e.g., lenses for neutral atoms. A combination of velocity- and position dependent forces is used to obtain efficient trapping and cooling of atoms in a so-called Magneto-Optical Trap (MOT) [8]. In a two-dimensional version, efficient two-dimensional compression of a slow atomic beam can be obtained [9].

The velocity- and position selective forces described above provides us with a powerful means to manipulate atoms. We use these forces for a three-stage 'atomic beam brightener'. The basic idea of such a three-stage beam intensifier was proposed by Metcalf [10], and is shown in figure 4.2. First, two-dimensional laser cooling is used to

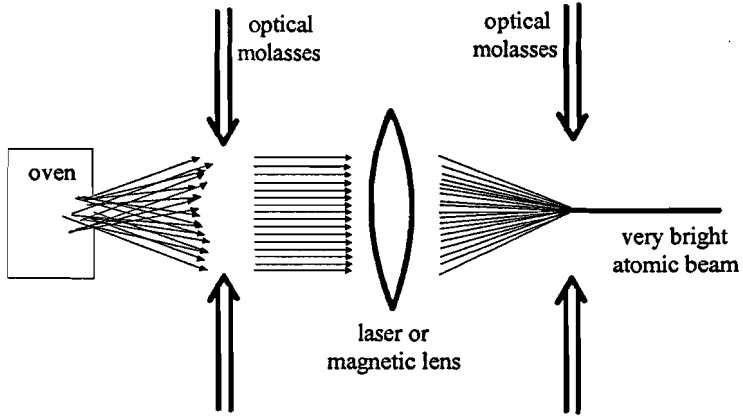


Figure 4.2: The principle of an atomic beam brightener according to the initial proposal by Metcalf. An initially diverging atomic beam is collimated using a laser cooling techniques. Then it is focussed, and near the focus it is recollimated.

wavelength	λ	640.225 nm
wavevector	$k = 2\pi/\lambda$	$9.8 \cdot 10^6$
nat. lifetime	τ	19.4 ns
nat. linewidth	$\Gamma = 1/\tau$	$5.15 \cdot 10^7 \text{ s}^{-1}$
mass	M	20 a.m.u.
recoil velocity	$v_{rec} = \hbar k/M$	0.031 ms^{-1}
sat. intensity	I_0	$40.8 \mu \text{ W mm}^{-2}$

Table 4.1: Some important cooling parameters for Neon

collimate the atomic beam. A lens for neutral atoms focusses the beam, and near the focus the beam is recollimated to a high-flux, small diameter atomic beam.

In this paper, we implement this scheme to intensify a beam of metastable $\{3s\}^3P_2$ neon atoms. The atoms are excited on the 640.225 nm transition to the $\{3p\}^3D_3$ state, which is a closed-level transition, of which some parameters are displayed in table 4.1. The total amount of laser power used is 200 mW. We achieve an intensity increase in a collimated atomic beam with a factor of 1600. Due to a modular design, the scheme can easily be adapted to a variety of other elements, such as other metastable rare gases or alkali metal atoms. This makes the setup enormously flexible for use in, e.g., atomic collision or spectroscopy experiments.

A functional overview of the set-up is shown in figure 4.3. The discharge-excited source (1) is cooled with liquid nitrogen. This reduces the atomic velocity with a factor of two, which greatly simplifies the laser cooling process as the interaction length needed for all laser cooling stages scales with the kinetic energy of the atoms, i.e., the source temperature. It is discussed in detail in section 4.3.1. The collimating section (2) uses velocity selective excitation to create a parallel, large diameter (~ 20 mm)

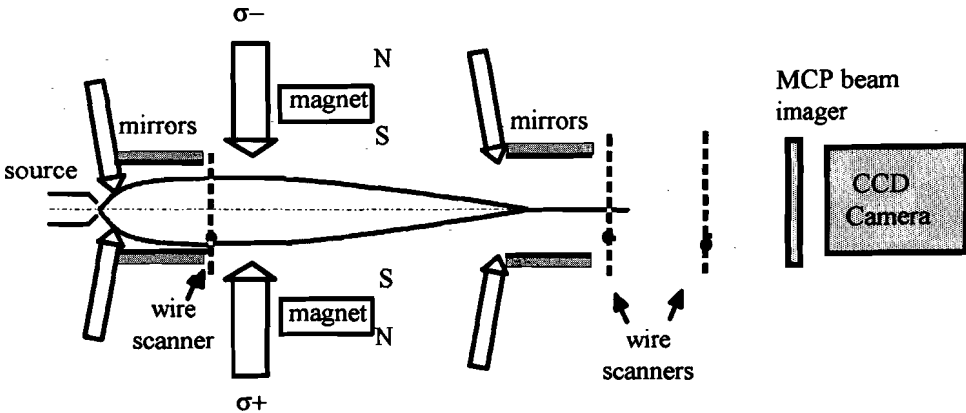


Figure 4.3: A schematic overview of the set-up. The liquid nitrogen cooled thermal source produces a diverging atomic beam. The beam is collimated using the curved-wavefronts technique discussed in section 4.2.1. It is focussed using a magneto-optical lens, as discussed in section 4.2.2. Near the focus the beam is recollimated again using curved wavefronts. The atomic beam profile can be measured at several positions using the wire scanners, as discussed in section 4.3.5.

atomic beam. A variation of the Doppler cooling scheme is used to achieve a large capture range. We use the position-dependent Zeeman effect in an inhomogeneous (quadrupole) magnetic field to create a magneto-optical lens (3) for neutral atoms. The lens focusses the beam to a spot with a diameter of ~ 3 mm. Another collimating section (4) serves to collimate the converging beam near the focus of the lens, yielding a small diameter intensified atomic beam. Some design considerations for all cooling stages are given in section 4.2. The design of the components, which is based on the results of a Monte-Carlo simulation of the cooling process (see section 4.2), is discussed in section 4.3. In section 4.4 the operation of the setup is demonstrated, showing a 1600-fold increase in collimated atomic beam intensity.

4.2 Theory of operation

4.2.1 Collimating sections

As discussed before, using the Doppler effect a velocity selective, cooling force can be exerted on an expanding atomic beam. Thus, the beam can be collimated using a transverse standing laser field. To transversely decelerate atoms with an initial transverse velocity v_{\perp} , using half the maximum resonant radiation pressure $F = F_{\max}/2 = \hbar k \Gamma/4$, an interaction time $t_{\text{int}} = (M v_{\perp})/F$ is required. For a beam with an axial velocity v_{\parallel} and an initial half angle divergence θ , this translates to an interaction length of

$$L = v_{\parallel} t_{\text{int}} = \frac{\theta M v_{\parallel}^2}{\hbar k \Gamma/4} \quad (4.2)$$

proportional to the kinetic energy of the atoms. For neon atoms at an axial velocity of 600 ms^{-1} and a divergence $\theta = 100 \text{ mrad}$, this is an interaction length $L = 93 \text{ mm}$. The atomic beam after collimation has a radius $r = \frac{1}{2}(F/M)t_{\text{int}}^2 = 5 \text{ mm}$.

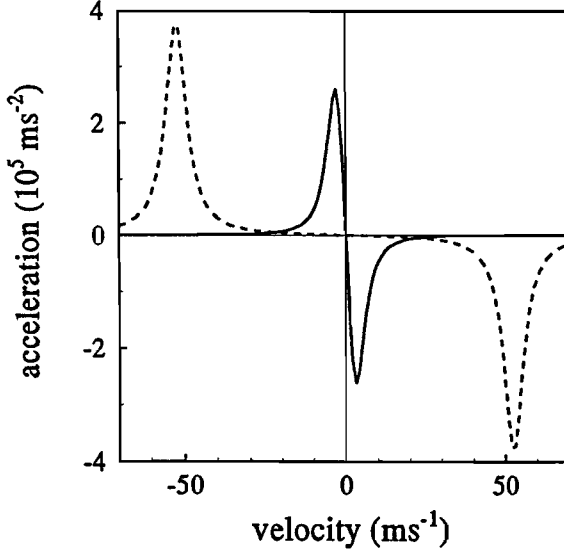


Figure 4.4: The acceleration for neon atoms as a function of velocity for $\Delta = -8\Gamma$ (indicated by the dashed line) yields a much larger capture range of the cooling process. To achieve effective collimation to $v_{\perp} = 0$, the detuning has to be chirped to $\Delta = -\Gamma/2$ (full line) during the interaction time.

However, the capture range of the radiation pressure force is limited to typically $v_{\perp} = \pm 5 \text{ ms}^{-1}$ for neon, as indicated by the dashed line in figure 4.4. The capture range can be extended by increasing the detuning, as shown by the full line in the figure. In this situation however, atoms with an initial velocity of $v_{\perp} = 50 \text{ ms}^{-1}$ experience a strong force only until their Doppler shift has changed with more than a natural linewidth, at $v_{\perp} = 40 \text{ ms}^{-1}$. For cooling to $v_{\perp} = 0$, this is very inefficient.

Consequently, to cool atoms from a large transverse velocity to $v_{\perp} = 0$ it is necessary to chirp the laser detuning while the atom is decelerated. As the laser frequency is chirped, the atoms with the largest v_{\perp} immediately start to be decelerated while atoms with a smaller v_{\perp} get into resonance at a later point. This technique is often used for longitudinally slowing an atomic beam. Its main disadvantage is that a pulsed beam is obtained: only a small fraction of the initial beam ends up in the cooled beam. A more practical way of achieving a varying laser detuning in transverse cooling of an atomic beam is by using curved laser wavefronts. We illuminate the atomic beam at an angle that is changed as the atom moves downstream through the interaction region as illustrated in figure 4.5. The Doppler shift can be written as

$$\Delta_D = -\mathbf{k} \cdot \mathbf{v} = -kv_{\parallel} \sin \beta + kv_{\perp} \cos \beta \approx -k\beta v_{\parallel} + kv_{\perp} \quad (4.3)$$

with v_{\parallel} the axial velocity of the beam. We now define an effective detuning $\Delta_{\text{eff}} = \Delta - kv_{\parallel} \beta$. As β changes as the atom moves downstream through the interaction region, the effective detuning changes as well. Thus the force can be kept at maximum through the interaction region, and the cooling process is consequently very efficient. This directly translates into an interaction time (in a beam experiment: interaction length) that can be kept as short as possible. As the effective detuning is ‘chirped’ in

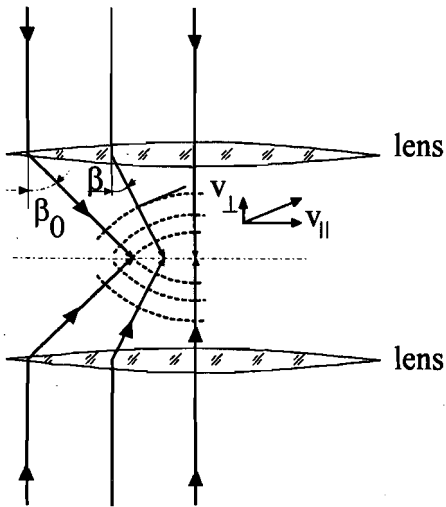


Figure 4.5: Using curved wavefronts, we can change the angle β between the atomic beam and the laser beam as the atoms move downstream. This way, the laser effective laser frequency is chirped in space.

space and not in time, a continuous beam is obtained. However, the interaction length is still considerable, typically 100 mm for cooling neon atoms with an axial velocity of $v_{\parallel} = 600 \text{ ms}^{-1}$ and an initial transverse velocity $v_{\perp} = 60 \text{ ms}^{-1}$. Hence using a large, converging laser beam to obtain the desired wavefront curvature requires a large amount of laser power to fill the interaction region. For a two-dimensional setup this would require four beams with a power of approximately 100 mW each, a prohibitive amount for a single component of the beam brightener. Other methods of increasing the capture range, e.g., using broadband radiation [11], require even more laser power.

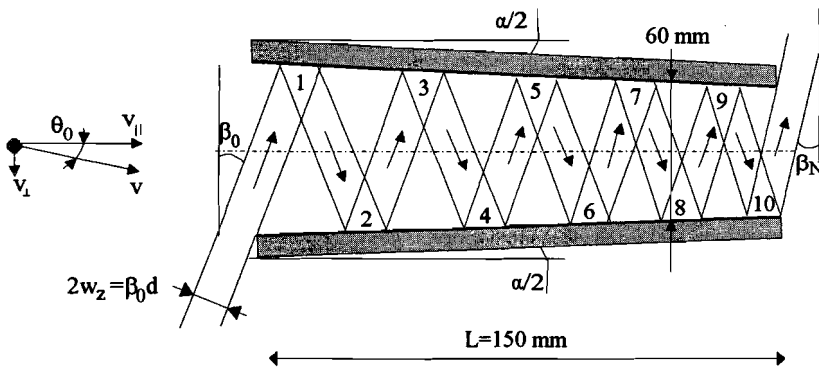


Figure 4.6: Schematic representation of the collimating section. A small diameter laser beam is coupled between the mirrors with an incidence angle β_0 . With each reflection, the angle between the atomic beam and the intersecting laser beam is reduced with an amount α .

To obtain effectively curved wavefronts, we use a set of two almost-parallel mirrors, with the laser light coupled in at one and of the mirrors at an angle β_0 to the atomic

beam, as shown in figure 4.6. With each reflection, the angle with the atomic beam is reduced: after n reflections it is $\beta_n = \beta_0 - n\alpha$, with α the angle between the mirrors. To achieve the ideal linear chirp, β should decrease linearly with the axial position. However, the actual situation is more complicated. After β_0/α reflections, the resulting angle $\beta = 0$ and the laser beam turns back. As the laser beam heats for $\beta < 0$, this would decrease the efficiency of the collimation. If β is small and the number of reflections between the mirrors is large, β can be approximated as

$$\beta(z) = \sqrt{2\alpha \frac{z_{\max} - z}{d}} \quad (4.4)$$

with

$$z_{\max} \approx d \frac{\beta_0^2}{2\alpha} \quad (4.5)$$

the axial position at which laser beam would turn back. To avoid the beam from turning back, and to achieve an approximately linear dependence of Δ_{eff} on z , z_{\max} should be larger than the mirror length. In figure 4.7 the effective detuning as a function of position is shown for the actual working parameters. The effective detuning is changed from $\Delta_{\text{eff}} = -8\Gamma$ to $\Delta_{\text{eff}} = -\Gamma/2$ as the atom moves downstream. This way, the capture range is increased dramatically while the final transverse velocity spread is kept minimal. However, it is also clear that the cooling mechanism depends rather strongly on the axial velocity v_{\parallel} . This means that it is preferable to use a supersonic beam with a small velocity spread, and a small final angle β_N to minimize the influence of a spread in v_{\parallel} . As the difference between β_0 and β_N is fixed by the required chirp in Δ_{eff} , β_0 then also has to be chosen small. The waist radius w of the incoming laser beam has to be larger for larger β_0 , thus requiring more laser power. On the other hand, the angles cannot be arbitrarily small, as $\beta(z)$ varies too steeply near $z = z_{\max}$. Coupling the laser beams between the mirrors at small β_0 becomes increasingly difficult as well.

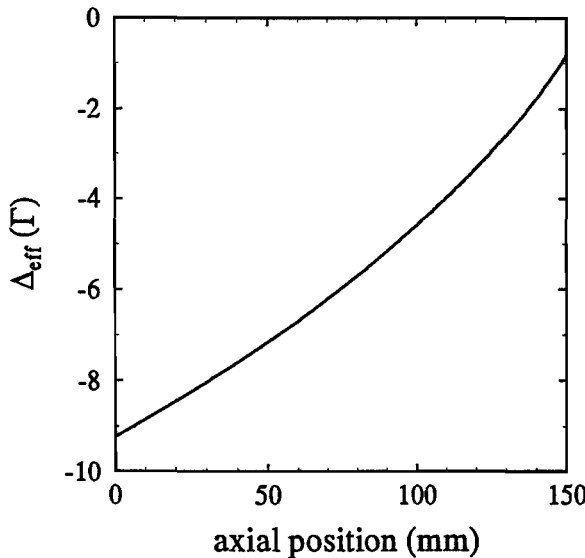


Figure 4.7: The effective laser detuning as a function of the axial position in the first collimating section. The effective detuning is almost linearly reduced from $\Delta_{\text{eff}} = -8\Gamma$ at the beginning of the mirrors to $\Delta_{\text{eff}} = -\Gamma$ at the end.

As a compromise, the entry angle is chosen to be ~ 100 mrad. The laser detuning in this section $\Delta = +35$ MHz, which corresponds to a capture velocity of 60 ms^{-1} . This scheme can easily be implemented in two dimensions, enabling a two-dimensional collimation of the atomic beam.

In order to optimize the design of the collimating sections, we perform a Monte-Carlo simulation. The program calculates the classical trajectories of an atom with a given initial velocity when illuminated with (quasi-)resonant light from several laser beams. Initially, the atoms are assigned a random magnetical sublevel of the 3P_2 metastable state. For each laser beam crossing the atomic beam at a given position the saturation parameter is given by $s_i = I_i/I_0$. The saturation intensity depends on the magnetic substate as well as on the laser polarization through the (squared) Clebsch-Gordan coefficients. For each laser beam, an 'effective saturation parameter' is defined as:

$$s_i^{\text{eff}} = \frac{s_i}{1 + (2(\Delta_{\text{eff}} + kv_{\perp})/\Gamma)^2} \quad (4.6)$$

The photon scattering rate R_i for each beam can be calculated, with all cross saturation terms taken into account, as

$$R_i = \frac{\Gamma}{2} \frac{s_i^{\text{eff}}}{1 + \sum_j s_j^{\text{eff}}} \quad (4.7)$$

The photon scattering rate R_i is directly translated to a force $\mathbf{F}_i = \hbar \mathbf{k}_i R_i$ in the direction of that laser beam. Spontaneous emission heating is introduced by adding random recoils to the motion of the atom at the total photon scattering $\sum_i R_i$ rate and optical pumping by allowing the atom to change ground-state sublevel after each scattering event.

In the simulation, the total force on an atom is equal to $\mathbf{F} = \sum_i \mathbf{F}_i$. The total number of laser beams seen by the atom is at least four. We integrate the motion of the atom using these forces and thus obtain a particle trajectory in both real and velocity space. In figure 4.8 such particle trajectories are displayed for atoms with several initial velocities in the first collimating section. In the upper part of the figure,

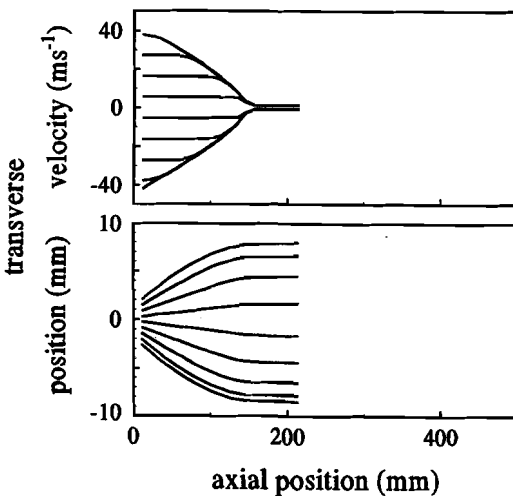


Figure 4.8: Simulated particle trajectories in the collimating section in velocity space (upper part) and real space. The transverse velocity of all atoms is reduced to zero during the interaction, yielding a parallel atomic beam.

one can clearly observe that the transverse velocity of the initially fastest atoms is decreased linearly as the atoms move through the 150 mm interaction region. The atoms with a smaller initial transverse velocity, come into resonance later and are also decelerated to $v_{\perp} = 0$. In the lower part, we observe that the atomic beam is collimated to a parallel beam with a diameter of ≈ 15 mm. This is a factor of three larger than the analytical estimate. This is due to the fact that in this estimate, the saturation parameter for the strongest subtransition is inserted. The actual saturation parameter, averaged over the subtransitions for linearly polarized light, is a factor of 2 lower.

4.2.2 Magneto-optical lens

After the first collimating section, we end up with a parallel, high flux atomic beam with a diameter of 18 mm. For most collision experiments, this is way too large. To decrease the beam width, we have to create a 'lens' for neutral atoms. Thus it is necessary to introduce a position sensitive, 'restoring' force. The for an ideal lens, the force F should be proportional to the distance to the axis. Such a force can be introduced in several ways.

One possibility is to use a hexapole magnetic lens, which focusses an atomic beam of polarized atoms [12]. As our parallel atomic beam is not polarized, this would only focus one fifth of all atoms.

Another way is to 'guide' the atoms towards the axis by introducing a position dependent AC-Stark shift. This can be implemented by using a high-power red-detuned laser beam counterpropagating to the atomic beam. This alternative however, would require a prohibitive amount of laser power.

We have chosen the alternative of using a position dependent light pressure force by exploiting the Zeeman effect in an inhomogeneous magnetic field. In a magnetic field the degeneracy of the magnetic sublevels is removed as shown in figure 4.9 for the $J = 2 \rightarrow J = 3$ neon transition. The energy shift ΔE of an atom in a magnetical

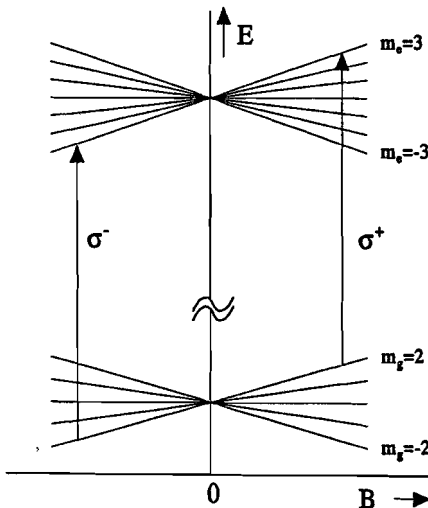


Figure 4.9: The removal of the degeneracy of the magnetic sublevels for the used $J = 2 \rightarrow J = 3$ transition in a magnetical field.

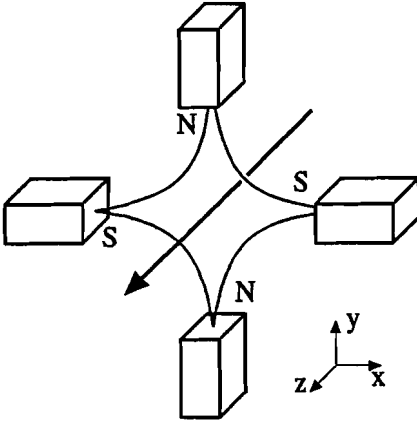


Figure 4.10: The magnetic field of a quadrupole. The magnetic field strength increases linearly with the distance from the axis.

sublevel m_j with respect to a magnetic field B is given by $\Delta E = \hbar \mu_B g_j m_j B$ with g_j the Landé factor and μ_B the Bohr magneton. When the atom with ground state g and excited state e is illuminated with either σ^+ , π , or σ^- polarized light with respect to the magnetic field, transitions with $\Delta m = +1, 0$ or -1 are induced. The transition frequency is then shifted by

$$\begin{aligned} \Delta_{\text{mag}} &= \mu_B B [g_{j_e}(m_g + \Delta m) - g_{j_g} m_g] / \hbar \\ &= \mu_B B [(g_{j_e} - g_{j_g}) m_g + g_{j_e} \Delta m] / \hbar \end{aligned} \quad (4.8)$$

A laser detuning in circularly polarized laser light can thus be compensated for by introducing a magnetic field in the direction of the k -vector of the light. Hence, when the magnetic field is inhomogeneous the radiation pressure force is position dependent.

In a quadrupole magnetic field as shown in figure 4.10, the magnetic field strength not too far from the axis of the quadrupole varies linearly with the radial distance and is zero on the axis. For simplicity, we first consider atoms on the x axis. The shift of the transition frequency Δ_{mag} is proportional to the magnetic field strength B and thus to x .

We now illuminate the atom with a laser field with σ^+ light running in the $+x$ direction and σ^- light running in the $-x$ direction. In a simplified picture we assume that in a weak magnetic field the frequency difference between the transitions with identical Δm to be small, which is true when $|g_{j_e} - g_{j_g}| \ll g_{j_e}$ (see equation 4.8). In figure 4.11 the simplified energy diagram is shown as a function of x . The laser frequency is detuned to the red of the resonance line by an amount Δ . At position x_1 , the laser detuning is exactly compensated for by Zeeman shift for the $\Delta m = +1$ transition. Consequently an atom at position x_1 will interact most strongly with the σ^+ light, which is running in the $+x$ direction and will thus experience a force towards the axis. The reverse is true for an atom at position $x_2 = -x_1$. We choose the magnetic field gradient to be $0.2 \text{ Gauss mm}^{-1}$, such that the outermost atoms in our collimated atomic beam are Zeeman-shifted by $-\Gamma/2$ and choose the laser detuning $\Delta = -\Gamma/2$. This way, the quadrupole magnetic field in combination with the circularly polarized laser light creates a radiation pressure force towards the atomic beam axis that is linear with the distance from the axis with coefficient ξ over the width of the collimated

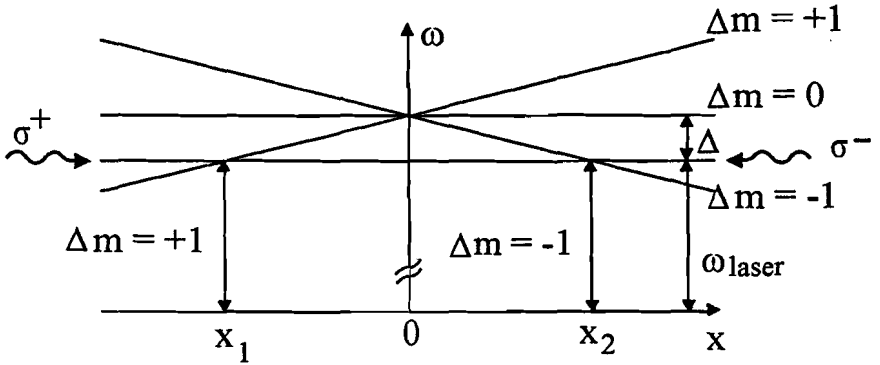


Figure 4.11: The Zeeman tuned transition frequencies as a function of x in a simplified picture. The σ^+ polarized laser beam from the right has a small red detuning, so it is most resonant with atoms at position x_1 . The σ^- polarized laser beam from the left is most resonant with atoms at position x_2 . All atoms are thus pushed towards $x = 0$.

beam, as shown in figure 4.12. With an interaction length L , the atoms gain a velocity $\Delta v_{\perp} = \xi x L / M v_{\parallel}$ towards the axis. Consequently the focal length $L_{\text{focus}} = x v_{\parallel} / \Delta v_{\perp}$ is again proportional to the kinetic energy of the atoms. In figure 4.12, $\xi = 610^{-19} \text{Nm}^{-1}$ and the achievable focal length for 600ms^{-1} atoms is thus $L_{\text{focus}} \approx 35 \text{mm}$. The same principle also holds for the y -axis.

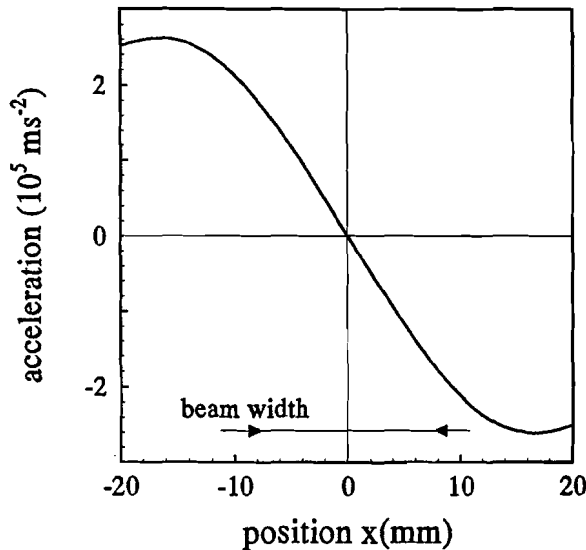


Figure 4.12: The acceleration of neon atoms as a function of the position for atoms in a quadrupole magnetic field when irradiated with σ^+ light from one side and σ^- light from the other side. The acceleration varies linearly with the position over the collimated beam width. Thus a lens for neutral atoms is obtained.

For atoms that are not on either the x or the y axis the picture is a little bit more complicated. In this case, the magnetic field is not in the direction of the laser beams. The magnetic field serves as the quantization axis for the magnetic substates. The laser beams are circularly polarized (σ^+/σ^-) with respect to their wave vectors. Using

rotation operators we can express the circular laser polarizations as linear superpositions of π , σ^+ and σ^- light with respect to the local magnetic field direction. The Zeeman resonance condition dictates how efficiently each of these polarization components can be absorbed. In the simulation, the detuning in equation 4.6 is modified with the Zeeman detuning Δ_{mag} . All laser beams are expressed in their polarization components with respect to the magnetic field, each with a different Zeeman detuning. The effective force for each polarization component of each laser beam is again calculated using equation 4.7. In the simulations, the lens appears to operate reasonably axially symmetric.

A different problem shows up if we want to make a strong lens: when the atoms have been accelerated towards the axis for a while, the acquired velocity causes a Doppler shift for the laser beams. Hence the optimal resonance condition is no longer fulfilled. In figure 4.11 this Doppler shift can be represented by an effectively larger laser detuning Δ . To compensate for this effect, we increase the magnetic field gradient as the atom moves downstream, keeping the optimal resonance condition. This way, the atoms can get a velocity of 20 ms^{-1} inwards. At the downstream end of the 50 mm thick lens the gradient is $1.2 \text{ Gauss mm}^{-1}$. The difference in Zeeman shift for the different transitions shown in figure 4.9 is no longer negligible. However, the simulations of the experiment show that the atoms are optically pumped to the outermost substates in the first part of the lens rather quickly. Thus the simplified picture remains valid.

4.2.3 Bright beam

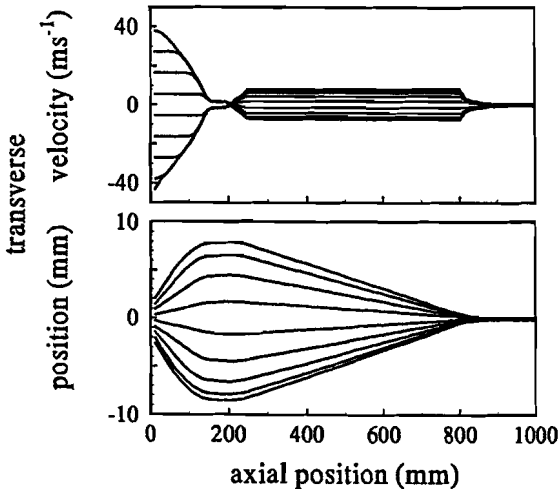


Figure 4.13: *Simulation of the complete beam brightening process. In velocity space (upper part) we can observe that the transverse velocity is first reduced to zero in the first collimating section ($0 < z(\text{mm}) < 150$), then reversed in the magneto-optical lens ($200 < z(\text{m}) < 250$) and finally reduced to zero again in last collimating section ($800 < z(\text{m}) < 950$). In the particle trajectories, we can observe that a high-flux, parallel atomic beam is obtained.*

A complete simulation of the three-stage brightening process is shown in figure 4.13. The atomic beam is first collimated, then focussed and recollimated near the focus. For 600 m/s atoms, the length of the beam brightener is one meter. In table 4.2 the parameters used for the simulation of figure 4.13 are displayed as well as the atomic

beam properties after these stages. The initially diverging atomic beam is compressed to a beam with a diameter of 1 mm.

	input		output	
initial			Δx	0.15 mm
			Δv_{\perp}	60 ms^{-1}
first stage	α	1.7 mrad	Δx	16 mm
	β_0	100 mrad	Δv_{\perp}	1 ms^{-1}
	Δ	$+4\Gamma$		
	L_{int}	150 mm		
second stage	dB/dr	2.12 Gauss/cm	Δx	18 mm
	Δ	$-\Gamma/2$	Δv_{\perp}	-10 ms^{-1}
	L_{int}	50 mm		
third stage	α	0 mrad	Δx	1 mm
	β_0	50 mrad	Δv_{\perp}	0.3 ms^{-1}
	Δ	$+4\Gamma$		
	L_{int}	150 mm		

Table 4.2: The optimal parameters for each cooling stage (input) and the one-dimensional beam properties after that cooling stage, as resulting from the simulation of figure 4.13.

4.3 Experimental design

4.3.1 Metastable atom source

The metastable atom source module is built as compactly as possible with an integrated differential pumping section. The source itself is cooled by liquid nitrogen to reduce the effective source temperature from 400 K to 150 K. The average axial velocity is thus reduced from 872 ms^{-1} to 558 ms^{-1} . The axial velocity spread is also reduced accordingly. This has great advantages for keeping the setup as compact as possible. First, to achieve a capture angle of 100 mrad in the collimating section, we only have to dissipate a transverse velocity component $v_{\perp} \approx 60 \text{ ms}^{-1}$. Second, since the axial velocity is smaller, the interaction time for a given interaction length is larger. This yields a smaller diameter beam after the first collimating section (see section 4.2.1). Third, a larger fraction of the beam fulfills the resonance conditions, since the axial velocity spread is smaller. The focal length of the magneto-optical lens scales with the source temperature as well, for the same reasons (see section 4.2.2). Finally, if we want to decelerate the collimated beam in the axial direction, we have a much better starting point.

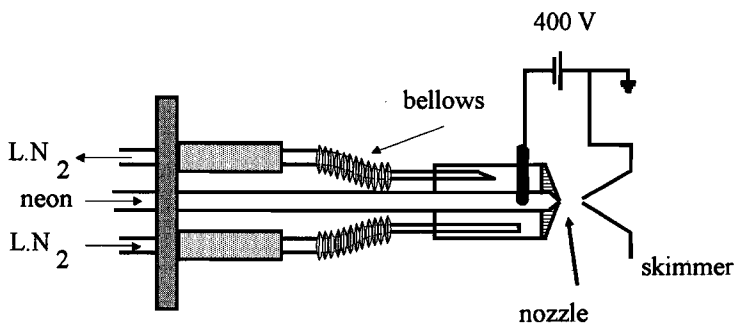


Figure 4.14: *The discharge excited metastable atom source. Of the two co-axial tubes the outermost is filled with liquid nitrogen. The inner tube is used for the gas feed. The separate boron-nitride nozzle plate is pressed to the flat side of the liquid nitrogen reservoir.*

A schematic impression of the thermal source itself is given in figure 4.14. The metastable atom beam is produced in a D.C. discharge that runs through the nozzle of a supersonically expanding jet. [13]. Although the excitation is rather efficient in general, the heat production in the nozzle is considerable. The skimmer also acts as (grounded) anode of the discharge. Since the gas has a negligible flow speed through the source tube, the expanding gas is thermalized with the area immediately around the nozzle hole. To get a beam of cold atoms, it is therefore necessary to cool the nozzle environment as effectively as possible. The nozzle plate is made of boron-nitride, which is an electrical insulator with a relatively good heat conductance. It is clamped to the liquid nitrogen reservoir with three springs. Typical operating conditions of the LN₂ cooled source are a source pressure $p_0 = 7 \text{ Torr}$, a nozzle diameter $D_n = 127 \mu\text{m}$ and

a 10 mA discharge current at a voltage of ≈ 400 V. The resulting center line beam intensity $I_0 = 2 \cdot 10^{12} \text{s}^{-1} \text{sr}^{-1}$, indicating a rather low degree of excitation as compared to other designs with $I_0 = 10^{14} - 10^{15} \text{s}^{-1} \text{sr}^{-1}$ [14]. However, the source is excellently suitable for demonstration of the beam brightener. In figure 4.15 the reduction of the axial velocity is demonstrated using time-of-flight velocity analysis. The time-of-flight apparatus is discussed in, e.g., reference [15].

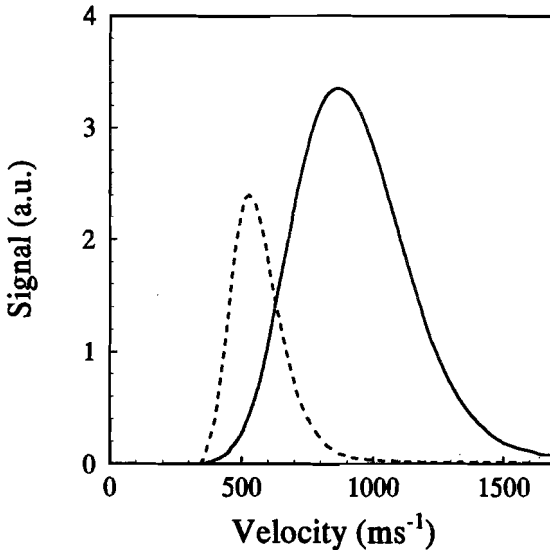


Figure 4.15: *Measured velocity distributions for the uncooled (full line) and liquid nitrogen cooled (dashed line) thermal source. Both the average velocity and the velocity spread are reduced by a factor of two.*

4.3.2 Collimating stages

The design criterion for the collimating sections is that a beam initially diverging in a cone with a half top angle of 100 mrad has to be captured in a collimated beam. On the basis of the simulations, we choose the length of the mirrors to be 150 mm. The angle between the mirrors α has to be adjustable in the range from 0 to 5 mrad. In the other dimension, the mirrors have to be parallel to within 0.1 mrad. Hence we need a very good method to determine these angles. These requirements were met by the mirror holders, of which an artist's impression is shown in figure 4.16. The holders are carefully machined to keep the mirrors exactly parallel to within 0.1 mrad in both dimensions, without any adjustments. A small angle α can be introduced by using shims (typically 50-500 μm thick) at one end of the holder. To determine the angle α a test laser beam is coupled between the mirrors at an angle β_0 . The exit angle β_N is determined together with the number of reflections N . The angle α can then be calculated using $\alpha = (\beta_0 - \beta_N)/N$. For the results described in section 4.4 50 μm shims were used, resulting in an angle $\alpha = 0.5$ mrad.

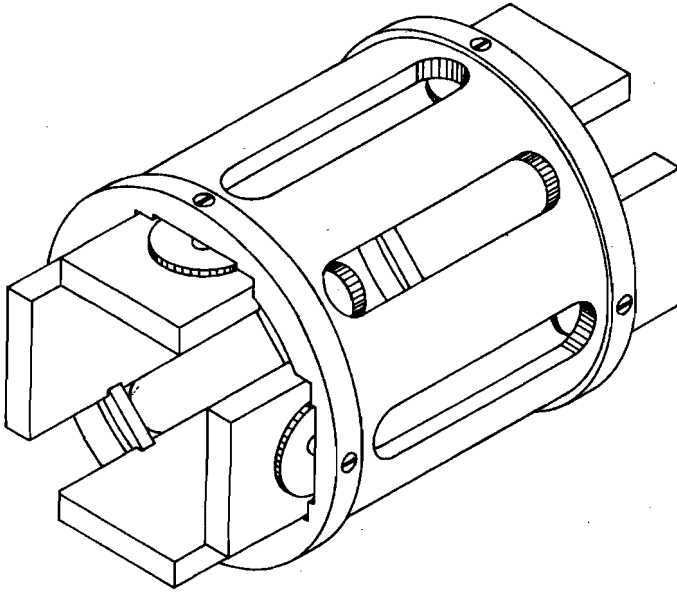


Figure 4.16: *Artist's impression of the mirror holders. Without any adjustments, the mirrors are parallel to 0.1 mrad by machine shop precision.*

4.3.3 Magneto-optical lens

The magneto-optical lens is designed in two modules: a 'magnetical' and an 'optical' module. For the optical module, we require that the atomic beam interacts over 50 mm with the laser field to get a strong lens. For a saturation parameter $s = 1$ ($40.8 \mu\text{W}/\text{mm}^2$) for a single laser beam with dimensions 25×50 mm 50 mW of laser power is required. For two-dimensional focussing, four laser beams are needed, which would mean a total laser power of 200 mW. Therefore, we re-use the laser light of one beam in four directions, as indicated in figure 4.17. The vacuum chamber acts as a precision made, non-adjustable mirror holder, greatly simplifying the laser alignment. The shaded area of $40 \times 40 \text{mm}^2$ is entirely illuminated from four sides with the correct laser polarizations. Special non-polarizing highly reflective mirrors [16] are used to maintain the circular polarization after eight reflections. We use a Gaussian laser beam with a waist radius ($1/e^2$ intensity drop) of 30×15 mm for this section to achieve homogeneous illumination of the interaction region.

Since the required magnetic field in the interaction region is typically smaller than 20 Gauss, we use permanent ferrite magnets outside the vacuum chamber. This allows for easy tailoring of the magnetic field while testing the setup. In figure 4.18 the quadrupole field gradient on the axis as a function of the axial distance from the center of the magnets is shown. We can use the fringe fields outside the 45 mm radius of the magnets to achieve the required approximately linearly increasing field gradient. An advantage of using this configuration is that the magnets are not in the path of the laser

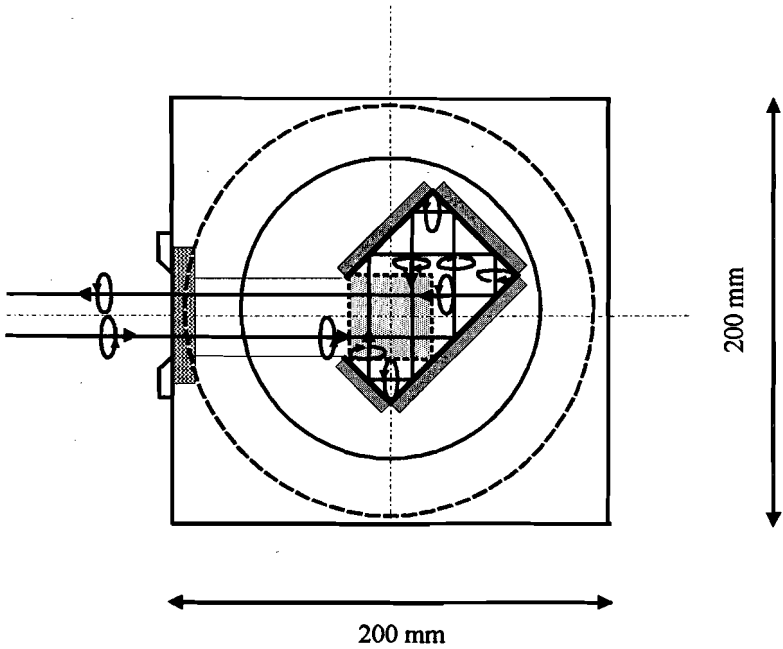


Figure 4.17: Side view of the optical module of the magneto-optical lens. The atomic beam is illuminated from four sides with the correct laser polarization using only one laser beam. The arrows indicate the polarization of the laser beams.

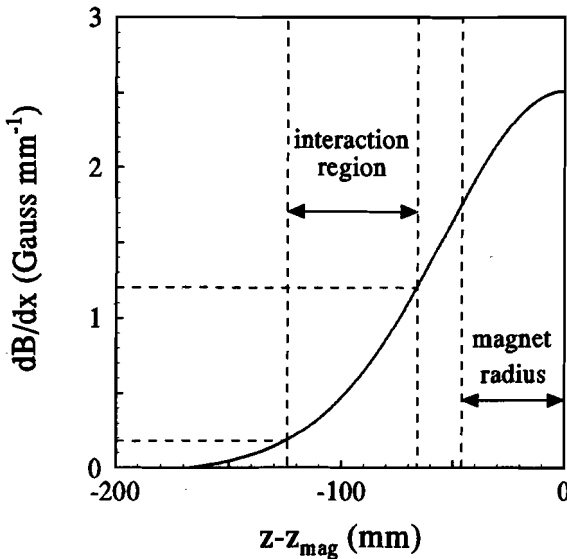


Figure 4.18: The quadrupole magnetic field gradient as a function of the position along the quadrupole axis. To achieve an increasing gradient, we use the fringe field as indicated here.

beam. In our setup, the position of the magnets with respect to the interaction region is precisely adjustable to achieve the proper magnetic field gradients in the interaction region.

4.3.4 Laser equipment

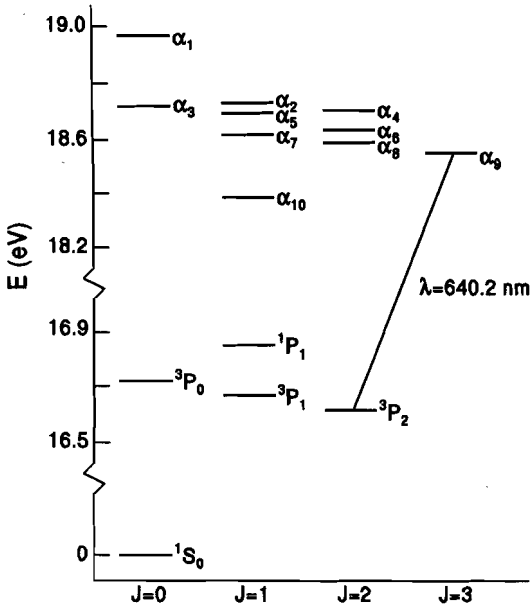


Figure 4.19: Part of the level scheme of neon. The lifetime of the metastable $3P_0$ and $3P_2$ states has been calculated to be 430 s and 24.4 s respectively [17]. For the cooling process we use the closed-level transition from the $\{3s\}3P_2$ state to the $\{3p\}3D_3 = \{\alpha_9\}$ state at 640.225 nm.

The whole setup is operated using a single dye laser. It is a commercial Spectra-Physics 380D ring dye laser pumped by a small frame Coherent Innova 70 Argon-ion laser operating on DCM dye [18]. The amount of laser power necessary for the total beam compression scheme is about 200 mW. In figure 4.19 part of the level scheme of neon is displayed. The cooling transition is the closed-level transition from the metastable $3P_2$ state to the $\{\alpha_9\}$ state at 640.225 nm. The laser is stabilized to a Zeeman-modulated and -shifted saturated absorption gas discharge cell. The laser frequency is thus known to an accuracy of 1 MHz.

An overview of the laser setup is shown in figure 4.20. The laser beam is divided in two beams by a beam splitter. One laser beam is shifted over 40 MHz using an acousto-optic frequency shifter. This detuning is required to compensate for the remaining Doppler shift at angle $\beta = \beta_N$, as discussed in section 4.2.1. The frequency-shifted laser beam is split in two parts needed for the first and third cooling stages. Both these beams are expanded and divided in four parts using plate beamsplitters to obtain the four beams that are coupled between the mirrors of the collimating sections in the $\pm x$ and $\pm y$ directions. In the setup all beam splitters and mirrors necessary for one collimation stage are mounted on one big translatable mount. This allows for very precise manipulation of each laser beam and ensures quick and reproducible alignment. When coupled between the mirrors, the Gaussian laser beams have waist

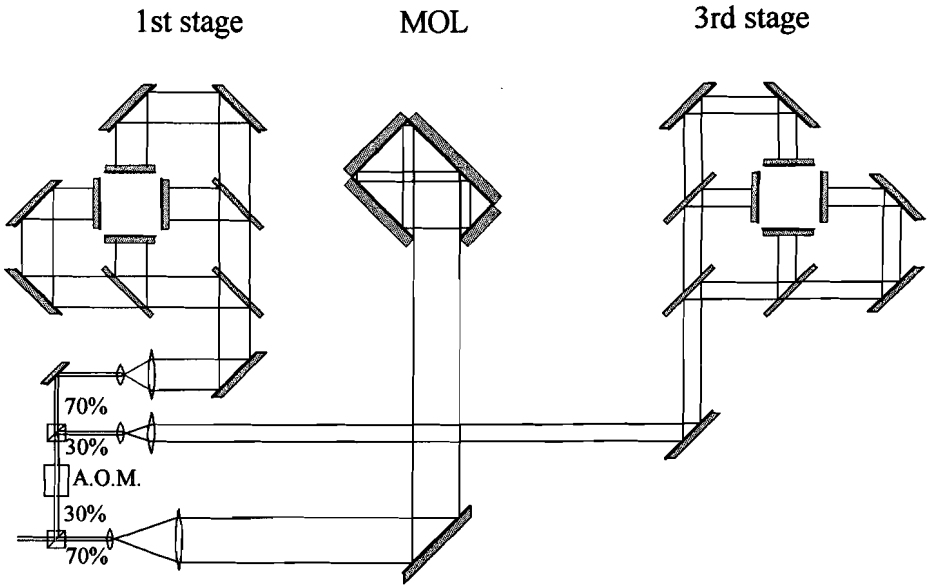


Figure 4.20: An overview of the laser beam handling in the experiment. The part of the laser beam that is used for the collimating sections, is split off first and frequency shifted using an acousto-optic modulator.

radii $w_z = 3$ mm for the axial direction and $w_x = 4$ mm in the other dimension. In the latter dimension, it is slightly diverging to compensate for the expansion of the atomic beam while it passes the mirror section.

The unshifted laser beam is also expanded using a cylindrical telescope to a waist size of $w_z \times w_x = 30 \times 15$ mm² and is used for the magneto-optical lens.

4.3.5 Beam diagnostics

The operation of all sections is tested using two ‘cold wire’ detectors. Due to the large internal energy of metastable neon (16.5 eV) (see figure 4.19) atoms can be detected by Auger emission of an electron from a metal surface. Due to the large fluxes as in our setup, the current is in the nano-Ampere range which can easily be measured. Charged particles and UV photons that are formed in the discharge are detected this way as well. We measured the fraction of the signal due to these particles by quenching the 3P_2 metastable atoms with the laser tuned to the transition to the $\{\alpha_8\}$ state, which decays in a cascade to the non-detected ground state. Near the source, this amounts to a considerable correction. The wire-scanners consist of a stainless steel 1.0 mm diameter wire that is moved through the atomic beam by a stepper motor. The ejected electrons are accelerated to two auxiliary wires, thereby preventing the buildup of a space charge. The wire scanners are built as self-contained in-vacuum units, that can be used at any position in the beam line in either the horizontal or the vertical direction. Thus we can

either take a two-dimensional beam profile at one position or a one-dimensional profile at two positions.

For fast monitoring of the atomic beam profile a micro-channel plate beam imager is used at the end of the setup. It consists of an open face micro-channel plate (MCP) with a phosphor screen anode. A metastable atom that hits the MCP frees an electron that is amplified by the MCP and accelerated to the phosphor screen. A CCD camera constantly views the phosphor screen. The video image can be digitized to take quantitative measurements. A typical beam profile obtained with the MCP is shown in figure 4.21. Due to the large beam fluxes however, the gain of the MCP at the central position of the compressed beam has decreased. This limits its use for quantitative measurements.

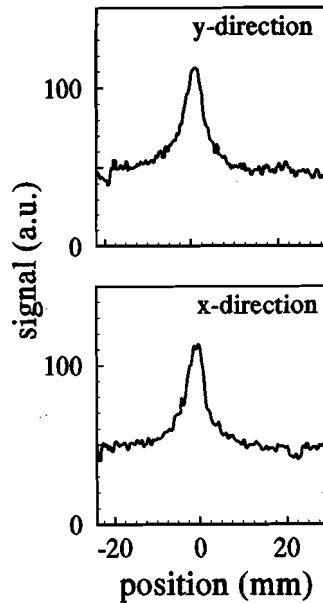
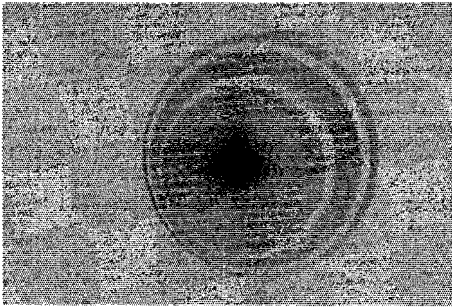


Figure 4.21: A typical compressed beam profile taken with the MCP detector. On the left, the MCP image is shown. On the right, a vertical (upper part) and a vertical (lower part) profile as obtained by digitizing the MCP image are displayed.

4.3.6 Beam setup

The setup is modularly designed to allow for rapid adjustments in the operation. All modules are built as aluminum vacuum sections sealed with O-rings to enable a quick turnaround in case the setup has to be modified to accommodate new insights. An overview of the implementation of the vacuum parts is shown in figure 4.22. The source chamber (1) is separated from the main vessel (3) by a differential pumping chamber (2). All three pumping stages are supplied with turbomolecular pumps to achieve an oil-free vacuum. The residual background pressure in the main vessel is 10^{-6} mbar,

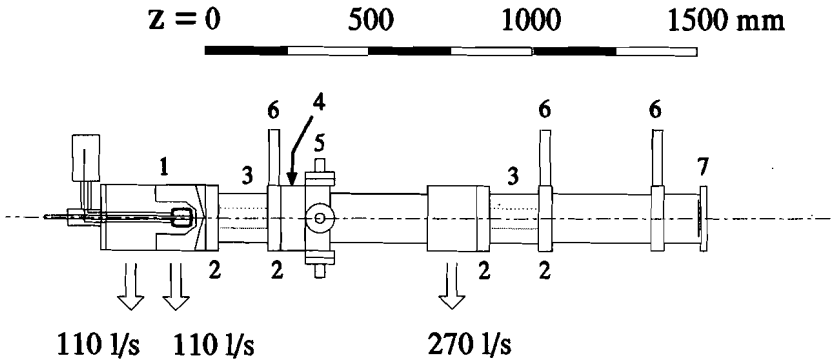


Figure 4.22: An overview of the vacuum setup. The source module (1) has a built-in differential pumping section, pumped with a separate turbopump. The collimation stages consist of two coupling modules (2) and a tubular spacer module (3), as discussed in the text. The magneto optical lens is built in an optical (4) a magnetical (5) module. The wire scanners (6) can be inserted at any position in the beam path, either horizontally or vertically. The MCP detector (7), mounted at the end of the beam line, provides on-line information about the cooling process.

and is limited by the gas load on the source chamber and the size of the apertures between the chambers.

The collimating sections are built in three modules each: two light coupling modules, containing four anti-reflection coated vacuum windows to pass the laser beams and two inspection windows each, separated by a tubular spacer module. The laser beam is coupled in the first coupling module. The mirror holder is situated the spacer module, but lies on two rails, which are suspended in the coupling modules. The alignment of the mirror section is therefore completely determined by the machining accuracy of the coupling modules and their alignment with respect to each other. The compact construction of coupling modules and source module allows us to start the cooling process 20 mm after the metastable atom source nozzle. Thereby we prevent the atomic beam from expanding too much before entering the collimating stage. To allow for easy visual inspection of the alignment, the spacer module was at times replaced by a plexiglass spacer.

To determine the divergence of the compressed atomic beam a drift section is added after the last collimating section. Using the wire scanners and micro channel plate as discussed before, the final divergence and beam diameter of the compressed atomic beam can be determined.

4.4 Results

4.4.1 First collimating stage

The operation of the first collimation section is tested using two 'cold wire' detectors, one immediately after the first collimating section at 210 mm and one immediately after

the last collimating section at 1040 mm downstream from the thermal source. The cold wire detectors are discussed in detail in section 4.3.5. Typical collimated beam profiles

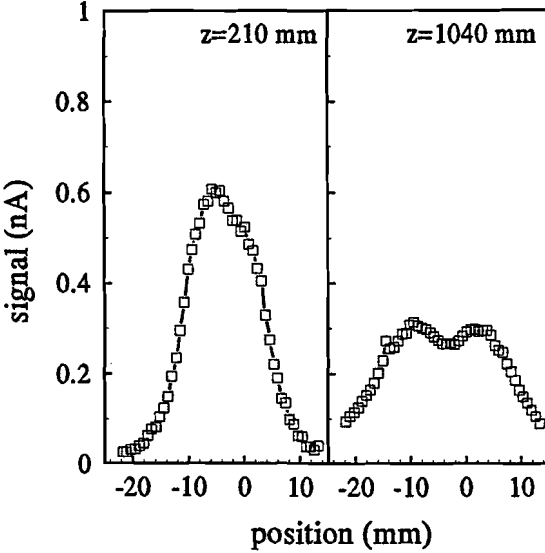


Figure 4.23: Atomic beam profiles, measured using the wire scanners at (left part) 210 mm and (right part) 1040 mm downstream from the source, with only the first section in operation. The block-like beam profile has a residual divergence of ≈ 4 mrad, as determined from the widths.

are shown in figure 4.23. A block-like beam profile is observed, with a dip on the beam axis. The profile is slightly diverging, with a residual half angle divergence (determined from the FWHM of the profile) of 2 mrad. The required laser power is about 30 mW for two-dimensional collimation. The figure shows that all atoms passing through the collimating apertures, which have a half acceptance angle of 0.1 rad, are captured in an atomic beam with a diameter of approximately 20 mm. The small decrease in the center of the profiles can be understood by the following argument: Atoms with a rather small initial transverse velocity are hardly resonant at the beginning of the collimating section, and continue to move outward until they are resonant. On the other hand, atoms with a larger velocity are immediately decelerated, but need a longer interaction time before they are collimated. Consequently, most atoms will end up away from the beam axis. This is reproduced by a simulation of the experiment, as described in section 4.2.3.

The resulting divergence of 2 mrad, is much larger than the Doppler limit (divergence ~ 0.5 mrad). Part of the explanation lies in the fact that it is very difficult to achieve a good overlap of the left- and right going (or up- and down going) laser beams at the very end of the mirror section. This increases the atomic beam divergence. The residual spread in the axial velocity, combined with the finite angle β_N at the end of the mirror section increases the observed divergence as well. The divergence after this section can be greatly reduced by using a second cooling stage consisting of a pure standing wave of linearly polarized laser light in two dimensions. The collimated atomic beam is much too large for most applications. However the beam flux is high.

4.4.2 Magneto-optical lens

The operation of the magneto-optical lens is tested with both the wire scanners described in section 4.3.5 and the micro-channel plate beam imager. The wire scanners allow quantitative measurements of the beam profile. They are located at 1040 mm and 1380 mm downstream of the source respectively. The MCP beam imager is located at the end of the setup, at 1283 mm downstream of the center of the lens, and provides on-line qualitative information. A typical focussed beam profile taken by the wire scanners is shown in figure 4.24. A typical beam diameter (FWHM) of 4 mm is achieved

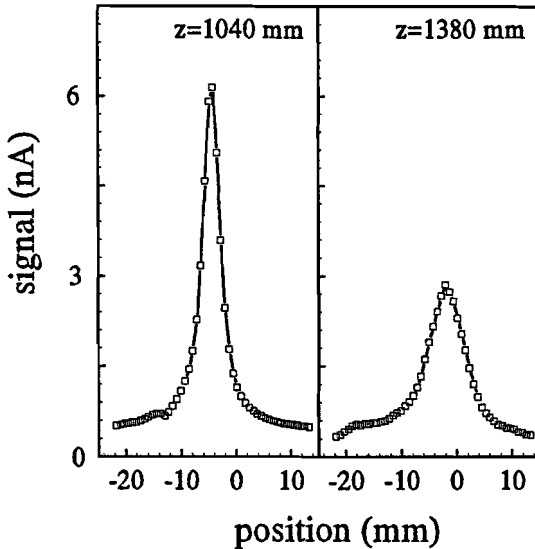


Figure 4.24: A measured focussed beam profile taken with the wire scanners, at (left part) 1040 mm (right part) 1380 mm downstream from the source. The center of the MOL is located at $z_{\text{mol}} = 267$ mm. The focus of the atomic beam is located near the first wire.

near the focus. Note that this is without any conventional collimating elements in the beam and with the full beam flux. To determine the width, these profiles are fitted to a Lorentzian profile using a least-squares procedure. For tests, part of the laser beam at the downstream side of the lens is blocked to achieve a larger focal distance. In figure 4.25 we plot the width of the atomic beam profile at the two wire scanners as a function of the active fraction of the lens. We clearly observe that the width at the second wire has a clear minimum when 25% of the lens is blocked. The beam width at the first wire has a minimum when the last 10% of the lens is blocked. Estimating from these results, the focus should be in the last collimating section when the lens is completely unblocked.

In figure 4.26 we plot the focus size and peak signal of the atomic beam at the first wire scanner as a function of the position of the magnets with respect to the interaction region. We clearly observe a minimum in the beam focus size coinciding with a maximum in the peak signal, indicating that the focal length of the lens can be adjusted by changing the quadrupole field strength as well.

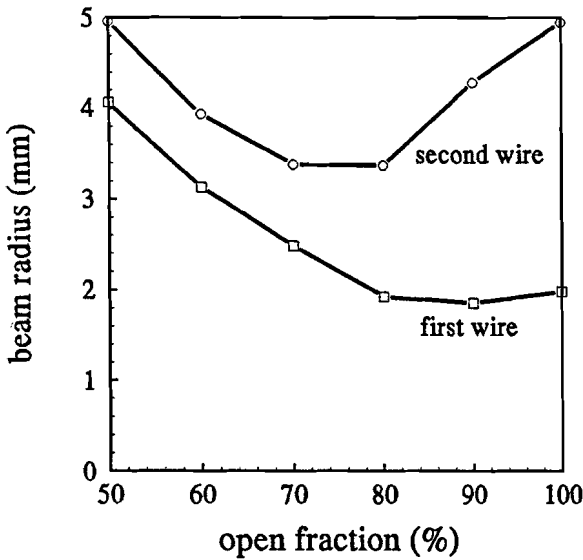


Figure 4.25: The beam radius (HWHM) of the atomic beam at the first and second wire scanners, located at 1040 mm 1380 mm downstream of the source respectively, when part of the laser beam in the lens is blocked.

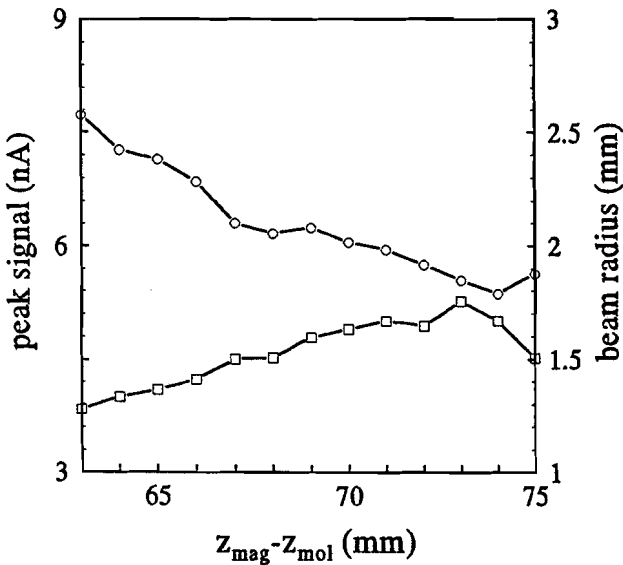


Figure 4.26: The beam radius (HWHM) (\circ) and the peak signal (\square) of the atomic beam as measured by a wire scanner at 1040 mm downstream from the source when the distance $z_{\text{mag}} - z_{\text{mol}}$ from the magnets to the center of the interaction region in the lens is varied.

4.4.3 Bright beam characteristics

With all stages in operation, a very intense and well-collimated atomic beam is obtained. In figure 4.27 measured beam profiles using the wire scanners are displayed. The collimated atomic beam has an initial diameter of 4.0 mm FWHM and diverges at 2 mrad.

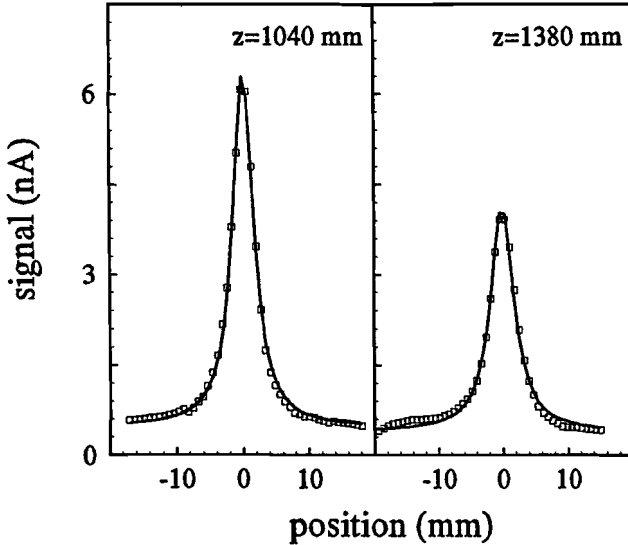


Figure 4.27: *Measured beam profiles with the last collimating section in operation, measured at 1040 (left part) and 1380 mm (right part) downstream of the metastable source respectively.*

After the MOL, the beam converges with a maximum half-angle of 14 mrad. Hence, the maximum transverse velocity $v_{\perp} \approx 9 \text{ms}^{-1}$, as compared to 60ms^{-1} for the atoms entering the first collimation stage. This allows the recollimation stage to be operated at $\alpha = 0$, i.e., without chirp in the effective detuning. However, choosing the effective detuning through the angle β still requires some trade-off between the capture range and the final divergence. This is demonstrated in figure 4.28. In this figure we plot the final beam divergence and the peak signal as a function of the coupling angle of the laser beams β and thus the effective detuning Δ_{eff} in the last collimating section. With increasing β , an increasing divergence is observed, indicating a higher final temperature. The peak height decreases with increasing β , indicating the limited capture velocity of the cooling process. The tradeoff can be avoided by introducing a very small angle α between the mirrors in the final cooling section. This angle should be ≈ 0.1 mrad, which means $10 \mu\text{m}$ spacers should be inserted at one end of the mirror holder.

4.4.4 'Brightness' vs. signal gain

A 'figure of merit' for the entire compression scheme can be obtained in several ways. One criterion, which is often applicable to experimental situations, is the increase of the total metastable atom flux \dot{N} that would pass a diaphragm with, e.g., an area $A = 1 \text{mm}^2$ at a distance $z = 1 \text{m}$ from the thermal source. The flux gain can now be

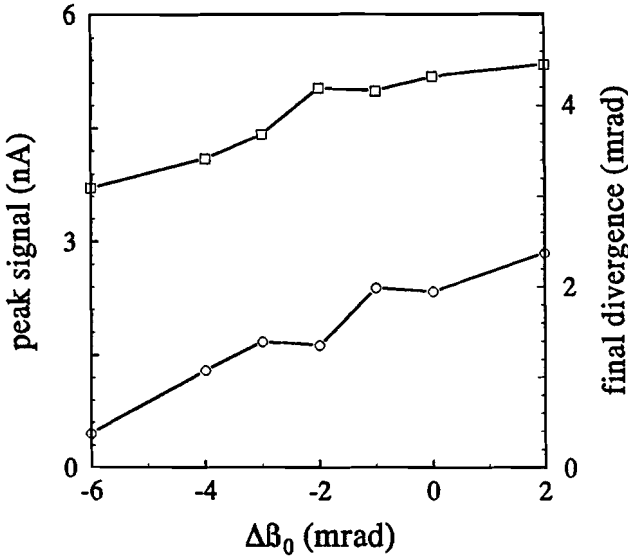


Figure 4.28: The final beam divergence (\circ) and peak signal (\square) as a function of the relative coupling angle in the final collimating section as measured by the wire scanners. As the coupling angle decreases, Δ_{eff} is decreased and thus the capture range of the cooling process.

defined as

$$\frac{\dot{N}_{\text{on}}}{N_{\text{off}}} = \frac{I_{\text{on}}}{I_0 A / z^2} = 1600 \quad (4.9)$$

with I_0 the center line beam intensity of the source, which is measured when the cooling lasers are off, and I_{on} the measured signal with the cooling lasers on.

Another measure is the beam divergence. The initial divergence of 100 mrad is decreased to ≈ 2 mrad, while maintaining the full source flux. In two dimensions this means that the divergence has decreased with a factor of 2500.

Unlike in traditional optics, using laser cooling it is even possible to increase the phase space density in the atomic beam. We estimate that the ‘brightness’ of the beam, i.e., the number of atoms per unit of phase space volume has increased by a factor of nine. Hereby we demonstrate that Liouville’s theorem is not valid for laser cooled atomic beams.

The absolute signal in our experiments is rather small due to the small source flux $I_{\text{source}} \approx 10^{12} \text{ s}^{-1}$ of the metastable atom source. By improving the source design, as, e.g., described by Shimizu *et al.* [14], we expect to gain a factor of ≈ 100 in absolute beam flux. Combined with the beam brightener as described here, an ultra intense metastable atom beam will be obtained.

4.5 Final remarks and future prospects

We have given the design and demonstrate the operation of a high-flux atomic beam brightener for neutral atoms. A solid angle of $3 \cdot 10^{-2}$ sr of the source flux is captured in a small diameter atomic beam with low divergence. Chromatic aberrations of the magneto-optical lens are the major cause of the final ≈ 4 mm beam diameter, even for the supersonic beam used. The measured beam intensification at the end of the setup

is a factor of 1600. The beam can be collimated to a divergence of 0.3 mrad, which is the Doppler limit.

The required laser power can be reduced by re-designing the magneto-optical lens proposed by Driessen [19]. In this design the laser beam alternatively undergoes *s*- and *p*-reflections on the mirrors. Thus residual polarizing effects of the dielectric mirror coatings in the lens can be eliminated. This new version is expected to be in operation by the summer of '93.

The final beam diameter can be reduced by using an additional restoring force, like in a magneto-optical trap, in the last collimating section. This would reduce the influence of a non-perfect focus of the lens on the beam diameter significantly. The design of such a section is in progress.

The final beam divergence can be reduced by using a sub-Doppler cooling section after the last collimating section. This should reduce the divergence to less than 0.2 mrad, close to the recoil limit.

Acknowledgements

The authors would like to acknowledge stimulating discussions with Peter van der Straten and Harold Metcalf. This work is financially supported by the Dutch foundation for Fundamental Research on Matter (FOM).

References

- [1] D.J. Wineland and H. Dehmelt. *Bull. Am. Phys. Soc.* **20**, 637(1975).
- [2] T.W. Hänsch and A.L. Schawlow. *Opt. Comm.* **13**, 68(1975).
- [3] S. Chu, L. Hollberg, J. E. Bjorkholm, A. Cable, and A. Ashkin. *Phys. Rev. Lett.* **55**, 48(1985).
- [4] K. Gibble and S. Chu. *Phys. Rev. Lett.* **70**,1771(1993).
- [5] See: special issue on atomic optics and interferometry in *Appl. Phys.* **B54** (1992).
- [6] See: special issue on Laser Cooling and Trapping of atoms in *J. Opt. Soc.* **B6**, (1989).
- [7] P.D. Lett, W.D. Phillips, S.L. Rolston, R. N. Watts C.E. Tanner, and C.I. Westbrook. *J. Opt. Soc. Am.* **B6**, 2084(1989).
- [8] E. Raab, M. Prentiss, A. Cable, S. Schu, and D. Pritchard. *Phys. Rev. Lett.* **59**, 2631(1987).
- [9] J. Nellesen, J.H. Müller, K. Sengstock, and W. Ertmer. *J. Opt. Soc. Am.* **B6**, 2149(1989).
- [10] H.J. Metcalf. *J. Opt. Soc. Am.* **B6**, 2206(1989).
- [11] M. Zhu, C.W. Oates, and J.L. Hall. *Phys. Rev. Lett.* **67**,46(1991).

-
- [12] Friedburg and Paul. *Z. f. Phys.* **130**, 493(1951).
 - [13] M.J. Verheijen, H.C.W. Beijerinck, L.H.A.M. van Moll, J. Driessen, and N.F. Verster. *J. Phys.* **E17**, 904(1984).
 - [14] J. Kawanaka, M. Hagiuda, K. Shimizu, F. Shimizu, and H. Takuma. *Appl. Phys.* **B56**, 21(1993).
 - [15] H.C.W. Beyerinck. PhD thesis, Eindhoven University of Technology, 1975.
 - [16] The non-polarizing mirror coatings were manufactured by LaserOptik GmbH, Garbsen (Germany).
 - [17] N.E. Small-Warren and L.Y. Chin. *Phys. Rev.* **A11**, 1777(1975).
 - [18] 4-dicyanomethylene-2-methyl-6(*p*-dimethyl-amino-styryl)-4H-pyran.
 - [19] J.P.J. Driessen. private communication.

Summary

In this thesis we study the force that laser light exerts on neutral atoms, in our case metastable ($\{3s\}^3P_2$) neon atoms. Using this force, it is possible to cool free atoms to very low temperatures, in the order of a few microKelvin. Presently, many applications of these cold atoms are put forward in the fields of, e.g., ultra-high resolution spectroscopy, atomic frequency standards and atomic collision physics. The present study was carried out in the Atomic Collisions and Spectroscopy group at the Physics Department of the Eindhoven University of Technology.

In chapter 2, we use radiation pressure on atoms to study the photon statistics of resonance fluorescence. We measure the deflection of an initially well-collimated atomic beam by a running laser wave. The number of photons scattered by an atom during the interaction time can be deduced from the deflection of the atom. Thus, by analyzing the average deflection and the spread therein, we can determine the photon number statistics. The expected sub-Poissonian statistics are a manifestation of the quantummechanical nature of light. We present extensive experimental results, that give the deviation from Poissonian photon statistics as a function of the intensity, detuning, and polarization of the exciting laser field. We compare the data with both the two-level theory and the results from a numerical simulation of the experiment. The numerical simulation is based on the derived explicitly real-valued expression for the integrated photon waiting time distribution. Due to a transient effect a large difference is observed between the two level theory and our experimental data in case of excitation with circularly polarized laser light. However, excellent agreement between the experimental data and the numerical simulation is demonstrated.

The exact mechanisms that lead to laser cooling to very low temperatures have been the subject of detailed theoretical studies. The only experimental data until now however, are measurements of the final temperatures that give only limited insight in the dynamics of the cooling process. In chapter 3, we experimentally study these dynamics by measuring the deflection of a very well-collimated atomic beam by a well-defined (quasi-)standing laser wave. By choosing the angle between the laser beam and the atomic beam, the atoms can be given a well-defined initial velocity v_{\perp} in the direction of the laser beams in the range $-1 \leq v_{\perp}(\text{ms}^{-1}) \leq 1$. From these deflection measurements, the 'sub-Doppler cooling forces' as well as the diffusion coefficients in these processes can be measured directly as a function of the initial atomic velocity. The experimental results are compared to quantum Monte-Carlo simulations and semiclassical calculations. We observe excellent agreement. In the $\sigma^+\sigma^-$ cooling configuration, we observe transient effects due to the slow evolution of the distribution over the magnetic substates to an equilibrium. We also observe channeling of atoms in weak standing waves and demonstrate the applicability of the well-known Sisyphus picture for the $\pi^x\pi^y$ cooling scheme.

In chapter 4, we present the design and demonstrate the operation of an 'atomic beam intensifier' for neutral atoms using a combination of laser cooling techniques. A beam of Ne^* atoms, initially diverging in a cone with an opening angle of 0.2 rad, is first collimated by a variation of the 'Doppler' cooling technique using effectively curved wavefronts. The resulting collimated atomic beam with a rather large diameter is then focussed by a magneto-optical lens and recollimated near the focus by Doppler cooling. This results in a beam with a diameter of 4 mm and a divergence of 0.004 rad,

containing the full flux of the original beam. The increase in centerline beam intensity is a factor of 1600. The intensified atomic beam opens up a whole new range of possible applications in atomic physics.

Samenvatting

In dit proefschrift bestuderen we de kracht die laserlicht uitoefent op neutrale atomen, in ons geval metastabiele ($\{3s\}^3P_2$) neon atomen. Gebruikmakend van deze krachten is het mogelijk vrije atomen tot zeer lage temperaturen, in de orde van enkele microKelvin, te koelen. Op dit moment blijken er veel toepassingsmogelijkheden van koude atomen te bestaan in onderzoeksgebieden als ultrahoge resolutie spectroscopie, atomaire frequentiestandaarden en atomaire botsingsfysica. Het hier gepresenteerde onderzoek is verricht in de werkgroep Atomaire en Optische Wisselwerkingen van de faculteit Technische Natuurkunde van de Technische Universiteit Eindhoven.

In hoofdstuk 2 gebruiken we stralingsdruk op atomen om de fotonstatistiek van resonantie-fluorescentie te bestuderen. We meten de afbuiging van een goed gecollimeerde atoombundel door een lopende lasergolf. Het aantal fotonen dat gedurende de interactietijd door een atoom wordt verstrooid, kan worden afgeleid uit de afbuiging van het atoom. Zo kan door het analyseren van de gemiddelde afbuiging en de spreiding daarin de fotonstatistiek worden bepaald. De verwachte sub-Poissonstatistiek is een directe consequentie van het quantummechanische karakter van licht. We tonen uitgebreide experimentele resultaten die de afwijking van de Poissonstatistiek laten zien als functie van de intensiteit, verstemming en polarisatie van de invallende laserbundel. We vergelijken de metingen zowel met de twee-niveau theorie als met een numerieke simulatie van het experiment. De numerieke simulatie is gebaseerd op een in dit proefschrift afgeleide, expliciet reële uitdrukking voor de geïntegreerde foton-wachttijdverdeling. Ten gevolge van een ingroei-effect nemen we in het geval van circulair gepolariseerd laserlicht een groot verschil waar tussen de twee-niveaustheorie en onze experimentele data. Er is echter wel een uitstekende overeenkomst tussen de experimentele data en de numerieke simulatie.

De precieze mechanismen die leiden tot laser koeling tot zeer lage temperaturen zijn theoretisch uitgebreid onderzocht. Echter, de enige experimentele gegevens tot nu toe bestaan uit metingen van de eindtemperatuur en geven slechts een beperkt inzicht in de dynamica van het koelproces. In hoofdstuk 3 bestuderen we deze dynamica experimenteel door de afbuiging te meten van een zeer goed gecollimeerde atoombundel door een goed gedefiniëerde (quasi-)staande lasergolf. Door de keuze van de hoek tussen de laserbundel en de atoombundel kan de atomen een goed gedefiniëerde beginsnelheid v_{\perp} in de richting van de laserbundel worden gegeven in het bereik $-1 \leq v_{\perp}(\text{ms}^{-1}) \leq 1$. Uit deze metingen van de bundeldeflectie kunnen zowel de 'sub-Doppler' koelkrachten als de diffusiecoëfficiënten in deze processen direct worden gemeten als functie van de beginsnelheid van de atomen. De experimentele resultaten worden vergeleken met quantum Monte-Carlo simulaties en semiklassieke berekeningen. We vinden een uitstekende overeenkomst. In de $\sigma^+\sigma^-$ configuratie vinden we ingroei-effecten ten gevolge van de langzame evolutie van de verdeling over de magnetische subtoestanden. We nemen ook het kanaliseren van atomen in zwakke staande golven waar en we demonstren de bruikbaarheid van het bekende Sisyphus-beeld voor het $\pi^x\pi^y$ koelschema.

In hoofdstuk 4 presenteren we het ontwerp en demonstren we de werking van een 'atomaire bundelcompressor' voor neutrale atomen, die gebruik maakt van laserkoel-

technieken. Een divergerende bundel Ne^* atomen met een openingshoek van 0.2 rad wordt eerst gecollimeerd door een variant op de 'Doppler' koeltechniek, waarbij gebruik wordt gemaakt van effectief gekromde golffronten. De resulterende brede, gecollimeerde atoombundel wordt dan gefocusseerd met behulp van een magneto-optische lens en bij het brandpunt weer door Dopplerkoeling gecollimeerd. Het resultaat is een bundel met een diameter van 4 mm en een divergentie van 0.004 rad, waarbij de volledige, oorspronkelijke bundelflux bewaard blijft. De centrale bundelintensiteit wordt met een factor 1600 vergroot. De intense atoombundel opent een heel nieuw gebied van mogelijke toepassingen in atoomfysische experimenten.

Dankwoord

Ik wil iedereen bedanken die aan de totstandkoming van dit proefschrift heeft bijgedragen. In de afgelopen vier jaar hebben velen mij bijgestaan. In het bijzonder denk ik dan aan mijn copromotor Ton van Leeuwen, waarmee ik een vier jaar durende, onbesliste wedstrijd in slordigheid ben aangegaan waarin wij ons beiden uitstekend thuis voelden. Verder mijn promotor Herman Beijerinck, met wie ik zeer veel zeer levendige discussies heb gehad. Ook de technici Louis van Moll en Rien de Koning, de constructeur Piet Magendans, de secretaresse Marianne vd Elshout en tekenwonder Ruth Gruyters hebben een onmisbare bijdrage geleverd aan dit werk. Datzelfde geldt ook voor mijn afstudeerders Henry Megens, Erik de Bie, Mark Schuwer, Anne den Boer en Evert-Jan Vonken, alle overige AOW-ers, ex-AOW-ers en alle stagairs zonder wie dit alles niet mogelijk was geweest. Zij hebben allen veel geduld met mijn nukken opgebracht. Voor hun bijdragen zowel op het spirituele als op het materiële vlak wil ik tenslotte mijn ouders alswel Gerard en Heidy nog eens extra in het zonnetje zetten.

Curriculum Vitae

- 3 juli 1966 geboren te Bussum
- juni 1984 eindexamen ongedeeld VWO,
Rijnlands Lyceum Oegstgeest.
- 1984–1989 Studie Natuurkunde aan de
Rijksuniversiteit Leiden.
- juni 1989 Doctoraal examen Experimentele Natuurkunde,
Rijksuniversiteit Leiden.
- 1989–1993 Onderzoeker in Opleiding bij de Stichting FOM,
werkgroep QE-E, Atomaire en Optische Wisselwerkingen,
Technische Universiteit Eindhoven.
- 1993– Post-doc positie bij het
National Institute of Standards and Technology
Gaithersburg, Maryland, USA.

STELLINGEN

behorende bij het proefschrift

LASER MANIPULATION OF METASTABLE NEON ATOMS

1. Bij lage etssnelheden in een systeem van Si, dat geëtsd wordt door thermisch XeF₂, is de verhoging van de etssnelheid bij beschieting van het substraat met 1 keV ionen geen gevolg van fysisch sputteren van het belangrijkste etsproduct, SiF₄.

G.J.P. Joosten, M.J.M. Vugts, H.J. Spruijt, H.A.J. Senhorst and H.C.W. Beijerinck, voorgelegd aan J. Vac. Sci. Technol. A.

2. De identiteit

$$\prod_{n=1}^{\infty} \frac{(1+p^{6n-5})(1+p^{6n-1})(1+p^{3n})}{(1+p^{6n})(1+p^{2n-1})} = 1 \quad \forall p \text{ zdd } 0 \leq p < 1$$

laat zien dat ook de wiskunde omslachtig taalgebruik kent.

3. Indien een ontsnapte gevangene in een stad met een rechthoekig stratenpatroon bij iedere straathoek willekeurig links of rechts af slaat om zijn achtervolgers te verwarren, en nooit tweemaal hetzelfde straatdeel kiest, neemt zijn gemiddelde afstand tot de gevangenis toe met de afgelegde afstand tot de macht $\frac{4}{7}$.

S.O. Warnaar, privé mededeling

4. Schrödinger's kat en Occam's scheermes leiden samen tot alternatieve werelden.
5. Slechts spinselectieregels kunnen ervoor zorgen dat 'bright beams' niet aan hun eigen succes ten onder gaan.
6. De door Walhout *et al.* geconstateerde vermindering van de diffusiecoëfficiënt rond de nulsnelheid bij laserkoeling in de $\sigma^+\sigma^-$ configuratie is een artefact van het gebruikte semiklassieke model.

Dit proefschrift, hoofdstuk 3

M. Walhout et al. , J. Opt. Soc. B9, 1997(1992).

7. Voor lichte atomen is het Sisyphus-beeld van laserkoeling in de $\pi^x\pi^y$ of MILC configuraties onjuist.
Dit proefschrift, hoofdstuk 3
J. Dalibard and C. Cohen-Tannoudji, JOSA B6, 2023(1989)
8. De koelende kracht bij laserkoeling in de $\sigma^+\sigma^-$ configuratie heeft een relatief lange tijd nodig om opgebouwd te worden.
Dit proefschrift, hoofdstuk 3
P.J. Ungar et al. , JOSA B6, 2058(1989)
9. Op een werkplek die altijd opgeruimd is, wordt zelden gewerkt.
10. Het cliché “een gemeenschappelijke vijand verenigt” wordt bevestigd door het verschijnsel dat de aanwezigheid van één enkele *onsympathieke* man een zeer positieve invloed kan hebben op een werksfeer van overigens alleen maar vrouwen.
11. \LaTeX vermijdt als enige technische tekstverwerker dubbel werk en verdient als zodanig een sterke voorkeur.
12. Meer zelfkennis van alle leden van een moderne (multiculturele) samenleving zou een belangrijke verbetering brengen in het onderlinge begrip en de verdraagzaamheid.
13. Berichtgeving over spontaan verval van de bewaking van gevangenen leidt tot gestimuleerde emissie van gedetineerden.